論文 / 著書情報
Article / Book Information

題目(和文)	ロボット関節のための瞬間的に切り替わる負荷感応型変速機
Title(English)	Load-sensitive Rapidly-switchable Transmission for Robot Joints
著者(和文)	PHLERNJAI Maroay
Author(English)	Maroay Phlernjai
出典(和文)	学位:博士(工学), 学位授与機関:東京工業大学, 報告番号:甲第10661号, 授与年月日:2017年9月20日, 学位の種別:課程博士, 審査員:小俣 透,吉田 和弘,吉岡 勇人,只野 耕太郎,石田 忠,高山 俊男
Citation(English)	Degree:Doctor (Engineering), Conferring organization: Tokyo Institute of Technology, Report number:甲第10661号, Conferred date:2017/9/20, Degree Type:Course doctor, Examiner:,,,,,
学位種別(和文)	博士論文
Type(English)	Doctoral Thesis

Year 2017 Doctoral Thesis

Load-sensitive Rapidly-switchable Transmission for Robot Joints

ロボット関節のための瞬間的に切り替わる負荷感応型変速機

Phlernjai Maroay

Department of Mechano-micro Engineering, Interdisciplinary Graduate School of Science and Engineering
TOKYO INSTITUTE OF TECHNOLOGY

Supervisor: Prof. Omata Toru
Sub-supervisor: Assoc. Prof. Takayama Toshio

Load-sensitive Rapidly-switchable Transmission for Robot Joints

by

Phlernjai Maroay

Abstract

This study proposes a load-sensitive rapidly-switchable transmission (LRT) concept for robot joint applications. The transmission utilizes an ability to rapidly change its reduction ratio between two sets of gears to provide both high speed and high output force applications in robot joints. The concept uses a differential mechanism and a clutch unit to load-sensitively change from a low reduction ratio in a high-speed (HS) phase during low load to a high reduction ratio in high-force (HF) phase when the load exceeds a set threshold. The variable transmission allows more efficient use of a motor compared to traditional transmissions with a fixed reduction ratio. Furthermore, the proposed LRT has high compliance during the phase transition. This characteristic can help limit damage due to collision and is suitable for applications which have a human within its proximity. Possible applications of the LRT concept include robot finger joints for grasping, elbow and knee joints, and power-assistive exoskeletons. Also, industrial machines such as a shearing and punching machine could benefit from the concept as well. In this study, two prototypes of LRT are developed. One is cable-driven and the other gear-driven for in-joint actuation. These two actuation methods are chosen because of their extensive use in robotics.

The cable-driven LRT introduces the idea of using movable pulleys as the differential unit in the LRT concept. A preliminary design proposes using a half-cut movable pulley as both the clutch and differential unit. The idea is experimentally verified to be capable of demonstrating the LRT concept. However, its usage is limited for low load applications due to issues concerning slippage and cable damage. Next, a combination of a pulley differential and a rack-gear clutch is proposed to solve the issue in the first design. A cable-driven 2-DOF robot finger equipped with an LRT prototype is developed for pinching application. The finger/LRT pair is able to generate high no-load speed and high fingertip force after contact with an object. The finger exhibits an average joint speed of 372 deg/s during HS phase and an output fingertip force of 24.6 N during HF phase. The LRT prototype can magnify the output force by 10 times in 0.7 s after the contact is made. Compared to a prosthetic finger with similar actuator weight, the developed finger/LRT pair can provide 50% faster speed, stronger fingertip force, and 4 times less current draw. Compliance characteristic for safety during high-speed motion is also experimentally verified. The LRT unit weighs 156 g including its frame and is compact enough to fit in a human palm.

Next, the gear-driven type LRT is developed with a novel gear-clutch mechanism. The clutch mechanism is proposed for robot joints that need to exert high output torque over a long stroke such in elbow and knee joints. The mathematical model and design method for the gear-clutch mechanism are discussed and experimentally verified. A robot elbow joint LRT using the novel clutch is developed with prosthetic elbows as references. The joint prototype is able to achieve high no-load speed and exert high output torque using a small

DC geared motor. The joint LRT can rotate up to 230 deg/s in HS phase and has a maximum lift capacity of 4 Nm in HF phase. The output torque can be magnified by 11.9 times within 1 s from the start of the phase transition. In addition, high compliance characteristics of the joint are demonstrated with a hammering load to the output link. Performance evaluations show that the joint can operate with two times faster no-load speed than the reference elbow joints with comparable maximum lift capacity. When compared to a fixed reduction motor and gear pair, the developed joint LRT is approximately 13% lighter and consumes 5 times less current during maximum load. The joint weighs 650 g and has an offline load holding ability that could help reduce joint power consumption.

Acknowledgments

To my parents, Sompong Phlernjai and Wilairat Phlernjai: I could not express enough gratitude for what they did. Thank you very much!

I am grateful to Prof. Omata Toru, Assoc. Prof. Takayama Toshio and Assoc. Prof. Tadashi Ishida for all the valuable advice and guidance through out the long years of my research. Also, I am much obliged to Prof. Yoshida Kazuhiro, Assoc. Prof. Tadano Kotaro and Assoc. Prof. Yoshioka Hayato for all the critical comments and advice for the writing of the thesis.

Moreover, I am thankful for all the help of my colleagues and friends, Osaki Mikio, Miyamoto Hiroyuki, Mochizuki Shota, Kuroda Kazuki, Saito Yukari, Abe Ryo, Noda Satsuya, Takaki Satoshi, Kaminaga Maho, Takeshima Hirozumi, Suzuki Maya and all other members of the lab that keep me company and made the life here in Japan so fun.

Lastly, a very special gratitude towards my international friends and company, Wongkitrungruang Mattanee, Chiwern Loo, and many others that help encourage me through this long journey.

Thank you for all of your support!

Contents

Chapter 1

Introduction

Electric motors are widely used in robotic applications to produce maximum output torque at low speed when subjected to a large load. Still, the efficient operating range of electric motor is limited to a certain speed range. Normally, a gearbox with an appropriate reduction ratio is chosen to operate the motor near its maximum efficiency. With traditionally fixed gear reduction ratio, the designer has to compromise between the output torque and speed. That is, to get high output torque, a gear with high reduction ratio is needed, which then limits the output speed during low or no-load motion as shown in Fig.1-1. This design trade-off poses a limitation on the performance of robot joints which are required to operate over a wide range, from low-speed at high torque to high-speed at low torque. Apart from the speed and torque performance of the robot joints, it is preferable to have high compliance to provide safety in case of collision, especially during fast motion [1, 2, 3]. Robot joints with high compliance are useful for applications that involves human in its working proximity. Although it is possible to use a large motor with low reduction ratio as shown in Fig.1-2(a) to achieve both high-speed and high-force performance as well as the desired compliance, the increase in weight and power consumption makes the choice less practical. Fig. 1-2(b) shows an alternative approach using variable transmission. The transmission has low reduction ratio in a high-speed (HS) phase to achieve high-speed/high compliance during low load and has high reduction ratio for high-force (HF) phase to achieve high output torque when under heavy load. Variable transmission allows the use of a smaller and less consuming motor to achieve the target speed and torque. Moreover, the ability to

change reduction ratios enables the motor to run at its most efficient speed for both low or high load situations. An example of robot joints that need at least two different reduction ratio is a finger joint for grasping application. The desirable actuation is that the joint moves fast during no-load and exerts high grasping force when the finger contacts the object. Such operation is defined as a two-phase operation. This study focuses on the simplest case of the two-phase operation which requires a uni-directional high torque. Other applications that benefit from similar actuation scheme include robot elbow, hip and knee joints, vices, prosthetic grippers, jack mechanism or industrial machines such as shearing or punching machine as shown in Fig.1-3.

Until now, many studies have been involved with development of variable transmissions. However, the usage of such transmission in practical robot joints are still very limited compared to the traditionally fixed transmission. The challenge remains in not only the limited space available and weight but also the changing speed of the reduction ratio. For example, a gripper equipped with variable transmission takes a long time to realize the high gripping force if the reduction change speed is slow. Such gripper thus limits the productivity when used in pick and place application. On the other hand, the faster change could also help improve patient experience with prosthetic hands, which are usually described as too slow by the users [4]. Therefore, it can be said that there is a need for a variable transmission that is not only compact but can also rapidly change its reduction ratio. The following sections will review some actuation methods of robot joints, compliance in robot joints and previous works on variable transmissions.

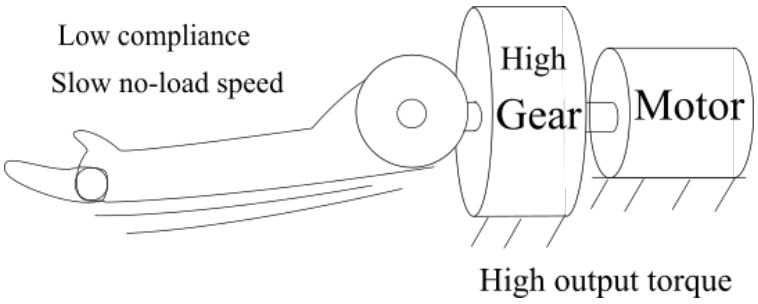

Figure 1-1: Speed limitation of high reduction gear

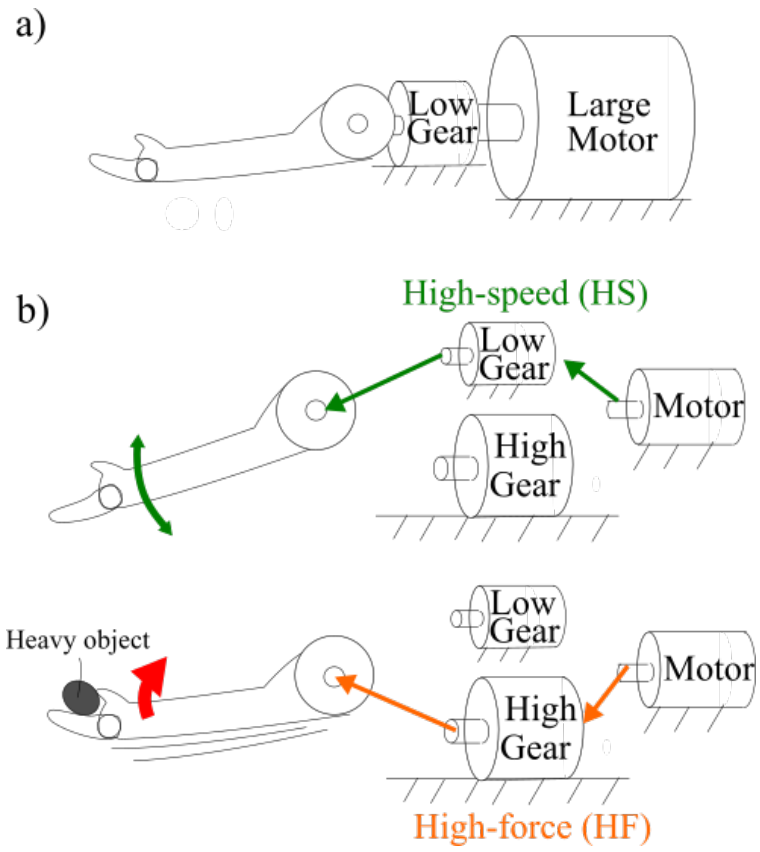

Figure 1-2: Possible solutions to achieve high speed and high torque

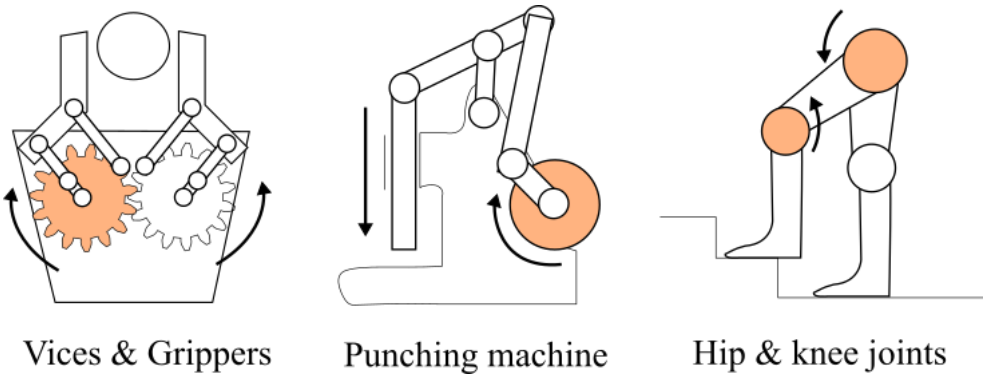

Figure 1-3: Other potential application with two-phase operation
Highlighted parts are motor and transmission with two phase capability

1.1 Robot joint actuation method

Most well-known actuation methods that have been used with electric motors can be separated into two types: 1) Cable drive, 2) Gear and link drive.

1.1.1 Cable drive

The main advantage of driving robot joints with cable is its lightweight and the flexibility of placing the actuator unit remotely from the joint for weight distribution. Robot hands with this actuation scheme are for example the UTAH/MIT Hand [5] and NAIST HAND 2 [6] shown in Fig. 1-4. UTAH/MIT Hand was developed with an ultimate objective of being a test bed for exploring manipulation concept and machine design of robot hands. The hand has 16-DOF and is driven by 32 separate tendons and actuators. The actuators used are dual actuator modules and weigh 9.07 kg; which results in a very heavy total weight of the complete system. However, by using cable drive, the robot hand can be made lighter by placing the actuator modules far apart from the hand. The finger is capable of producing a fingertip force up to 31 N. NAIST Hand 2 is a multi-fingered robot hand with detachable mechanism at the wrist. The actuator drives the hand remotely. The hand weighs 665 g and can exert 10 N at the fingertip. Other examples of cable drive are exoskeletons for rehabilitation where lightweight design is crucial. Fig. 1-5 shows a cable-driven arm exoskeleton (CAREX) [7] and a leg exoskeleton C-ALEX. Both CAREX and C-ALEX are considerably lighter than conventional exoskeletons with rigid links.

Cable drive can provide a very high load transmission per weight. It is often combined with underactuation in robot grasping [8] because of its simplicity. The passive compliance property of cable also helps in improving safety in the joint motion. However, the nature of cable is that it can only apply force through tension but not compression. Therefore, two actuators per joint are needed to actively drive the joint in both directions. In simple grasping application, elastic components such as torsion springs are often used to release the grasp instead of an additional motor. In cable drive system, the joint has to be designed or controlled to maintain positive cable tension at all time.

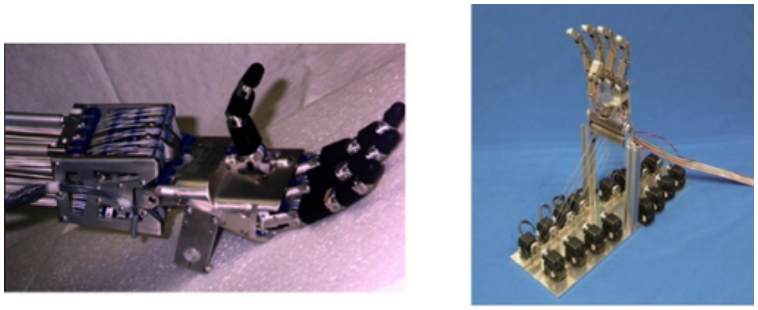

UTAH/MIT Hand NAIST Hand 2

Figure 1-4: Cable-driven robotic hands
(Image from [5, 6])

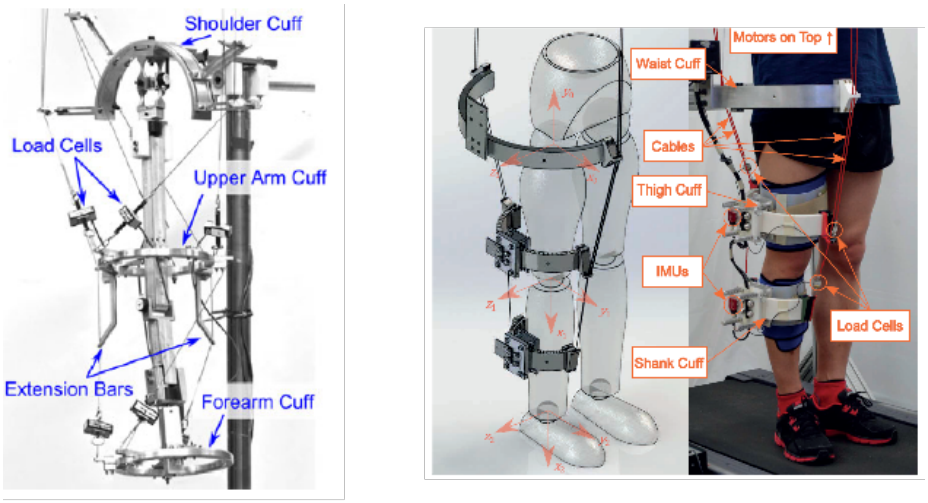

CAREX C-ALEX

Figure 1-5: Cable-driven arm and leg robot exoskeletons
(Image from [7, 9])

1.1.2 Gear and link drive

Another actuation method is to install the actuator directly at or near the joint. The motor and joint are connected by rigid components such as gears or links. The rigidity of the components allows fast response and control between the motor and the output joint. Robotic hands that use this kind of direct actuation are for example [10, 11, 12] as shown in Fig. 1-6. DLR-HAND II uses harmonic drive motors and tooth belt gears. Each finger can move at the joint speed of approximately 360 deg/s and can produce active fingertip force in a stretched finger state of 30 N. The hand with the circuits included weighs 1.8 kg.

Barrett hand is underactuated by links and can carry the maximum payload of 6 kg while it weighs only 980 g. Goldfinger is a non-anthropomorphic dexterous robot hand driven by motors via linkages. The hand weighs 2.27 kg. Some robot arms with this kind of actuation are shown in Fig. 1-7.

Figure 1-6: Robotic hand that has actuator installed at the joint
(Image from [10, 11, 12])

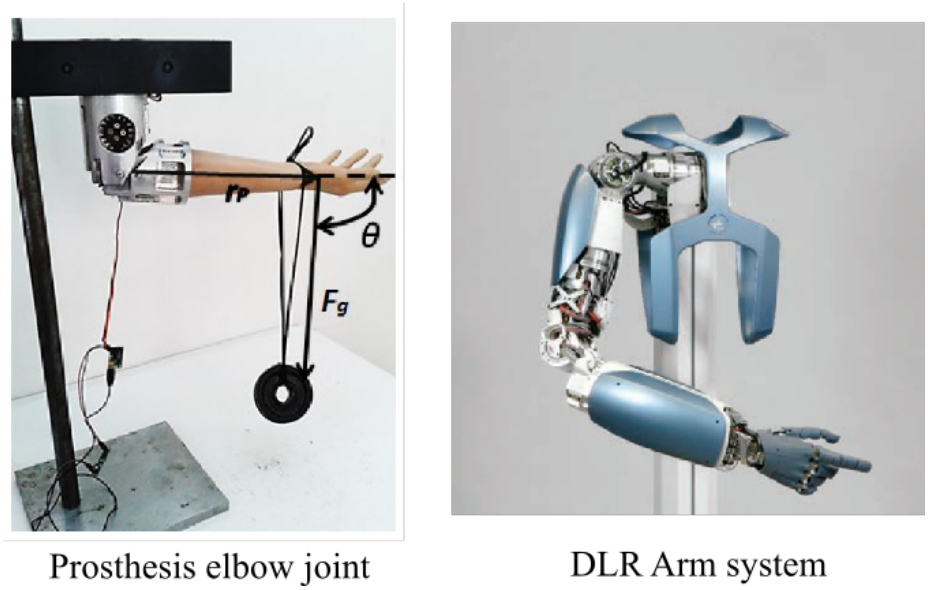

Figure 1-7: Gear-driven robot arms
(Image from [13, 14])

Unlike the cable drive systems, gears and links can transmit the motor torque in both directions. Therefore, only a single motor is needed to control a single joint. However, as the motor and gear are placed near the output joint, this type of actuation is highly dependent on the actuator performance. To get both high output torque speed, the motor

often needs to be large and heavy. Heavy actuators placed in the hand make the hand bulky and the large moment of inertia from the weight calls for larger torque at the arm joint when mounted at the tip of a robot arm.

1.2 Previous research on compliance and safety in human-robot interaction

In robotics manipulation with a human in its environment, it is important for the joint to have compliance property, especially during fast motion of the output link to limit damage in case of collision. Some examples of robot hands or arms that use compliant design have been developed in [15, 16, 17]. On the other hand, stiff joint is preferable when the joint needs to accelerate. Fig. 1-8 shows the desired joint stiffness during a rest-to-rest positioning task as suggested in [18].

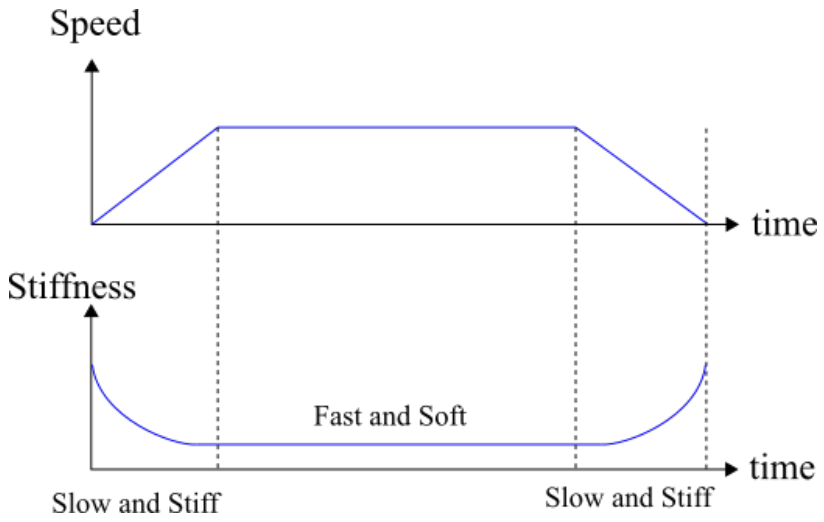

Figure 1-8: Desirable behavior of output joint stiffness in rest-to-rest task[18]

To achieve the desired stiffness profile, the compliance can be actively controlled by controlling the actuator through software and sensors. According to [19], one of the well known examples of compliance control method for a robot joint is the use of antagonistic control as shown in Fig. 1-9. By using two non-linear springs and two separate actuators, each driving the opposite side of the output pulley, the stiffness of the output link can be

controlled. This is inspired by how triceps and bicep muscle works. Similarly, artificial muscle (PAM) such as Mckibben muscle [20] which is inherently compliant can also be used with the antagonistic control method.

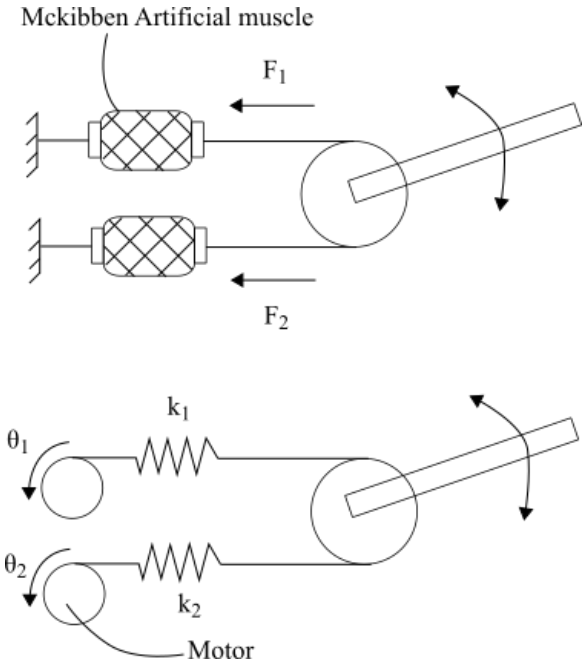

Figure 1-9: Active compliant control by Antagonistic actuation

There has been many studies related to variable stiffness actuators (VSAs) for example, those in [21, 19, 20, 22, 23]. According to [24], the advantage of the active control method is that it offers high programmability of the stiffness. However, due to sensor accuracy and motor saturation, the mechanism cannot provide immediate change in compliance during high speed collisions unless it is equipped with more complex collision detection and control method. On the other hand, passively compliant actuators is more reliable for the use in collision safety. An actuation system that has passive compliance during fast motion is a parallel coupled micro-macro actuation or PaCMMA[25] and its improvement in distributed macro-mini actuation DM^2 [26]. Fig.1-10 shows a schematic diagram of the PaCMMA. The idea is to use two actuators to drive the output joint in parallel. The micro actuator directly drives the joint. The macro actuator is connected in parallel with the micro actuator through a compliant transmission. The output torque is the addition of the two actuators. When a collision impact occurs, the compliant transmission passively separate

the inertia of the macro part from the micro part. The effective low stiffness during the impact helps reduce possible damage to the joint itself and the impact target. The concept of using a compliant transmission was introduced in a series elastic actuator (SEA) [27]. SEA has been employed in many compliant actuation systems such as [28, 29]. The elastic component couples the output position with the output force, allowing accurate and stable force control. However, the elastic component inevitably slows down the rising in the output force when compared to a stiff transmission, given the same actuator and reduction ratio.

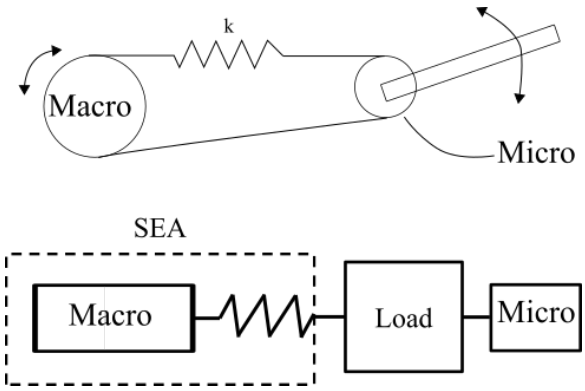

Figure 1-10: Schematic of Parallel Coupled Macro-Micro Actuation

1.3 Previous studies on variable transmission for robot joint

Transmission that can change their reduction ratio can be generalized by two main types, a continuously variable transmission (CVT) and rapidly-switchable transmission (RT) as follows

1.3.1 Continuously Variable Transmission (CVT)

The continuously variable transmission is, as the name suggested, change it reduction ratio continuously (not necessary linearly) from one value to another, which allows the use of many reduction ratios in between. CVT can be divided into two types, active and load-sensitive type.

Active CVT

This type of transmission actively changes its reduction ratio using an additional actuator. Fig. 1-11 shows a crank CVT driven by two links [30]. The transmission uses two sets of motor and ball screw to continuously control the output torque by changing the position of point A and the resultant force of the motors. The use of ball screw makes the transmission non-backdrivable and can only achieve compliance by active compliance control.

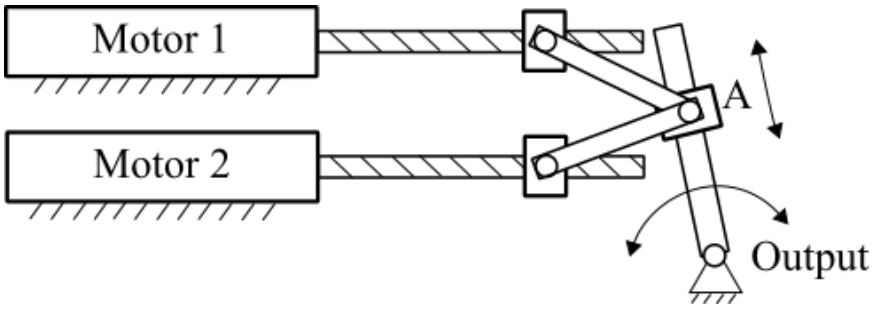

Figure 1-11: Crank CVT [30]

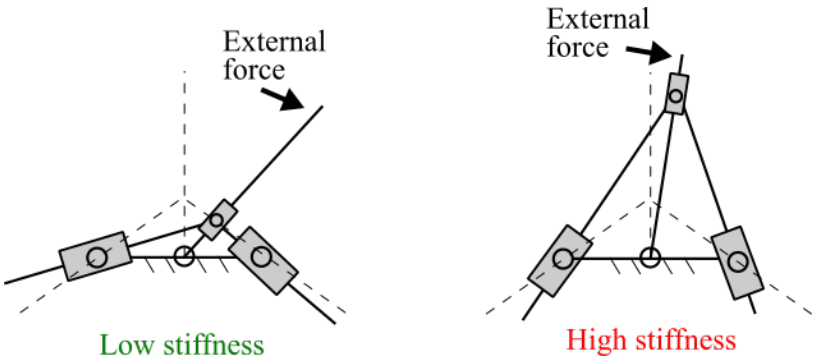

Figure 1-12: Stiffness control with CVT in parallel link manipulator [31]

Similar actuation method combined with back-drivable actuators can give a controllable passive compliance to the manipulator [31] as shown in Fig.1-12. This controlability over the stiffness profile can help promote safety in human-robot interaction. Still, such highly backdrivable linear actuators are weak and need to be used in parallel with multiple actuators to produce the desired output force.

Load-sensitive CVT

To get a more compact design, the actuator controlling the reduction change can be replaced by a spring or friction clutch. The spring in couple with the load turns an active into a load-sensitive transmission. The idea is to use the increase in load to mechanically and passively change the reduction ratio depending on the load.

A robot finger joint with load-sensitive CVT [32] is shown in Fig.1-13. This CVT mechanism uses mechanical advantage of linkage to achieve higher output fingertip force with only one motor. The output torque is determined by the relation between L_{in} and L_{out}.

$$\tau_{out} = \tau_{in} \frac{L_{out}}{L_{in}} \tag{1.1}$$

Initially, the torsion spring is preloaded to hold the longest L_{in} so the finger can move in high-speed (a) because of the low reduction ratio. After the finger touches the object (b), the motor keeps spinning and continuously reducing the length of L_{in}. As the linkage continuously changes, the reduction ratio gets higher which results in higher output force (c). The reduction ratio of the link CVT can change around 3 times. The reduction ratio can theoretically reaches an infinity for certain output angles θ_{out} (80 deg) due to the singularity of the linkage. The finger joint has a motion range of 70 deg $\leq \theta_{out} \leq$ 138 deg. The output link can rotate as high as 550 deg/s during no-load and produce up to 100 N output force at 75 deg, 80 deg and 130 deg output angles. With clever use of a shape memory alloy (SMA) brake, the finger joint can be over-driven by a large amount of current for a brief period and consequently braked to hold 100 N output force for a wider range of output angle. The reduction ratio change time was measured to be around 0.3 s during this current overdrive. However, the use of SMA inevitably introduces a cooldown time of 6 s for releasing the grasp. The CVT joint weighs only 100 g which is considerably light for robot finger joint.

Matsushita et al. developed a CVT mechanism with a drum structure [33] shown in Fig. 1-14. A motor is used to rotate the drum. The drum structure is designed so that it gets radially smaller when cable tension gets higher. The load-sensitive decrease in drum radius then contributes to higher reduction ratio which results in higher output force. There are two designs of the drum. a) is a deflection type which the poles deflect inward under

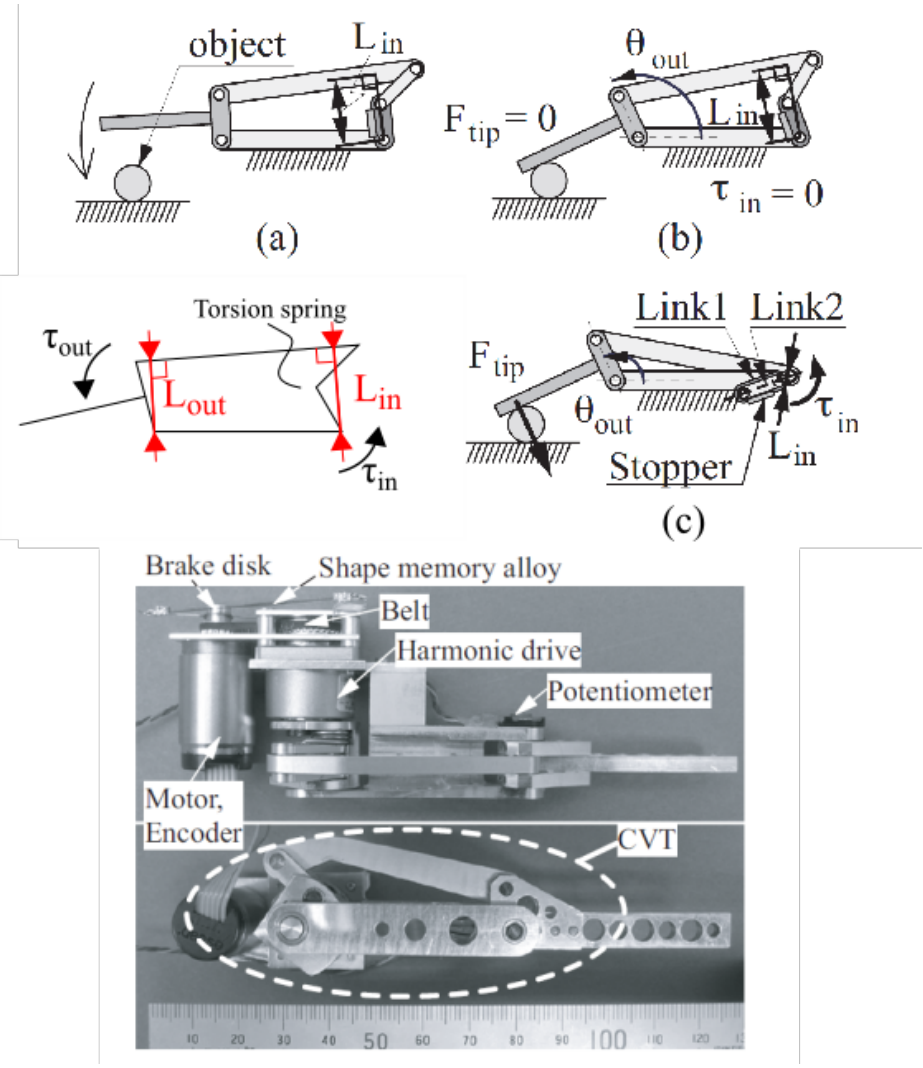

Figure 1-13: 100g-100N finger joint with load sensitive CVT
(Image from [32])

load. Another one b) is called a torsion type which reduces its radius by torsional twist of the poles. The drum CVT is able to change the reduction ratio from 1 to 3 for deflection type and 1 to 2 for the torsion type. The time of change is 1.2 s for the deflection type and 0.5-0.8 s for torsion type. A cable-driven robot finger that used a similar design of CVT was developed in [34]. As the drum radius is the determining factor of the reduction ratio, the drum CVT has to be large to get wider range of reduction ratio.

Another cable-driven CVT is a dual-mode twisting mechanism for robot finger [35] in Fig. 1-15. The CVT uses the twisted string actuation system [36] that produces high contraction force by twisting strings, cables or belts. The contraction length ΔL can be

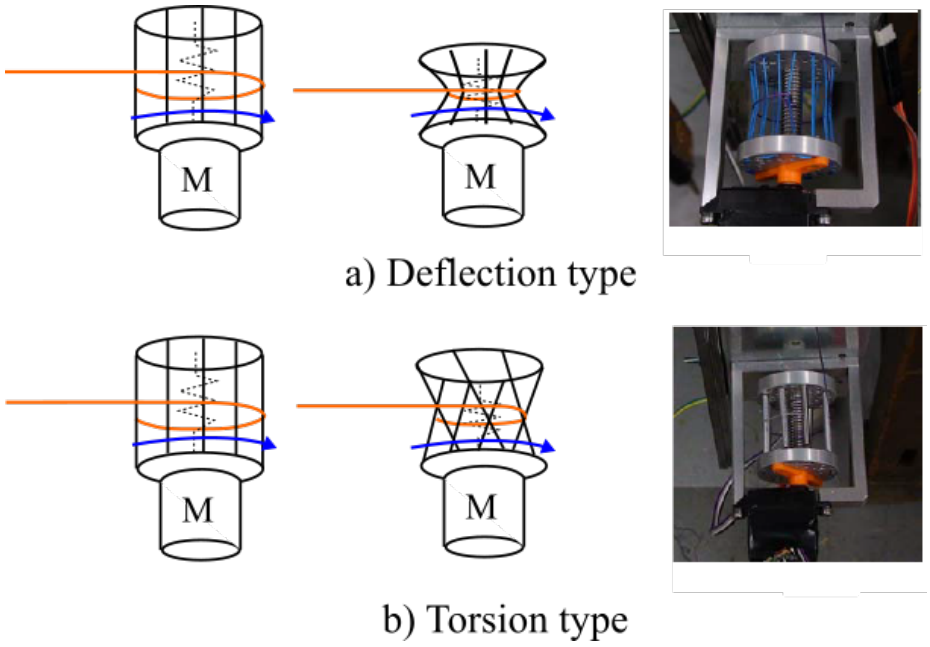

Figure 1-14: Drum CVT mechanism
(Image from [33])

calculated from unwrapped helix of the twisted strings, assuming no axial elongation of the strings.

$$\Delta L = L_0 - \sqrt{L_0^2 - \theta^2 r^2} = L_0(1 - \cos\alpha) \tag{1.2}$$

where L_0 is the initial length of the string. α is the helix angle. θ is the motor rotation angle, and r is the twisting radius. The contraction length ΔL is a continuous but non-linear function of θ. When the motor turns and θ increases, the helix angle increases from zero to a certain max value due to finite diameter of the string. At this max α, the twisting actuation reaches its maximum reduction ratio (large input θ results in small contraction ΔL). In the dual-mode twisting mechanism, Part I of the cable is designed to have a bigger twisting radius than Part II ($r_1 > r_2$) so that the part I contraction speed is faster than Part II according to Eq. 1.2. With the passive clutch preventing rotations of Part II during low load, only Part I rotates and produces fast bending motion of the finger. After contact with an object, the increased motor torque causes the clutch to slip. Part II then rotates and acts

as another twisting CVT, producing a high grasping force of the finger. The finger is able to rotate 12.1 times faster and exerts a fingertip force 4.61 times larger when measured separately for each mode. The time used to reach the high output force were reported about 5 s after high-speed motion. The weight of the finger with the CVT is only 29.9 g which is very light. However, the drawback of this design is the slow change of reduction ratio and difficulty during finger release because of the friction clutch. A robot hand utilizing this twisting mechanism has been presented in [37] with an additional actuator to control the clutch which can improve the releasing performance.

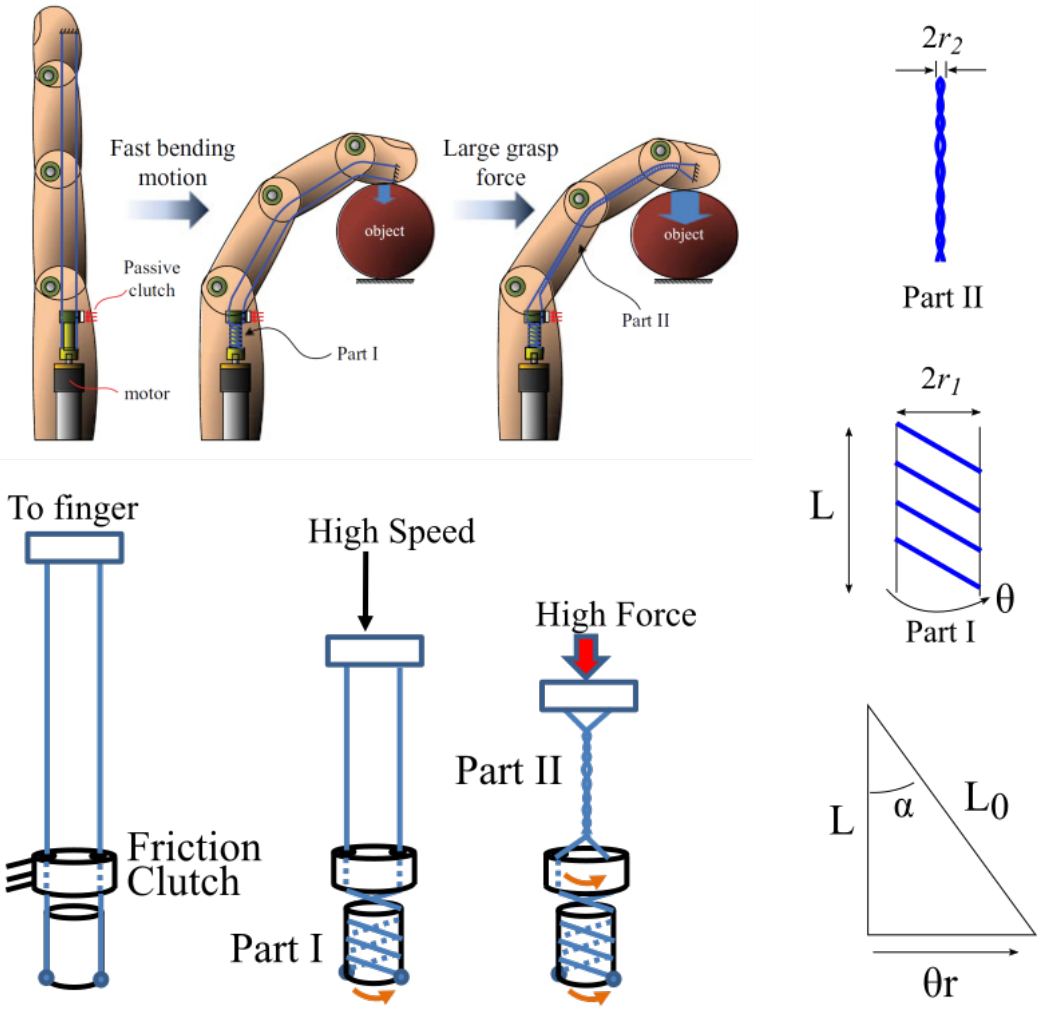

Figure 1-15: Robot finger with dual-mode twisting mechanism
(Upper image from [35])

Advantages and limitations of CVT for two-phase application

Active CVTs can independently control its reduction ratio to several values regardless of the output position. However, the need of multiple actuators to control a single output increase the size and weight of the transmission. This might not be suitable for small robot joints such as in robot hands and arms. On the other hand, load-sensitive CVTs have advantages of its compactness and simplicity. However, the reduction change rate (Reduction change/s) of most load-sensitive CVTs are relatively low, especially for cable-driven CVT. Also, CVTs often have a physical correlation between its output position and usable range of reduction ratio. For example, CVT can greatly change its reduction often have a very limited motion range of the output, which is not suitable for two-phase application in robot arms.

1.3.2 Rapidly-switchable Transmission (RT)

Rapidly-switchable Transmission (RT) is also known as step transmissions. The transmission can provide an abrupt change in its reduction ratio using a clutch or a singularity of the design. Fig. 1-16 shows a graphical comparison between RT and CVT with in robot grasping application. Theoretically, a step change from low reduction to high reduction can cause the output torque/force to rapidly increase as compared to the continuous change in CVT, assuming the same object and mechanical stiffness. A common example of RT is an automotive transmission which the reduction ratio is changed by selecting gear engagement pairs. Another example is a transmission in bicycles which the chain jumps from one sprocket to another. However, the idea of using such transmissions of cars and bicycle for robotic application are still not as commonly known as CVT. This is because of their size and some limitations. For car transmission, a clutch has to cut the engine power off from the gear in order to change, which results in a non-driven state during the time of clutch disengagement. This is not suitable for robotic application such as load lifting as the load will drop during the change. Moreover, changing gears in bicycle requires continuous rotation of the sprockets. Therefore, it is not suitable for grasping task which the change in reduction ratio has to be made after the finger is stopped by the contact. There have

been few researches regarding development of RT. The RT can be separated into two types, active and load-sensitive.

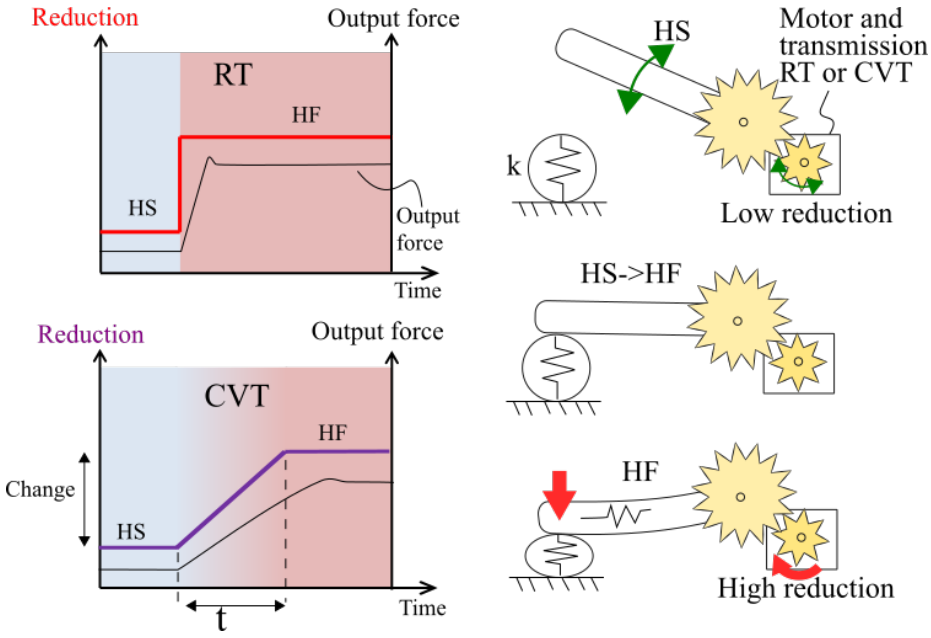

Figure 1-16: Comparison between CVT and RT with robot grasping

Active RT

Previous studies of our lab introduced RT for robotics application. Robot hands using the developed transmission are, for example, 100N Hands in [38, 39]. Fig.1-17 shows the schematic diagram of high-speed and force magnification drive of the hands. The hands use two actuators, each for HS and HF phase. The two actuators are connected serially to the output link. The 3D toggle mechanism uses of the mechanism singularity to rapidly generate high output force. In order to achieve this high output force, a non-backdrivable component has to be introduced to Motor 1 such as the screw and nut in [38] or the worm gear in [39]. 100N-Hand II is the improved version of 100 Hand I. The improvement in range of motion were achieved by using the worm gear drive instead of the link and screw drive in 100N-Hand I. Theoretically, the 3D toggle is a CVT mechanism that can increase reduction ratio to infinity with a small stroke. In the case of these two hands, the 3D toggle are designed to be used as a switch to rapidly change the reduction ratio to infinity without using the reduction values in between. Moreover, because of the small

stroke needed to toggle, the change can be very fast. Therefore, the transmission with 3D-toggle is categorized as an RT type. The hands can change into HF phase at any output angle. Hand I weighs 941 g and Hand II weighs 1063 g. The maximum joint velocity is above 200 and 400 °/s for hand I and II, respectively. The maximum fingertip forces of both hands are over 100 N. The output force in HF can be exerted within 0.4 s after contact (Hand II). The non-backdrivability of the 3D toggle can keep HF force without energy consumption. However, its small stroke (1 mm, 2 mm in Hand I and II, respectively) limits the finger travel range after the contact is made. That is the object needs to be stiff enough ($k > 150$ N/mm) to achieve the high grasping force of 100 N. Also, the use of non-backdrivable component means that a force sensor will be need to actively control the output compliance of the fingers.

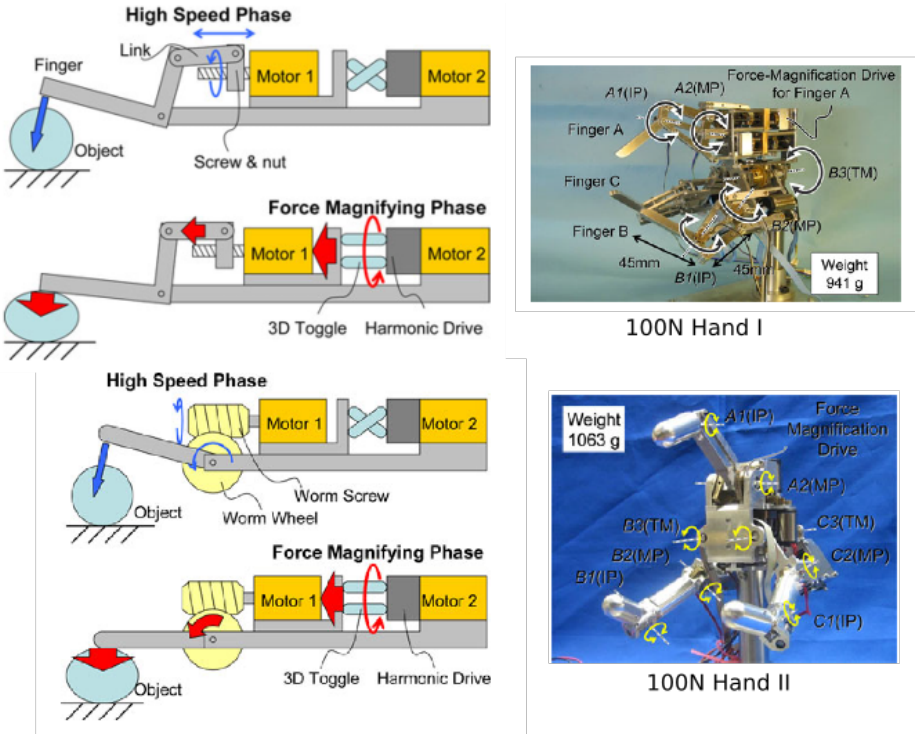

Figure 1-17: 100N Hand I,II and 3D toggle mechanism
(Image from [38, 39])

Next, a Large grasp force hand with passively high compliance during HS phase was developed in [40]. Fig. 1-18 shows the hand with its schematic diagram. The transmission uses a rack-gear connection as a clutch to connect/disconnect input power from two actua-

tors with different reduction ratios. In this case, M1 is a motor with low reduction used to drive the finger joints in high-speed. M2 is a motor with high reduction gear used to drive the rack unit in HF phase. A novel rack-tilting mechanism was introduced to allow the rack to tilt and slip into engagement without jamming with the output gear. In this design, the HF stroke can be enlarged by increasing the rack length so the hand can be used to grasp a soft object. The finger joint speed is more than 750 deg/s and can produce a large grasping force of 120 N within 0.7 s. The hand weighs 1.2 kg. On of the advantages of this design is that the finger can be back-driven with high compliance during HS phase without feedback control, promoting its usage in applications involving human robot interaction. Also, note that the two reduction sets can be chosen from the motor gearbox and not part of the mechanism transformation such as CVT. As the ready-made gearbox are available in various ratios and sizes, this provides flexibility in the hand design. Still, a mean of contact sensing is needed to know when to activate M2.

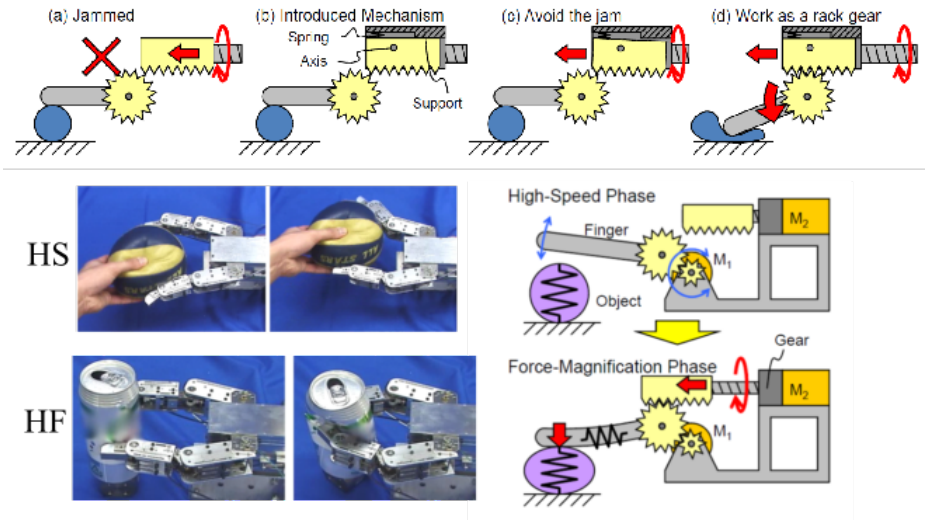

Figure 1-18: Large grasp force hand and rack-tilting mechanism
(Image from [40])

Load-sensitive RT

There are a few studies involving transmission that can be categorized as a load-sensitive RT (LRT). Most of these are for linear actuation used in parallel jaw grippers. For example a grasp force magnifying mechanism in [41]. Fig.1-19 shows the working principle. The

mechanism consists of one motor and a lead screw pair 1 and 2 which rotate together. Both screws are right-handed, but Screw 2 is designed to have a smaller pitch than Screw 1. Gear 2 connects the motor with Screw 2 and has a screw thread on the inside similar to a nut. The gripper has to be initialized. First, the backward motor rotation cause Gear 2 to move left toward the stopper. After Gear 2 is tightened against the stopper, the rotation is transmitted to the jaw side and move the jaw to the right, which opens up the grasp. Further motor rotation then tightens both the jaw and Gear 2. After this initialization state (1), the gripper is ready to produce two-phase grasping. When the motor is driven forward. The jaw side will get loosen first because of the larger pitch of Screw 2. The tightened Gear 2 is still in contact with the stopper because the motor torque under no-load is not enough to loosen it. Therefore, the gripper will work in HS phase first during no-load until it reaches an object (2). After the contact with object, the increased motor torque then loosens Gear 2 to the right and pushes the lever mechanism which axially displaces the whole gripper slider unit toward the object by a small stroke (3). This lever works similar to the 3D toggle introduced in previous discussion and produce high grasping force by the singularity of the lever. The gripper weighs only 86 g and can exert a grasping force of 200 N, 60 N with and without the force magnifying, respectively.

A load-sensitive RT with a two-way Clutch in [42] was developed as an actuation unit of a crawler robot HELIOSVII [43]. Although its application is not intended for robot hand and arm joints, the transmission is included for the sake of similarity of the idea. The mechanism utilizes a two-way clutch and a friction clutch to switch between low load application and high load application. The mechanism and its components are shown in Fig. 1-20. In low load, the output axis is directly driven by the actuator through the friction clutch. Also, the two-way clutch allows free rotation of its outer ring in both direction if the outer ring speed is higher relative to the inner ring. This results in the low reduction ratio of the mechanism. During high load, high output torque causes the load-sensitive friction clutch to disengage. The transmission path then changes to the reduction unit and drive through the two-way clutch to the output shaft. The change in the reduction ratio is abrupt and can be considered an RT. It can change the reduction ratio (HF/HS) by about 4 times. The mechanism weighs 3.2 kg and is 150 mm in diameter.

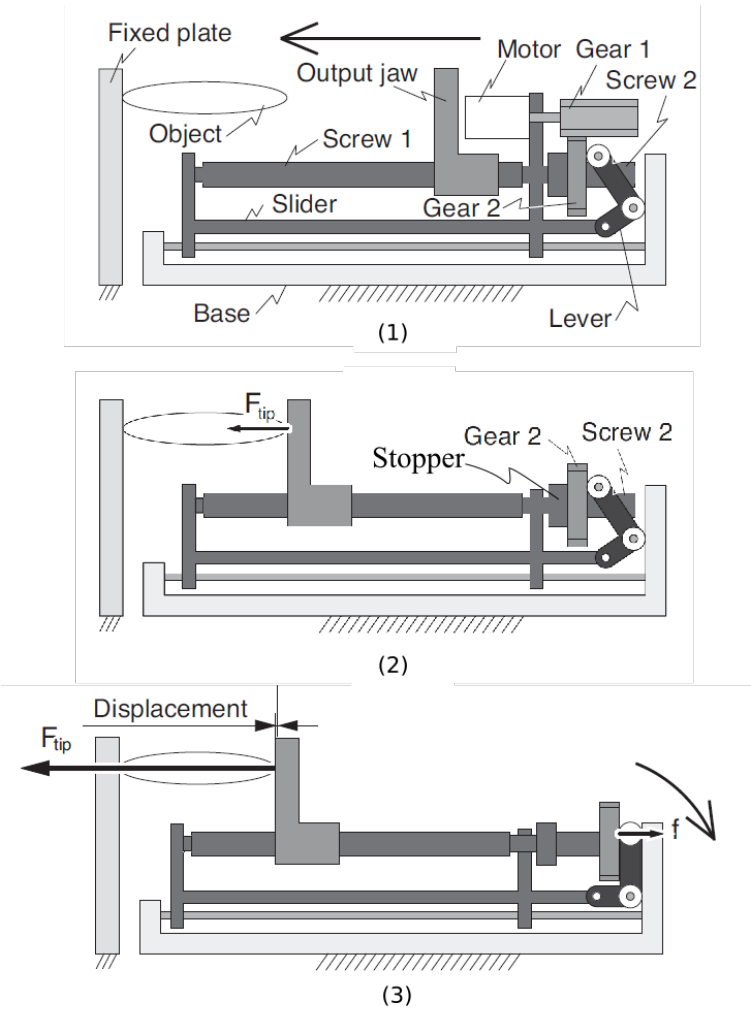

Figure 1-19: Parallel jaw grippers with grasp force magnifying mechanism
(Image from [41])

Advantages and limitations of RT for two-phase application

Both 100N Hands with the toggle mechanism can generate large grasping force very rapidly but the grasp is limited to significantly stiff objects due to the small stroke of the toggle mechanism itself. The use of rack-gear clutch in Large grasp force Hand provide a longer range of the HF stroke which can be easily increased by adjusting the rack length. Also, the hand has high compliance during HS phase when the clutch is in a disengaged state. Active RT discussed above all have the flexibility to choose the reduction ratio at any time. However, in simple applications such as grasping or load lifting, a load-sensitive approach with one actuator would be more compact and simple as there is no need for an additional

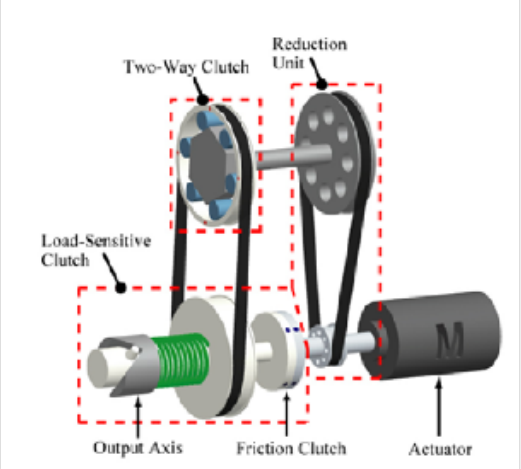

HELIOSVII

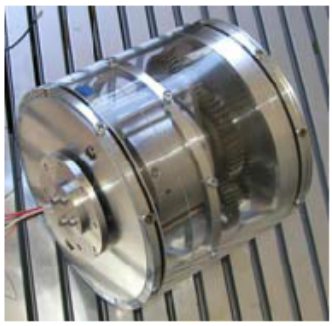

Actuation unit

Figure 1-20: Load-sensitive RT unit with two-way clutch
(Image from [42])

contact sensing component and less controller needed. Still, studies on load-sensitive RTs mainly focused on linear actuation or large drive train systems. Although the linear drive can be used with links to produce rotation, the limited range and lengthy space claim may pose some difficulties in the design of robot rotational joints. Also, the use of toggle mechanisms limits its working range. Load-sensitive RT designed for drive trains can generate unlimited rotations. However, the design involves using two clutch mechanisms are often too large and heavy to be implemented in robot hand and arms.

1.4 Research objective and organization of the thesis

This study proposes a concept of load-sensitive RT (LRT in short) for robot joints. From the discussions in this chapter, the transmission should have characteristics as follows

1. Use a single actuator to operate
2. Rapid reduction change time within 1 s, which is comparable to active RT
3. Compact enough for robot hand and arm joints
4. High compliance for safety during high-speed

The next chapters of this study are organized as follows.

Chapter 2 describes the concept of LRT, its components, and actuation scheme. First, Serial and parallel actuation schemes of dual-motor systems are discussed. Since the serial actuation requires a non-backdrivable component to exert high output torque, the parallel actuation method is chosen for the proposed LRT. The importance of a clutch mechanism in parallel actuation is then addressed. Next, the actuation concept of the LRT is introduced. The main idea is to use a differential and clutch mechanism to produce a load-sensitive switching behavior of the transmission. The differential mechanism and clutch are analyzed in generalized forms. Then, mathematical models of LRT regarding the effective reduction ratio and output force/torque are proposed. Additionally, the stiffness profile of the transmission is analyzed to show that it has a high compliance characteristic for safety. Some design considerations of the proposed LRT concept are also discussed in this chapter.

Chapter 3 presents a cable-driven LRT for robot finger joints. A preliminary concept is proposed with a novel split-pulley clutch. The idea is to split the movable pulley into halves and use them as both the clutch and differential unit of the LRT. The ability to load-sensitively switch the reduction ratio is then experimentally verified. However, a limitation exists as the clutch produces cable damage for after several uses. Therefore, an improved design concept for the cable-driven LRT is proposed. The idea uses a rack-gear

engagement as a clutch and the movable pulley as a differential. The design is verified to be more practical than the split-pulley design because there is no cable damage. Next, developments of a 2-DOF underactuated robot finger and LRT prototype are discussed. Development considerations for two-phase pinching operation are shown. Static experiments on the developed LRT unit is used to determine the practicality of the mathematical model used in the actual prototype design. Pinching experiments are also conducted to evaluate the performance of the finger/LRT pair. High compliance characteristics of the finger/LRT pair is verified experimentally using drop test. In addition, analysis on cable friction and maximum achievable output force is discussed in this chapter. Lastly, the performance of the finger/LRT pair is compared to an existing cable-driven prosthetic robot finger used as the design reference.

Chapter 4 presents a gear-driven LRT for robot elbow joints. First, the space claim limitation of the rack clutch when the joint has to exert HF torque over a longer stroke is discussed. This chapter proposes a novel gear-clutch mechanism which is potentially more compact than the rack clutch used in the cable-driven LRT. The gear-clutch design criteria on jamming and meshing are introduced. A mathematical model of the clutch is developed and verified experimentally. Then the introduced design criteria of the clutch are used in the actual design and development of an elbow joint LRT prototype. Experiments confirming jam-free engagement and one-way characteristics of the clutch are conducted. Transmission efficiency and torque magnification ratio are then investigated with static tests on the joint prototype. In addition, the high compliance characteristic of the joint during high-speed motion is verified by a hammering test. Next, dynamic load-lifting experiments are performed to confirm that the developed joint LRT with the gear-clutch can produce two-phase lifting as intended. Finally, the joint performance is then evaluated by comparing with existing prosthetic elbow joints and a reference fixed reduction ratio geared motor system.

Chapter 5 concludes the study chapter by chapter. The performance of the developed prototypes and the practicality of the proposed LRT concept are discussed. In addition,

considerations for possible applications, and future works are also discussed in this final chapter.

Chapter 2

Load-sensitive Rapidly-switchable Transmission (LRT)

This chapter proposes a load-sensitive rapidly-switchable transmission for two-phase operations in robot joints. The target application is the simplest case that requires HF operation in only one direction such as grasping or load lifting as discussed in chapter 1. Before explaining the actuation method of the proposed LRT, let us first cover actuation methods that were used to produce two-phase operation with two actuators.

2.1 Serial and parallel actuation

Fig.2-1 shows the actuation schemes of the active RT, classified as serial and parallel actuation. In serial actuation (a) motor M1 with low reduction is connected to the output shaft of a high gear reduction G driven by motor M2. In this arrangement, high output torque from M2 cannot be transmitted to the output link because M1 is back driven. Therefore, the serial actuation require a non-back-drivable component LD placed between M1 and the output link as shown in (b). This LD could be a locked type torque diode, lead screw or a worm gear. The worm gear and 3D toggle mechanism in [38, 39] are examples of LD in serial actuation method. The obvious advantage of the serial actuation is that it can enhance the output motion range and speed by the combination of both actuators. Still, the disadvantage is the inherently stiff output due to the non-back-drivable component. On

the other hand, parallel actuation in (c) combines the output torques from both motors but couples their rotation. This means that the output speed is limited by the slower input, which is M2 with high reduction gear. To solve this problem, a free type torque diode FD or clutch mechanism is required as shown in (d). With this arrangement, the output link can be driven at high speed by M1 and the high output torque can be achieved by once the output speed is lower than M2-G drive or by switching the clutch into connected state. The clutch mechanism can be controlled by an additional actuator or by the M2 itself as in [40]. Although serial and parallel actuation with two motors can produce two-phase operation as desired, there are still some disadvantages. In serial actuation, during HF phase, M1 does not contribute to the output torque. In parallel actuation during HS phase, M2 cannot contribute its power to the output speed. This means only one of the two motors contribute work to the output link while the other acts as a dead weight to the transmission.

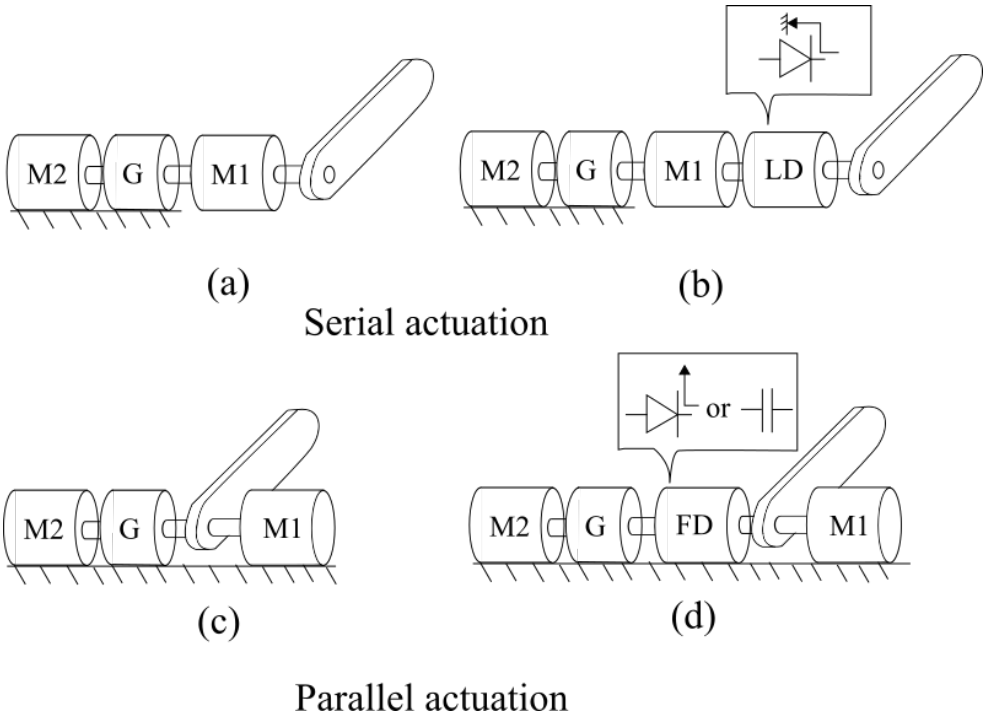

Figure 2-1: Serial and parallel actuation

As we can see, the actuation scheme of RT involves driving the output link through two different reduction gears (High reduction gear G and low reduction within M1). With a load-sensitive approach, we can use a single motor to drive these two reduction gears using

a differential mechanism. This way, the motor will contribute work to the output at all time and potentially leads to a more compact transmission for two-phase operation.

2.2 LRT Actuation scheme

Fig. 2-2 shows the proposed actuation scheme of LRT using a differential mechanism with parallel actuation. Parallel actuation is chosen because it does not require a non-backdrivable component. The motor is connected to a differential gear D, which distributes the motor power to both the low reduction gear G1 and high reduction gear G2. The output from G1 is connected to the output link and is used to provide swift motion of the link in HS phase. The output from G2 is connected to the output link through a load-sensitive clutch $\mathrm{C_{ls}}$, which switches its connect/disconnect states based on the amount of the load. The idler gear is added between the differential output 1 and the input of G1 to ensure the same output direction from both low and high reduction paths. The load-sensitive clutch can be realized by coupling one of the differential output to the clutch control input. In Fig. 2-2, G2 output shaft is connected to the clutch input. The idea is to switch the clutch connection when the load exceeds a certain threshold value. This threshold value can be implemented by using a preloaded spring, friction clutch or any other mechanism that can hold the clutch until a limit is reached. During low load, the clutch is in a disengaged state; the motor power goes through the low reduction path G1, producing HS phase. When the load exceeds the threshold value, the increased input torque from motor causes the clutch to engage. The outputs from both G1 and G2 then work in parallel to produce HF phase. Further details on the differential and the load-sensitive clutch are covered in following subsections.

2.2.1 Differential mechanism

A differential is a mechanism that can distribute an input torque/force to multiple outputs. Fig. 2-3(a) shows the schematic of a differential gear. A simple explanation of the mechanism is that when the output 1 is fixed, the input power is transmitted to output 2. On the contrary, if output 2 is fixed, the input power is then transmitted to output 1. When neither

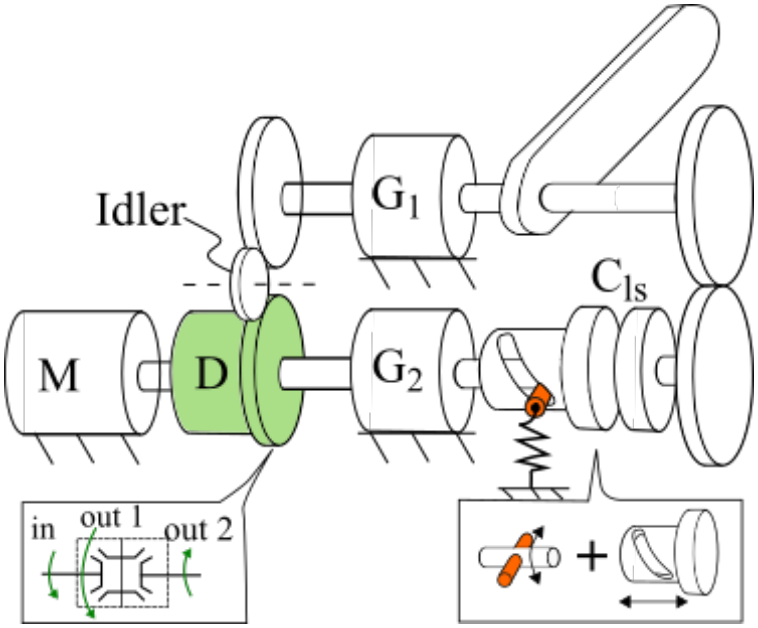

Figure 2-2: Actuation scheme of LRT

output 1 and 2 are fixed, the input power is distributed according to the difference in speed of the two outputs. Kinematically, the relation between the speeds can be described with the following equation, similar to the planetary gear train.

$$\frac{-Z_2}{Z_{in}} = \frac{\omega_{in} - \omega_1}{\omega_2 - \omega_1} \tag{2.1}$$

where Z_{in} and Z_2 is the number of gear teeth of the input and output 2, respectively and are always positive. As we can see, the reduction ratios of a differential $R_1 = \omega_{in}/\omega_1$ and $R_2 = \omega_{in}/\omega_2$ depend on the speed of both outputs.

Consider a scenario when $\omega_1 = 0$, reduction ratio R_2 is then

$$R_2 = \frac{\omega_{in}}{\omega_2} = -\frac{Z_2}{Z_{in}} \tag{2.2}$$

Consider the case where $\omega_2 = 0$, reduction ratio R_1 is

$$R_1 = \frac{\omega_{in}}{\omega_1} = \frac{Z_2}{Z_{in}} + 1 \tag{2.3}$$

Note that the ratio Z_2/Z_{in} is equal to 1 for differential gear with the same size of bevel gears at both input and output 2. Assuming the differential in equilibrium, we can write equations of torque and power by

$$\tau_{in} + \tau_1 + \tau_2 = 0 \tag{2.4}$$

$$\tau_{in}\omega_{in} + \tau_1\omega_1 + \tau_2\omega_2 = 0 \tag{2.5}$$

From Eq. 2.4 and Eq. 2.5, the torque relations are as follows

$$\frac{\tau_1}{\tau_{in}} = \frac{\omega_{in} - \omega_2}{\omega_2 - \omega_1} = -(\frac{Z_2}{Z_{in}} + 1) = -R_1 \tag{2.6}$$

$$\frac{\tau_2}{\tau_{in}} = \frac{\omega_{in} - \omega_1}{\omega_1 - \omega_2} = \frac{Z_2}{Z_{in}} = -R_2 \tag{2.7}$$

Eq.2.6 indicates that τ_1 has an opposite direction as τ_{in}. On the other hand, Eq.2.7 indicates that τ_2 has the same direction of τ_{in}. Note that these torque relations remain true regardless of the speeds. Therefore, it would be easier to use the torque relations than speed relations in the analysis of a differential. Fig. 2-3(b) shows the expected directions and magnitudes of the outputs based on calculations, where $R_2 < 0$ and $R_1 > 0$.

Other examples of differential mechanisms are such as planetary gears, movable pulley, and lever mechanism as shown in Fig. 2-4.

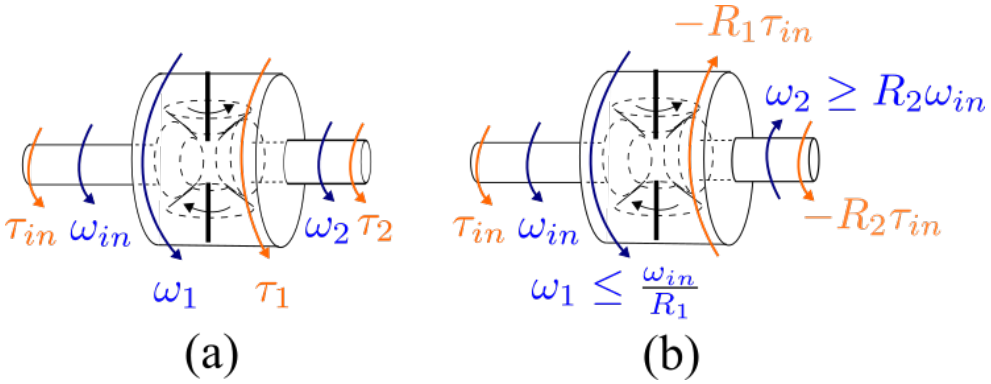

Figure 2-3: Schematic of differential gear

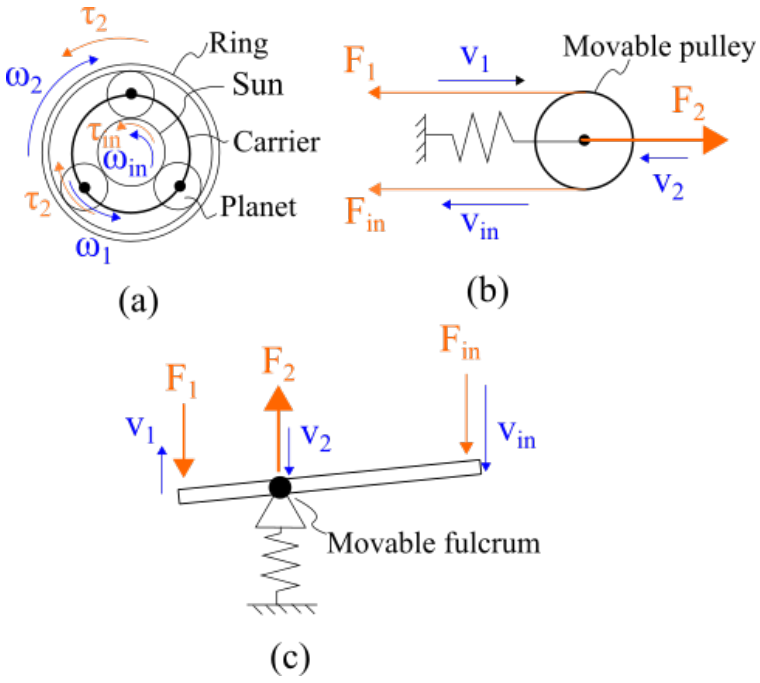

Figure 2-4: Other examples of differential mechanism
(a) Planetary gear (b)Movable pulley (c) Lever mechanism

2.2.2 Load-sensitive clutch

A load-sensitive clutch is a mechanism that switches its working state based on the load. One of the simplest design is the used of a shaft and a slotted collar as shown in Fig. 2-5. The input shaft has a pin connected laterally to the shaft. The shaft is covered by the slotted collar which transforms rotation of the input shaft to axial movement of the collar. The load-sensitive part is achieved by using either a preloaded spring in (b) or by a friction brake in (c). Another way of holding the input shaft is a magnetic brake or slip-type torque limiter (d), which is similar to the friction brake but without contact surface to prevent mechanical wear. Alternatively, a stopper (e) can also be used to apply holding torque using ball and indent at the initial location of the collar. (f) shows the free body diagram of the load-sensitive clutch. When the clutch input torque τ_{cin} exceeds a preset threshold, the input shaft rotates and consequentially moves the clutch plate A to engage with plate B. Once engaged, the input torque is transmitted to the output side of the clutch. Some of the input torque is used to overcome the holding torque of the clutch τ_c which is a function of rotation angle θ_s. Therefore, the clutch output torque can be calculated by

$$\tau_{cout} = \tau_{cin} - \tau_c \tag{2.8}$$

From Fig. 2-5, τ_c is a function of θ and is dependent on the preloading method.

$$(b) \qquad \tau_c = k_\theta(\theta_s + \theta_0) \tag{2.9}$$

$$(c, d) \qquad \tau_c = C \tag{2.10}$$

$$(e) \qquad \tau_c = \tau_{cin} u(\tau_{cin} - C)\delta_\theta \tag{2.11}$$

where k_θ is the torsion spring constant. θ_0 is the preloaded angle. C is a constant threshold value. $u(x)$ is the unit step function and δ_θ is the Kronecker delta function, which equals to 1 only at $\theta = 0$ and equals zero everywhere else.

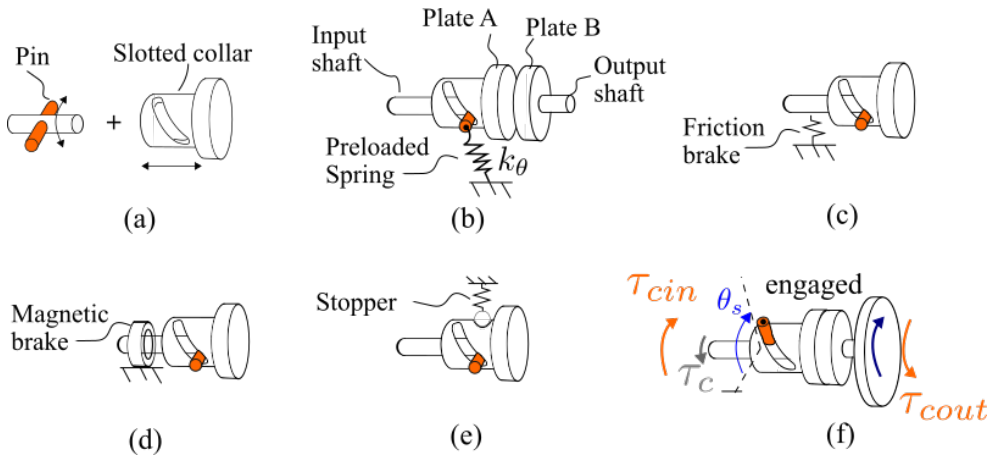

Figure 2-5: Load-sensitive clutch
(a) Spring preload (b)Pin and slot (c) Friction brake type
(d) Magnetic brake type (e) Stopper type (f) FBD of engaged state

2.3 Reduction and torque analysis of LRT

The output torque and speed of the proposed LRT can be analyzed separately for HS and HF phase. Fig.2-6 shows the two-phase operation of the LRT. The blue arrows indicate rotation

direction of the shafts. The orange arrows refer to the torque direction. For simplicity, assume no friction loss in the transmission. Also, assume that the reduction ratio of G1 and G2 ($G1$ and $G2$) are positive.

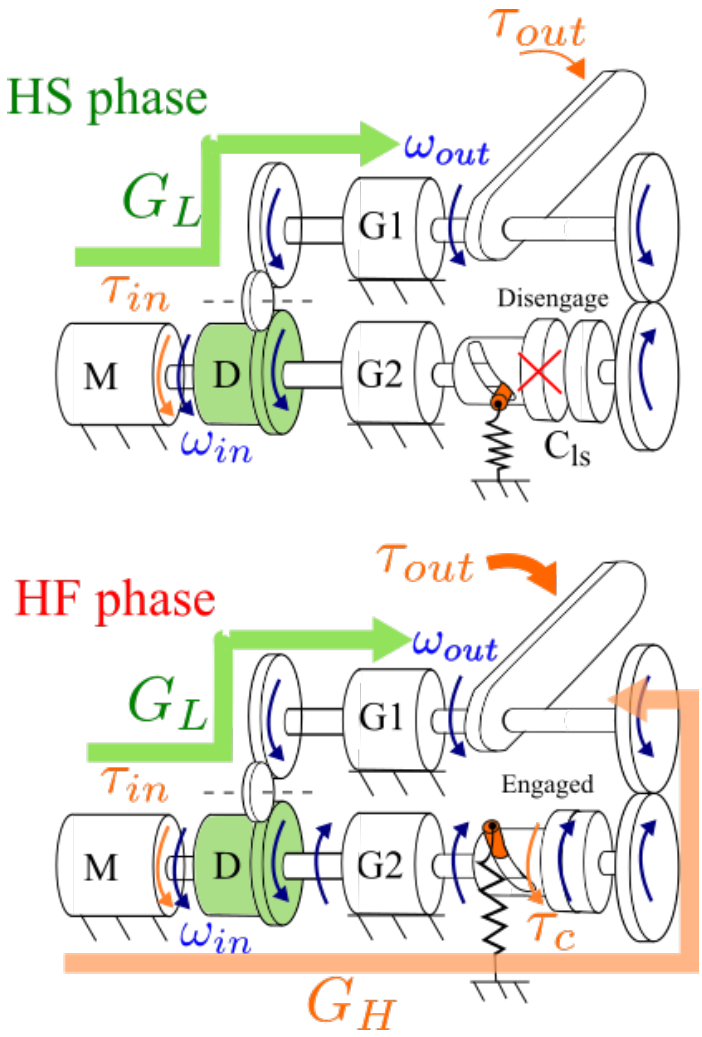

Figure 2-6: Two-phase operations of the proposed LRT

First, consider HS phase where the clutch is kept in a disengaged state during low-load. From Eq.2.3 and 2.6, we can calculate for reduction ratio and τ_{out} by

$$\frac{\omega_{in}}{\omega_{out}} = R_1 G_1 = G_L \tag{2.12}$$

$$\tau_{out} = \tau_{in}(-R_1 G_1) = -\tau_{in} G_L \tag{2.13}$$

where G_L is the effective reduction ratio of the low reduction path including the differential. The minus sign shows that the external output torque is in the opposite direction to the input. In HF phase, the output speed from both low and high reduction have to be equal due to the parallel actuation.

$$\omega_{out} = \frac{\omega_1}{G_1} = \frac{\omega_2}{-G_2} \tag{2.14}$$

From Eq.2.14 and Eq.2.1, solving yields

$$R_2 = \frac{\omega_{in} - G_1\omega_{out}}{-G_2\omega_{out} - G_1\omega_{out}} = \frac{-Z_2}{Z_{in}} \tag{2.15}$$

$$\omega_{out} = \frac{\omega_{in}}{G_1(1 - R_2) - R_2G_2} = \frac{\omega_{in}}{R_1G_1 - R_2G_2} \tag{2.16}$$

With $R_2 < 0$, we defines the effective reduction ratio of the high reduction path $G_H = -R_2G_2 > 0$. The reduction ratio in HF phase can be written as

$$\frac{\omega_{in}}{\omega_{out}} = G_L + G_H \tag{2.17}$$

The output torque, however, has to consider the loss from activating the load-sensitive clutch τ_c as follows

$$\frac{\tau_{out} - \tau_c}{\tau_{in}} = -\frac{\omega_{in}}{\omega_{out}} = -(G_L + G_H) \tag{2.18}$$

$$\tau_{out} = -((G_L + G_H)\tau_{in} - \tau_c) \tag{2.19}$$

where τ_c applies at a different location may result in a slightly different equation. For more general expression, τ_c is replaced by an equivalent threshold torque at motor input τ_{th} and thus Eq. 2.18 can be rewritten as

$$\tau_{out} = -((G_L + G_H)\tau_{in} - G_H\tau_{th}) \tag{2.20}$$

The minus sign indicates that the output torque is in the opposite direction to the input. During the transition from HS to HF phase, the clutch is still in a disengaged state. Therefore, the output torque during transition is simply

$$\tau_{out} = -\tau_{in}G_L \tag{2.21}$$

which is identical to the torque equation for HS phase. Moreover, the clutch closing speed can be calculated as follows,

$$V_c = \frac{A(\omega_{in} - \omega_{out}G_L)}{G_H} \tag{2.22}$$

where V_c is the clutch closing speed. A is a transformation coefficient mapping the G2 output rotation to the clutch translation. A is dependent on the clutch design. For robot grasping, the output link stops moving during the transition and thus V_c can be estimated by setting the $\omega_{out} = 0$

From the analysis, the reduction ratios and output torque equations of the proposed LRT are summarized as follows

HS/transition: $\tau_{in} \leq \tau_{th}$

$$\tau_{out} = -\tau_{in}G_L \tag{2.23}$$

$$R_{HS} = G_L \tag{2.24}$$

HF: $\tau_{in} > \tau_{th}$

$$\tau_{out} = -(\tau_{in}(G_L + G_H) - \tau_{th} G_H) \tag{2.25}$$

$$R_{HF} = G_L + G_H \tag{2.26}$$

2.4 Stiffness analysis

Another advantage of using the clutch mechanism is that during the disengage state, a passively high compliance of the output can be achieved. Fig. 2-7 shows simplified block diagrams of the proposed LRT backdriven by an external force. In the case of (a), the LRT is in HS phase when the backdriving torque is low and could not overcome the clutch preload. The clutch plates are separated by an initial separation distance d_{sep}. If all the gears are backdrivable, the backdrive angle θ_b causes the motor to be backdriven by θ_{inb} through the low reduction path G_L. Therefore, for $\tau_b \leq \tau_{b0}$, the output stiffness can be calculated as

$$k_{out} = G_L^2 k_m \tag{2.27}$$

$$k_m = \frac{\mathrm{d}\tau_{in}}{\mathrm{d}\theta_{inb}} \tag{2.28}$$

where k_m is the stiffness of the motor.

$$\tau_{b0} = \frac{G_L k_s A^2 \theta_0}{G_H} = \frac{G_L k_\theta \theta_0}{G_H} \tag{2.29}$$

A is the transformation coefficient mapping the G2 output rotation to the clutch translation ($x = A\theta_s$). $k_\theta = k_s A^2$ is the effective torsional stiffness. θ_0 is a constant which refers to the effective preloaded rotation. The LRT in HS phase works as a stiff gear with low reduction G_L. If needed, the motor torque τ_{in} can be controlled to regulate the output stiffness actively. Fig.2-7(b) show the case when $\tau_b > \tau_{b0}$. In this scenario, the backdriving motion of the output link causes both the motor and clutch to move. The clutch spring k_s and motor stiffness k_m both acts against the backdrive torque. The backdrive displacement and torque between the spring and motor components are correlated by the differential gear.

From Eq. 2.1 and analysis of the differential gear, we can get the following equations for $x < d_{sep}$, where x is the clutch translation and d_{sep} is the initial separation distance between the clutch plates.

$$\text{Kinematic relationship:} \qquad \theta_b G_L = G_H \theta_s + \theta_{inb} \tag{2.30}$$

$$\text{Torque Equilibrium:} \qquad k_s A^2(\theta_s + \theta_0) = \frac{\tau_b G_H}{G_L} \tag{2.31}$$

$$k_m(\theta_{inb}) = \frac{\tau_b}{G_L} \tag{2.32}$$

Rearranging the term τ_b and substituting $k_\theta = k_s A^2$ yields

$$\theta_b = \left(\frac{G_H}{G_L}\right)^2 \frac{(\tau_b - G_L k_\theta \theta_0 / G_H)}{k_\theta} + \frac{\tau_b}{G_L^2 k_m} \tag{2.33}$$

The output stiffness during the phase transition can be calculated by

$$k_{out} = \frac{\mathrm{d}\tau_b}{\mathrm{d}\theta_b} \tag{2.34}$$

$$\frac{1}{k_{out}} = \frac{1}{(G_L/G_H)^2 k_\theta} + \frac{1}{(G_L)^2 k_m} \tag{2.35}$$

The output stiffness is equivalent to two springs in serial connection to the load. With $G_H > G_L$ the LRT has a stiffness lower than k_θ by a magnitude of G_H/G_L squared. In other words, the LRT exhibits high compliance once it enters the transition phase.

Fig.2-7(c) shows the case when the LRT is in HF phase. Now, the clutch is in an engaged state. The stiffness calculation is similar to that of a high reduction gearbox connected to a motor. Additionally, the clutch spring now acting in the backdrive direction. That is for HF phase

$$\text{Kinematic relationship:} \qquad \theta_{inb} = \theta_b(G_L + G_H) \tag{2.36}$$

$$\text{Torque equilibrium:} \qquad \tau_b = \tau_{in}(G_L + G_H) - k_\theta(\theta_s + \theta_0 - \theta_b) \tag{2.37}$$

$$k_{out} = \frac{\mathrm{d}\tau_b}{\mathrm{d}\theta_b} \tag{2.38}$$

$$= \frac{\partial\tau_b}{\partial\tau_{in}}\frac{\mathrm{d}\tau_{in}}{\mathrm{d}\theta_b} + \frac{\partial\tau_b}{\partial\theta_s}\frac{\mathrm{d}\theta_s}{\mathrm{d}\theta_b} \tag{2.39}$$

$$= (G_L + G_H)^2 k_m + k_\theta \tag{2.40}$$

The equation shows evidently high stiffness compared to the HS/transition phase. The high stiffness is advantageous when large output force is desired.

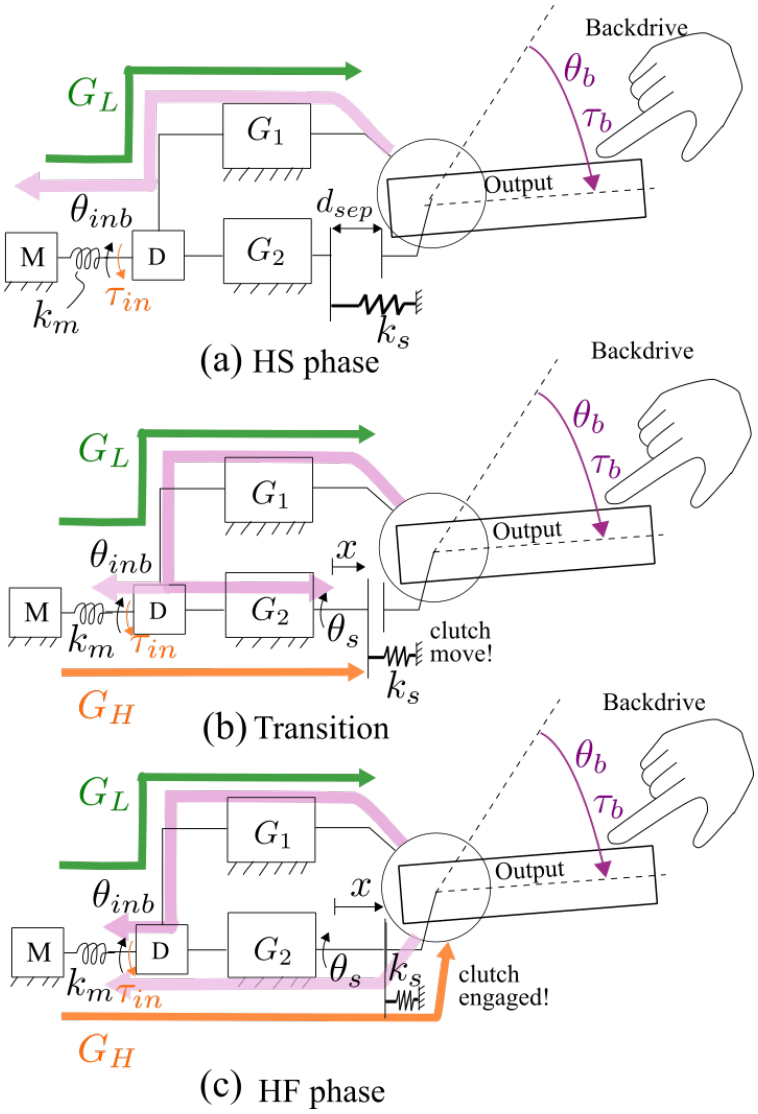

Figure 2-7: Simplified block diagram of LRT with external driving torque

2.5 Design considerations

From the torque analysis section, the LRT can change from HS to HF phase by using the clutch engagement. The first design requirement for the LRT is

$$G_L G_H > 0 \tag{2.41}$$

That is both low and high reduction paths must produce the same output direction in order to drive the output link in parallel. The choice of G_L and G_H depends on the target application. For example, G_H and the motor is sized to produce the target output torque, then G_L is sized to achieve the desired no-load speed. Fig. 2-8 shows the expected change in reduction and output force for the proposed LRT. The output force measured from the force sensor starts with the contact between the link and the object. Then the LRT changes its reduction ratio from HS to HF through a transition state. The time used during the transition is defined by delay A or the transition time t_A which can be estimated as follows, assuming constant motor speed ω_{in}.

$$t_A = \frac{d_{sep}}{V_c} = \frac{G_H d_{sep}}{A(\omega_{in} - \omega_{out} G_L)} \tag{2.42}$$

where V_c is the clutch closing speed found in Eq. 2.22. where A is a transformation coefficient mapping the G2 output rotation to the clutch translation ($x = A\theta_s$). The term ω_{out} can be assumed to be zero for two-phase operation such as grasping where the output link stops moving during the phase transition. Note that although the reduction ratio changes step-wise at the exact moment the clutch engages, the output force increases with time due to the mechanical compliance of the object and the transmission parts. The time used for the output force to reach its peak value since the reduction change is defined by delay B. As there is no infinitely stiff material, delay B is inevitable. However, delay B can be estimated from the motor speed and design parameters by, assuming constant motor speed.

$$t_B = \frac{\tau_{out}}{k_T \omega_{out}} = \frac{(G_H + G_L)^2 \tau_{in} - (G_H + G_L) G_H \tau_{th}}{k_T \omega_{in}} \tag{2.43}$$

where k_T is the total effective stiffness of the mechanical parts and the object. The higher G_H produces a larger output torque but at the same time limits the output speed in HF phase and thus increases the delay B. Note that this applies for all gearboxes with high reduction ratio. To further decrease Delay B, stiffer material or a motor with faster speed can be used.

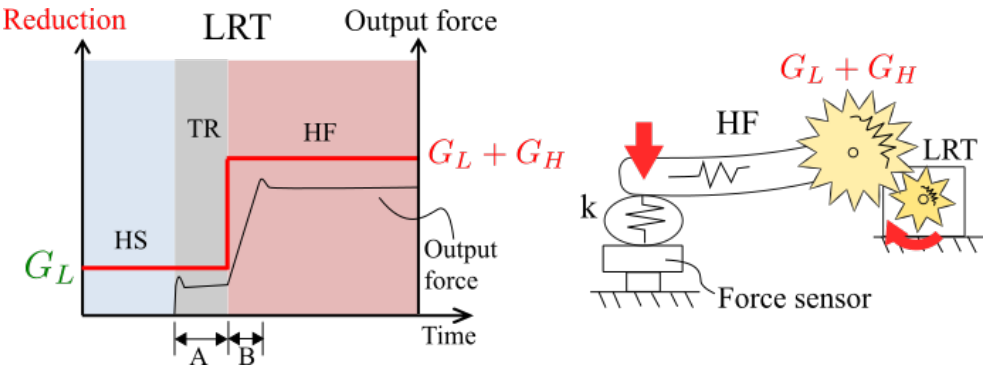

Figure 2-8: Reduction ratio and output force profile of LRT

From the stiffness analysis, the backdriving torque and backdrive angle of the LRT can be plotted as shown in Fig.2-10 in the case of the spring preloaded clutch. The slopes in the graph show the output stiffness at different phases of the LRT. In HS phase, the LRT work as a stiff transmission with low reduction. The output stiffness is dominated by the motor control until τ_b reaches the transition threshold τ_{b0} calculated from Eq.2.29. Then the LRT exhibits a high compliance during the transition until the clutch engages. This compliance characteristics of the LRT can be used for collision safety during high-speed output motion in HS phase. The threshold torque τ_{b0} can be set by design so that the backdrive torque from collision does not exceed a dangerous level before the LRT enter the highly compliant transition phase. This τ_{b0} can also be related to the threshold input torque τ_{th} at the motor by

$$\tau_{b0} + \frac{G_L}{G_H} k_s A d_{sep} = G_L \tau_{th} \tag{2.44}$$

According to Eq. 2.25, the choice of τ_{b0} also affects the expected output torque in HF phase. The higher τ_{b0} would give higher τ_{th} which means less output torque in HF phase, given the same motor torque. However, too low τ_{b0} would cause the LRT to enter phase transition too early and cannot properly accelerate the output link due to the high compliance and low torque. The appropriate choice of τ_{b0} is that it should be more than the output torque requirement during HS phase of the LRT. For example, in grasping application, if the no-load torque required to move the finger link is equal to 100 mNm, τ_{b0} may be set to 150 mNm to ensure that the finger can reach the object without prematurely changing into the slow HF phase. In load lifting application, τ_{b0} might be chosen such that the LRT can handle up to 1 kg in HS phase and changes into HF phase when more than 1 kg load is applied. The choice really depends on the definition between low-load, and high-load determined by the designer. Alternatively, the switching load $G_L\tau_{th}$ can be chosen to map the high efficiency region of the motor to the desired load range as shown in Fig. 2-9. However, for safety reason, τ_{b0} should not exceed the allowable impact torque on both the LRT and the object it collides with. For example, the human pain tolerance of 50 N [44] can be used to determine the maximum value for τ_{b0} . In the case that a high value of τ_{b0} is required, such as when the output link is heavy, a stopper type clutch introduced in Fig. 2-5(e) can be used to produce more output torque in HF phase. Note that variable threshold τ_{b0} is also available if a controllable brake such as a magnetic brake is used to preload the clutch.

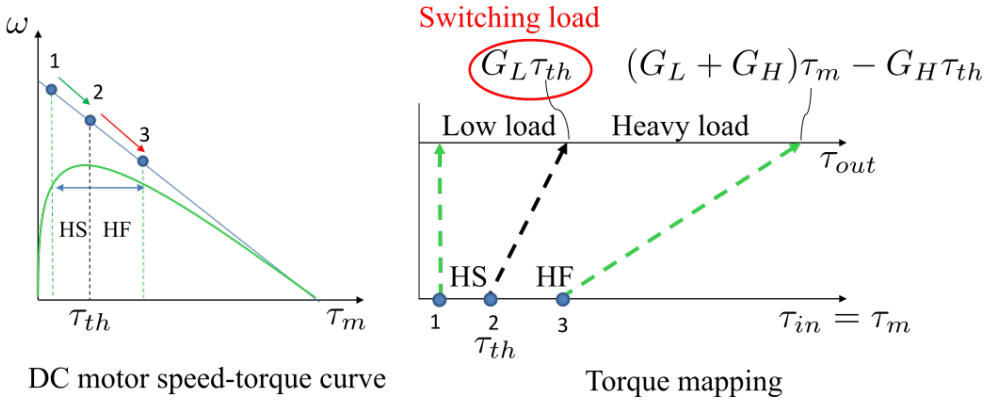

DC motor speed-torque curve

Torque mapping

Figure 2-9: Motor and load torque mapping of LRT

Furthermore, from Fig.2-10, the range of high compliance spans from the end of HS

phase to the maximum backdrive angle θ_{bmax}. If θ_{bmax} is large enough, the output link can be backdriven until the collide object goes out of the link trajectory as shown in Fig. 2-11(a). The minimum requirement for θ_{bmax} is dependent on the target application. For example, in robot arms, θ_{bmax} of at least 90 deg is needed to ensure that the impact load goes out of the arm trajectory if the collision occurs perpendicular to the arm. Some examples of minimum requirements on θ_{bmax} can be found in Fig. 2-11(b) and (c). (b) shows the compliance range determined by the full range of the robot finger, to allow human to backdrive the robot finger far enough to get away from the gripping range. Fig. 2-11(c) shows an alternative use of the compliance characteristic in a robot hip joint with an arbitrary height stair climbing task. In this case, the hip joint can be designed to be backdrivable by the knee joint until the toe touches the ground and the foot aligns in parallel to the stair step. The required θ_{bmax} of the hip joint can be determined kinematically from the leg specifications. Generally, θ_{bmax} can be related to LRT design parameters by

$$\theta_{bmax} = \frac{G_H d_{sep}}{G_L A} + \frac{\theta_{inb}}{G_L} \tag{2.45}$$

In the case that the motor is not backdrivable, the second term is zero. Therefore, θ_{bmax} can be determined from only the first term with d_{sep}. As the reduction ratios G_H and G_L are often determined from the target output torque and speed, d_{sep} can be thought of as the main parameter to change θ_{bmax}. If the initial clutch separation d_{sep} is large, the compliance range of the output joint will be large. Although this provides a better safety margin for the LRT, a wider d_{sep} increases the transition time as the clutch needs more time to close in normal operation.

By examining Eq.2.45 and 2.42, it is evident that there is a design trade-off between the compliance range θ_{bmax} and the transition time t_A. The best practice for LRT design would be to get the transition time as small as possible while ensuring that θ_{bmax} is large enough for safety in the target application. Note that if the target application does not need such compliance range, θ_{bmax} could be minimized, which results in a faster transition time. However, the transition time has to be higher than the expected impact time (Approx. 15

ms as used in [45]) in order to ensure that the LRT behaves compliantly during the impact.

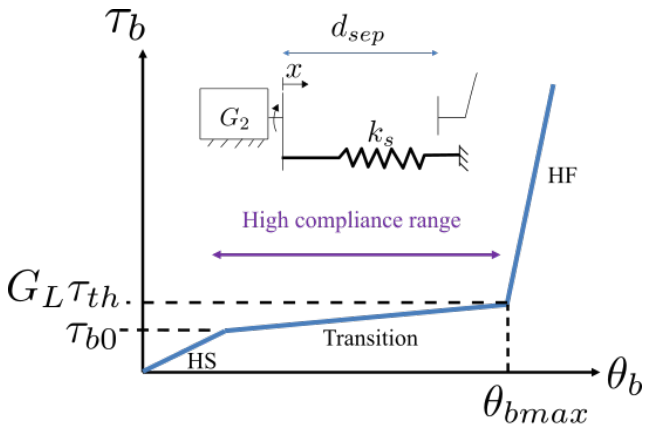

Figure 2-10: Stiffness profile of the LRT

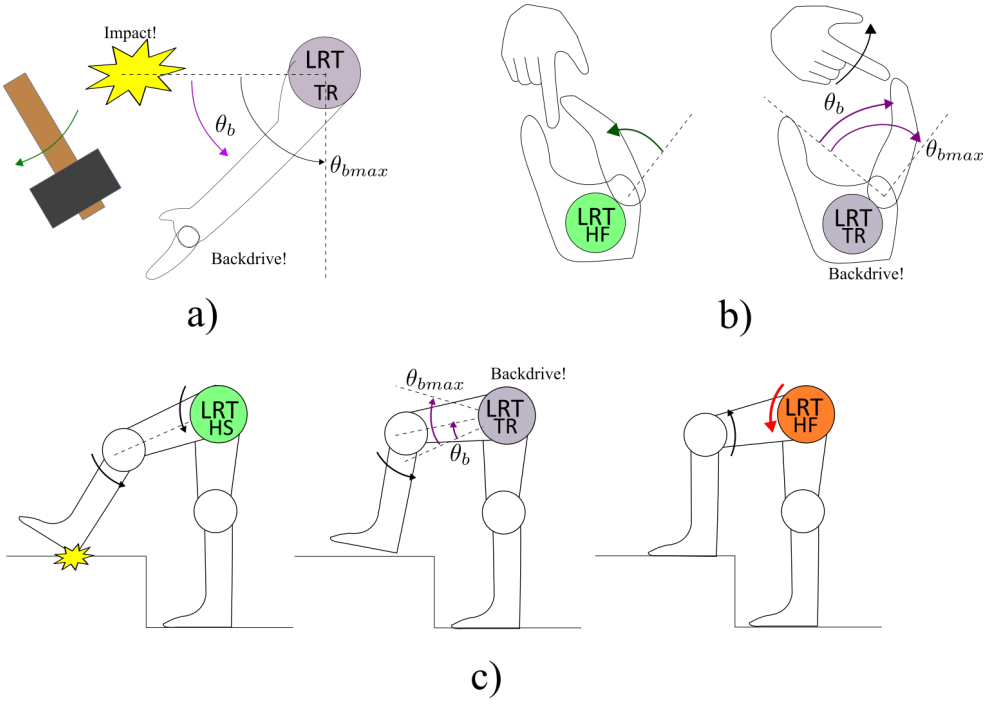

Figure 2-11: Examples of minimum requirement for θ_{bmax}

2.6 Conclusion on the concept

In this chapter, the concept of LRT was introduced. The load-sensitive characteristic is achieved by using a differential mechanism and a preloaded clutch. Mathematical models

of the differential and clutch were discussed in detail with some calculations. Actuation scheme of LRT was discussed with figures to help better understanding of the transmission. Also, calculations of reduction ratios, output torque, as well as requirements for low and high reduction gear trains were discussed in general. Moreover, the stiffness profile of the proposed LRT was analyzed separately in each working phase. The analysis showed that the LRT had high compliance during the phase transition. This characteristic can be used to increase collision safety during high-speed motion of the output link. Lastly, design trade-off between the range of compliance and switching speed, as well as many design considerations of the proposed LRT were discussed in this chapter.

In the following chapters, prototypes robot joint using the proposed concept of LRT are developed. Chapter 3 covers a cable-driven type and Chapter 4 covers a gear-driven type. A novel gear-clutch mechanism is also introduced to be used in the gear-driven type LRT.

Chapter 3

Cable-driven LRT

For a cable-driven robotic finger joint, the finger exerts force onto an object by means of having an actuator pull the cable which is connected to the pulley at the finger base. The proposed cable-driven LRT would be placed in between the motor and the finger joint as shown in Fig.3-1. The role of cable-driven LRT is then to increase the output cable tension F_{out} load-sensitively by changing its working phase from HS to HF when needed. As discussed in chapter 2, a differential mechanism that is well suited for cable-driven application is the movable pulley system. Fig. 3-2 shows a simple double pulley system with a movable pulley acting as a differential. Since the tension force of the cable is the same at any point on the cable, the movable pulley can be used to lift a heavy load. On the other hand, the cable end fixed at the spring can also be considered another output of this movable pulley.

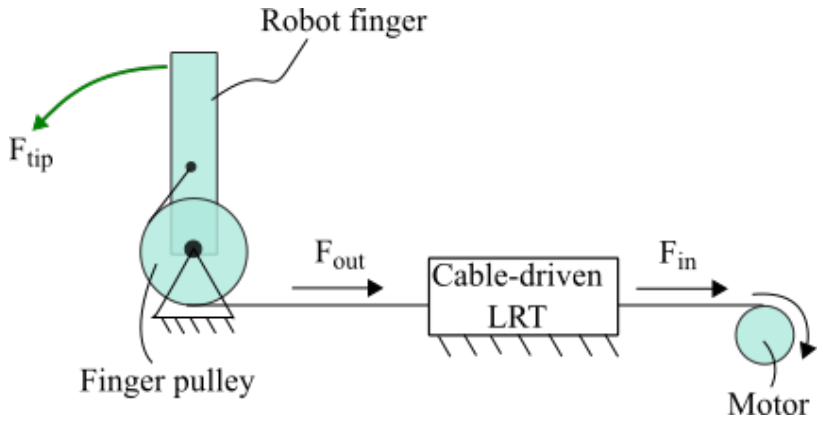

Figure 3-1: Cable-driven finger with LRT

This chapter is divided into two sections. The first section discusses a preliminary design of the cable-driven LRT with a novel split pulley clutch. The second section covers an improved actuation scheme with a rack-tilting clutch to eliminate cable damage problem found in the split pulley clutch design.

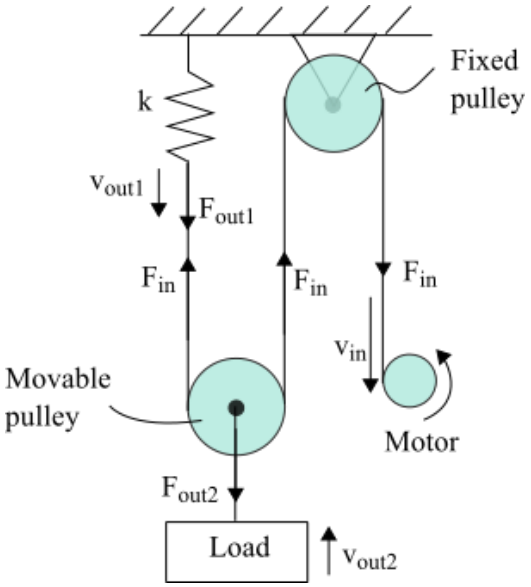

Figure 3-2: Double pulley system

3.1 Split pulley clutch type

3.1.1 Actuation scheme

The basic concept of the split pulley clutch design is shown in Fig. 3-3. For clarity, only the input force F_{in} is shown instead of the motor. The movable pulley of the double pulley system was now split into halves which are connected by a compression spring. The gap between them let the cable passes through or can be closed to grips onto the cable. These halves will be called cable grippers from here onward. Coming from the input side, the cable loops around the cable grippers, wraps around the fixed pulley, then passes through the gap between the cable grippers to a cable-driven robot finger. The cable gripper outer surfaces are assumed to be frictionless. In this configuration, the cable grippers act as both the differential and the load-sensitive clutch of the LRT.

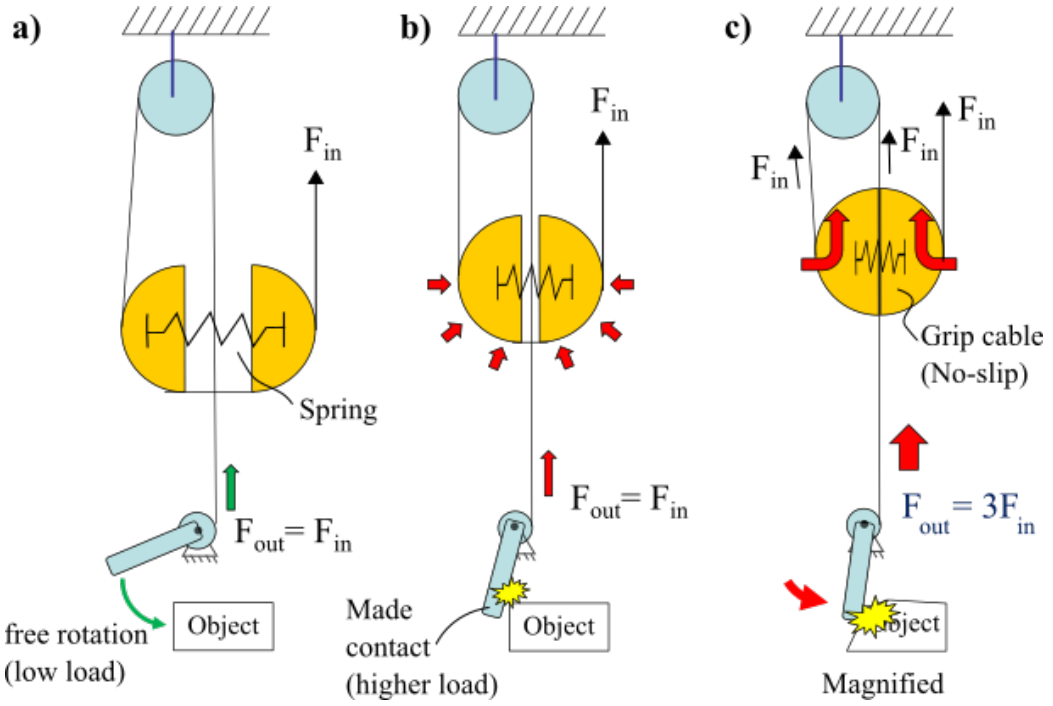

Figure 3-3: Basic concept of the split pulley design

During low load of the finger (a), the gap between the cable grippers is kept opened by the spring. The cable directly connects the input to the output. Therefore the output speed is not reduced (R = 1) and can be used to provide the HS phase of the finger. After the finger contacts an object (b), the increase in load makes the motor pull the cable with a stronger force. (c) The increase in cable tension then causes the spring to compress, and the cable grippers to grip onto the cable. The output force is magnified by the same principle as that of the double pulley system. This process generates the HF phase of the finger. A higher magnification of force is possible by adding more cable loops to the LRT. Fig. 3-4 shows the actuation scheme with the split pulley clutch. The mechanism included one more fixed pulley and some additional components. The cable grippers are guided to slide by the pin slot. A balance plate is used to couple the translation of both cable grippers. A compression spring is used to preload the clutch (cable grippers). The cable starts from the finger side, passes through the gap between the cable grippers and loops around the small fixed pulley. After that, the cable loops around the exterior of the cable grippers and the large fixed pulley, then ends at the motor, indicated by the input force F_{in}. Fig. 3-5 shows the working phases of the cable-driven LRT with the split pulley clutch.

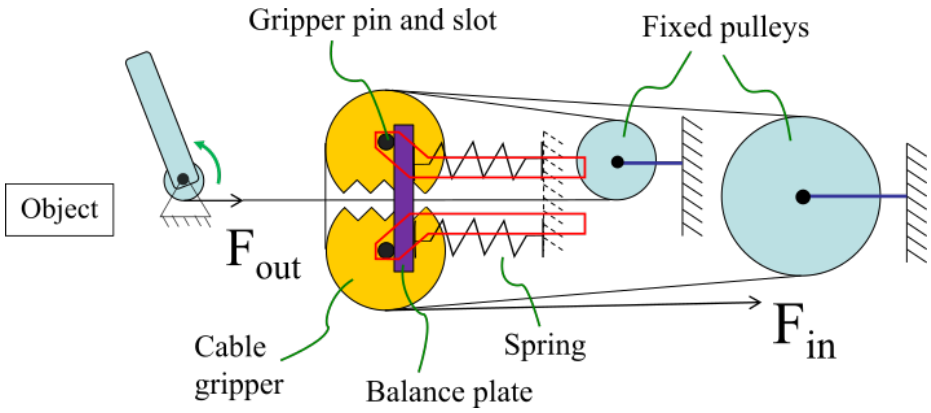

Figure 3-4: Cable-driven LRT with the split pulley clutch

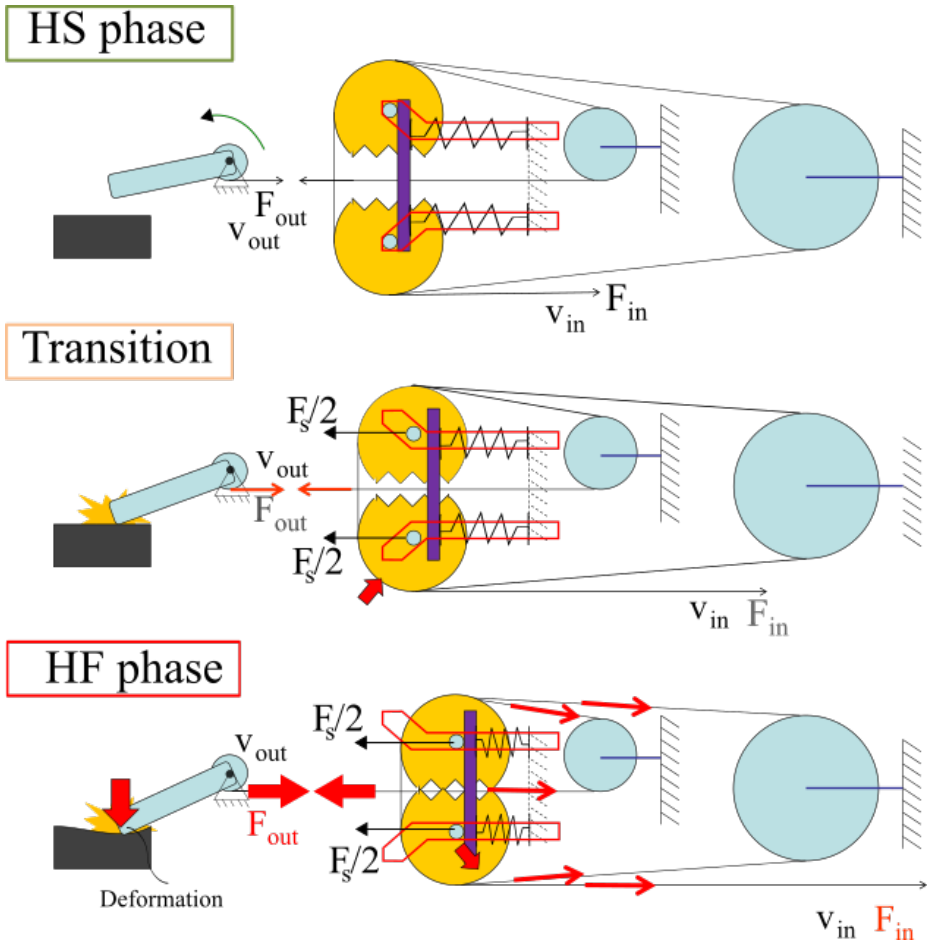

Figure 3-5: Working phases of the split pulley LRT

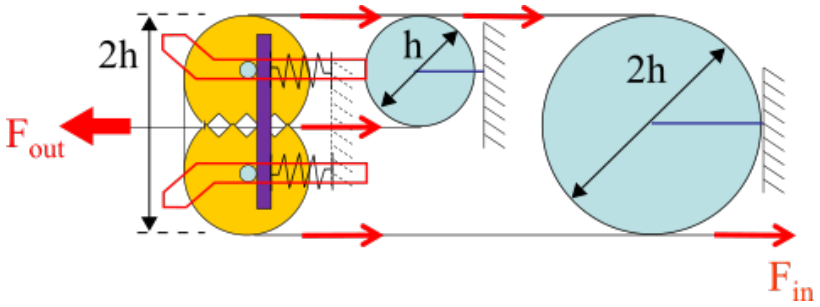

Figure 3-6: Cable grippers and pulley sizing for simplification

3.1.2 Mathematical model

For simplicity, assume that the cable is axially stiff and there is no slippage after the clutch engaged. Also, if the fixed pulleys are sized appropriately as shown in Fig.3-6, the calculation can be greatly simplified as all the pulling forces are aligned horizontally. From Fig. 3-5, one can define G_L and G_H of the LRT by

$$G_L = 1 \tag{3.1}$$

$$G_H = 2N_b \tag{3.2}$$

where N_b is the number of cable loops bound around the fixed pulley and cable grippers. In Fig. 3-5, $N_b = 2$. The reduction ratio in HS and HF from Eq. 2.24 and 2.26 can be calculated as follows

$$R_{HS} = G_L \tag{3.3}$$

$$R_{HF} = G_H + G_L \tag{3.4}$$

The governing equations for output force in HS/transition are:

$$F_{out} = \eta_L G_L F_{in} \tag{3.5}$$

and for HF phase:

$$F_{out} = (\eta_L G_L + \eta_H G_H) F_{in} - \frac{F_s}{2N_b} G_H \tag{3.6}$$

where η_H and η_L are the transmission efficiency of the high and low reduction path, respectively. F_s is the spring force and can be calculated from $F_s = k_s(x + x_0)$.

3.1.3 Split pulley prototype

A prototype was developed to demonstrate the proposed actuation concept. Fig. 3-7 shows the prototype. The balance plate was placed away from the cable gripper pins and was connected together by the links to make both cable grippers move horizontally together. This adjustment does not effect the working concept of the mechanism. Fig. 3-8 shows the grippers and fixed pulleys, which were made of brass and sized according to Fig. 3-6. The grippers and fixed pulleys were grooved to house the cable. The 3 mm hole in the center was designed for pin insertion. The balance plate and the mechanism frame were made of aluminum alloy. The prototype was 21mm $\times$ 38 mm $\times$ 180 mm in size and weighed approximately 280 g. A ϕ0.69-mm Kevlar rope was used as the driving cable. The compression spring had a spring constant of 1.28 N/mm with minimal preload.

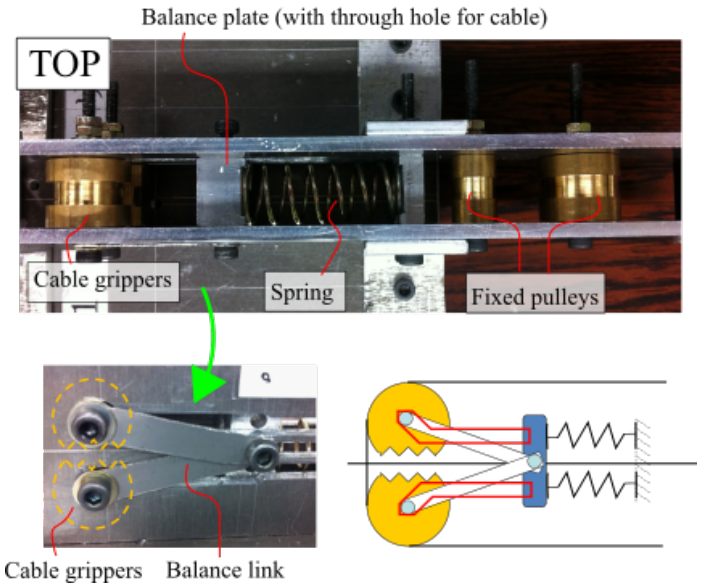

Figure 3-7: Prototype of the cable-driven LRT with split pulley clutch

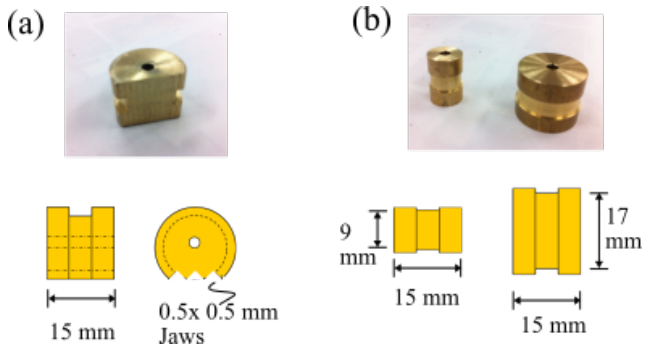

Figure 3-8: Cable grippers and fixed pulleys specifications

(a) Cable grippers b) fixed Pulleys

3.1.4 Experiment and Discussion

In this preliminary concept, the ability to load-sensitively switch its reduction ratio were verified by the following experiment. Fig. 3-9 shows the experiment setup.

A force sensor was used to measure the output cable tension forces F_{out} when supplied by input forces F_{in}. The relationship between output and input forces were examined. The entire mechanism assembly was fixed firmly on a jig plate together with a force sensor connected at the output side. The input force F_{in} was supplied by water weights.

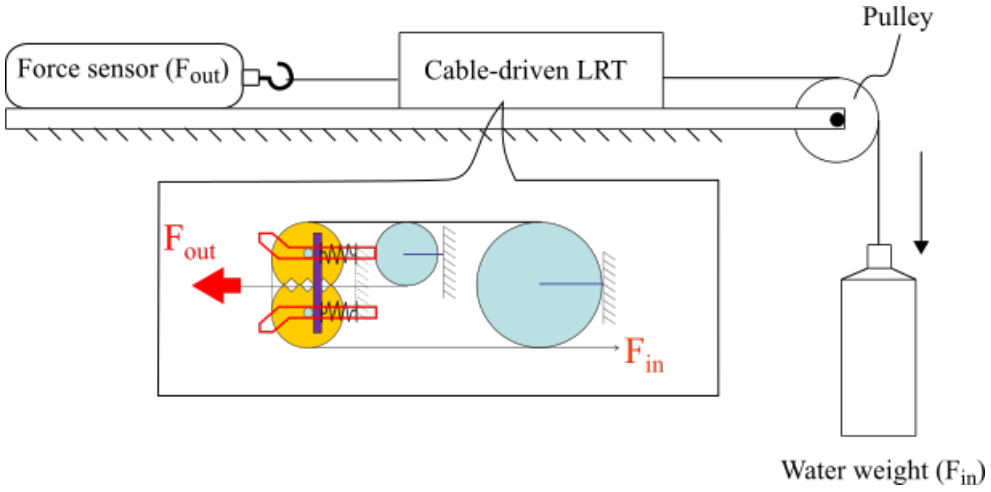

Figure 3-9: Experiment setup for measurement of force magnification

Although the cable grippers were assumed to have no-slip condition on the gripping surfaces. In reality, as shown in Fig. 3-10, the generated output force in HF phase is limited by the gripping capability of the cable grippers. Therefore, the experiment was separated

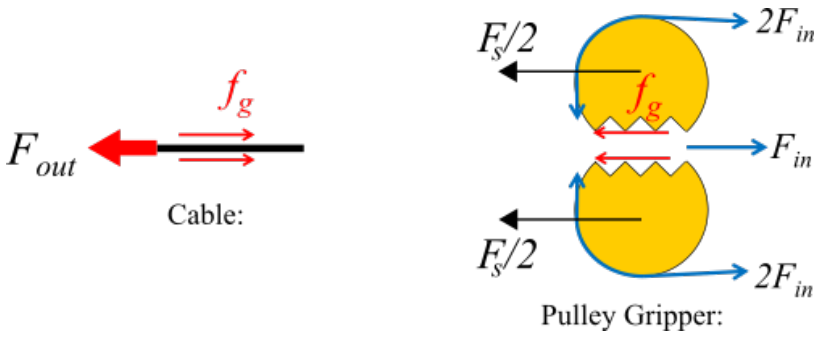

Figure 3-10: Output and gripping force relation

into two cases shown in Fig. 3-11 with case B has higher expected cable gripping force than case A based on the difference in cable binding method around the cable grippers.

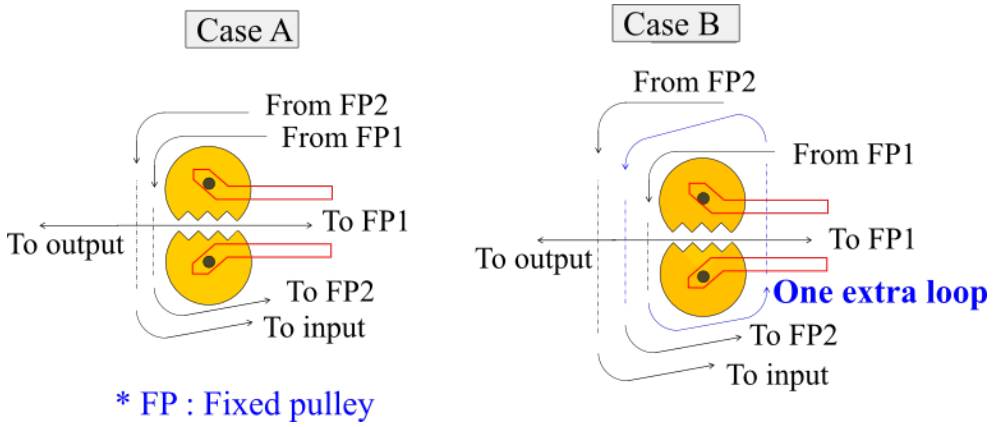

Figure 3-11: Experiment cases of the force magnification measurement

- Case A) Normal binding: In this case, the cable binding method was the same as previously introduced in Fig. 3-6.

- Case B) Double binding: There was an additional binding loop around the cable grippers on top of the normal binding in case A. Case B was expected to produce more cable gripping force, thus higher gripping capability than case A.

Fig. 3-12 shows the experiment results for both cases. The results were averaged from three measurements. The green line represents the theoretical direct drive line ($F_{out} = F_{in}$) if the LRT works in purely HS phase. The red line in the spring displacement graph refers to the travel limit of the cable grippers which was limited by the pin slot.

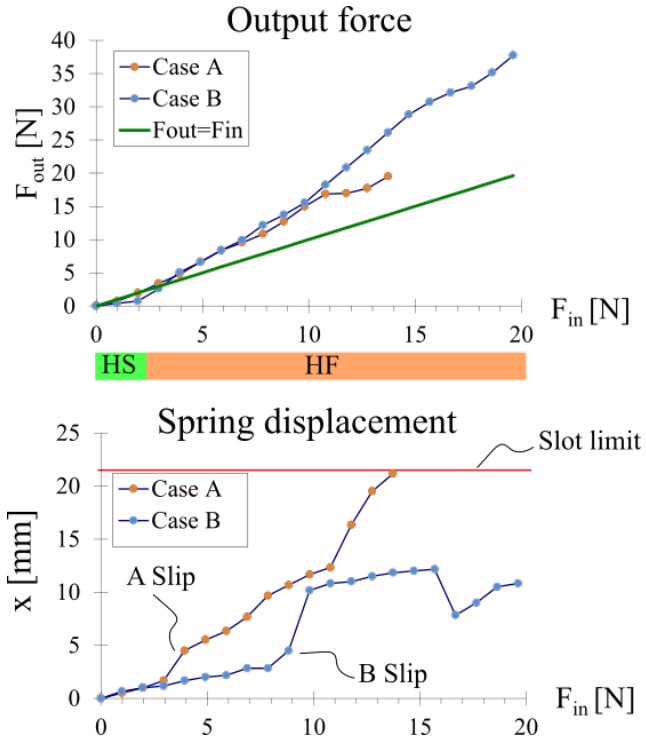

Figure 3-12: Force magnification experiments of the split pulley prototype

Case A slipped and hit the slot limit at lower F_{in} when compared to case B. This means that case B has more gripping capability than case A as expected. The reason why case B slipped was that of cable fraying from several attempts of gripping at the same point. Closer inspection showed that cable gripper entered the engaged state at around 1 N of input force for case A and just before 2 N for case B. The force output can be divided into two parts as the slope change. One before the engage point designated as HS phase and one after designated as HF phase. HS outputs were lower than the direct drive line while the HF output had a higher slope than the direct drive line. Therefore, the results verifies that the LRT with split pulley clutch could increase the reduction ratio and output force load-sensitively.

By rewriting Eq. 3.5 and 3.6 in the following form, transmission efficiency η_L and η_H can be calculated from the experiment results.

$$F_{out} + F_s = (\eta_L G_L + \eta_H G_H) F_{in} - f_l \tag{3.7}$$

where f_l is friction loss that was not included in the math model such as friction from the translation of the balance plate and the spring part. F_s were calculated from $F_s = kx$.

Table 3.1: Calculation results on experiment data

Case	η_L	η_H	f_l[N]
A	0.7	0.69	3.0
B	0.4	0.63	3.1

The experiment results show that although case B has higher gripping capability and less slippage, the transmission efficiency is evidently lower than that of case A. This is because of the additional loop of cable in case B introduced more friction loss along the cable line. This phenomenon is known as capstan friction or belt friction as illustrated in Fig. 3-13, where μ refers to the coefficient of friction between the rope and the surface. ϕ refers to contact angle of the rope in radian. The capstan friction equation is

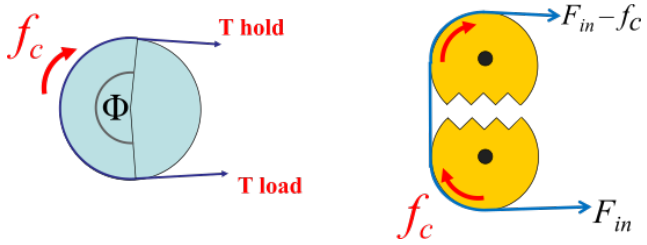

Figure 3-13: Capstan friction and its effect on the cable grippers

$$f_c = T_{load} - T_{hold} = F_{in}(e^{\mu\phi} - 1) \tag{3.8}$$

As ϕ increases from the additional loop in case B, the capstan friction also increases along the cable gripper outer surface. The capstan friction causes the cable tension to gradually decrease along the cable path; which results in a lower total pulling force acting on the cable grippers.

In conclusion, the split pulley design of a cable-driven LRT was proposed. The prototype was experimentally verified that it could change from HS to HF phase load-sensitively. The reduction ratio of the HF phase can be increased by adding more cable loops around the grippers and the fixed pulley. However, for higher loops of cable, the capstan friction

limits the efficiency and the expected force magnification. Capstan friction can be useful in applications that need to hold larger load with a small force such as in rope rescue [46], tendon locking mechanism (TLM)[47] and the capstan brake for tendon-driven mechanism [48]. However, it is counter productive in the split-pulley clutch design.

3.1.5 Problems and possible improvements

As discussed above, the main issues to the performance of the split pulley design are slippage in gripping, and capstan friction. The direct cable gripping method used in this design could not effectively transmit all the pulling force to the output side of the cable. Moreover, capstan friction caused the cable gripper to tilt and produced a pressure point when gripping onto the cable. This pressure point contributes to the damage and slippage of the cable. Fig. 3-14 shows the cable damage after several gripping attempts.

Although the prototype was sufficient to demonstrate the concept of a cable-driven LRT, the problem of cable damage limits its usage to low force applications. Developments of stronger cable materials or cable coating techniques in the future might help increase the usefulness of the design. In the next section, an alternative clutch design is used to solve these cable slippage and damage by avoiding direct cable grip.

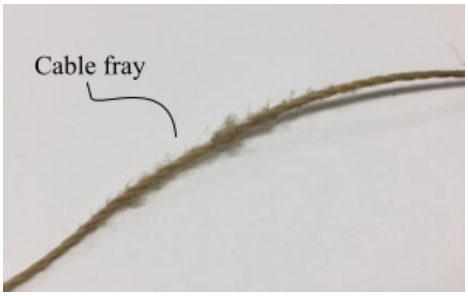

Figure 3-14: Cable fraying from multiple gripping

3.2 Cable-driven LRT with rack-gear clutch

This design uses rack and gear as a clutch instead of the cable grippers. Fig. 3-15 shows how the rack-gear engagement can be used to drive the output cable. The cable connects

the robot finger on one end and a fixed point on gear hub on another end. When the rack is driven to the left, the gear rotates and pull the cable on the finger side. Note that this clutch design does not directly grip onto the cable. Therefore, it could potentially solve the cable damage and slippage problem found in the split pulley design.

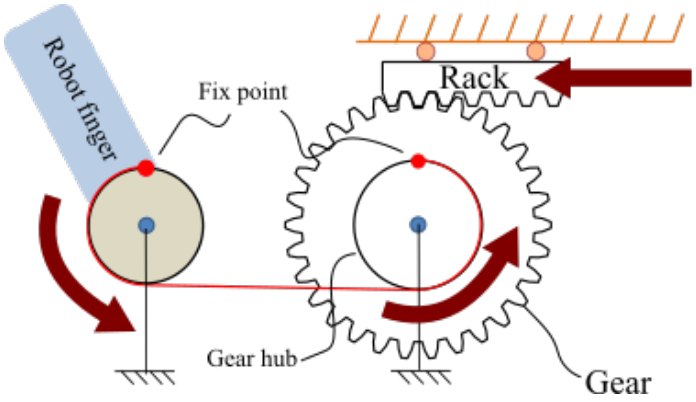

Figure 3-15: Rack-gear clutch for cable-driven finger

Combining the simple rack-gear clutch with a differential unit using movable pulleys, Fig.3-16 shows the concept of the transmission. The cable is now separated into two segments. The first segment connects the finger and gear hub. Another segment starts at the fixed point on gear hub, loops around Pulley Set 1 and 2 and then connects to the motor shaft. Pulley set 1 consists of several pulleys (three pulleys in the figure) which independently rotate around the same fixed axis. Pulley set 2 also contains the same number of pulleys as Set 1, but is instead rotates around an axis placed on a movable platform called rack carrier. Therefore, the Pulley Set 2 is a group of movable pulleys. The rack is set on the rack carrier to move together with Pulley Set 2. In this arrangement, the Pulley Set 2 now work as a differential mechanism where one of its output is the cable end fixed at gear hub, and the other output is the rack carrier translation. With a preload spring bias to the rack carrier unit, we now have a rack-gear clutch which changes its engage/disengage state load-sensitively for the cable-driven LRT. The rack-gear initial separation distance is designated as d_{sep}. The spring preload length is x_0. The number of cable loops around both Pulley sets is referred to as N_b.

In actual design, the fixing point on the gear hub can be simplified by multiple binding of cable around the gear hub. Due to capstan friction equation in Eq. 3.8, if ϕ is large

enough, the cable will not slip on the gear hub. This allows the use of continuous cable and simplify the transmission assembly.

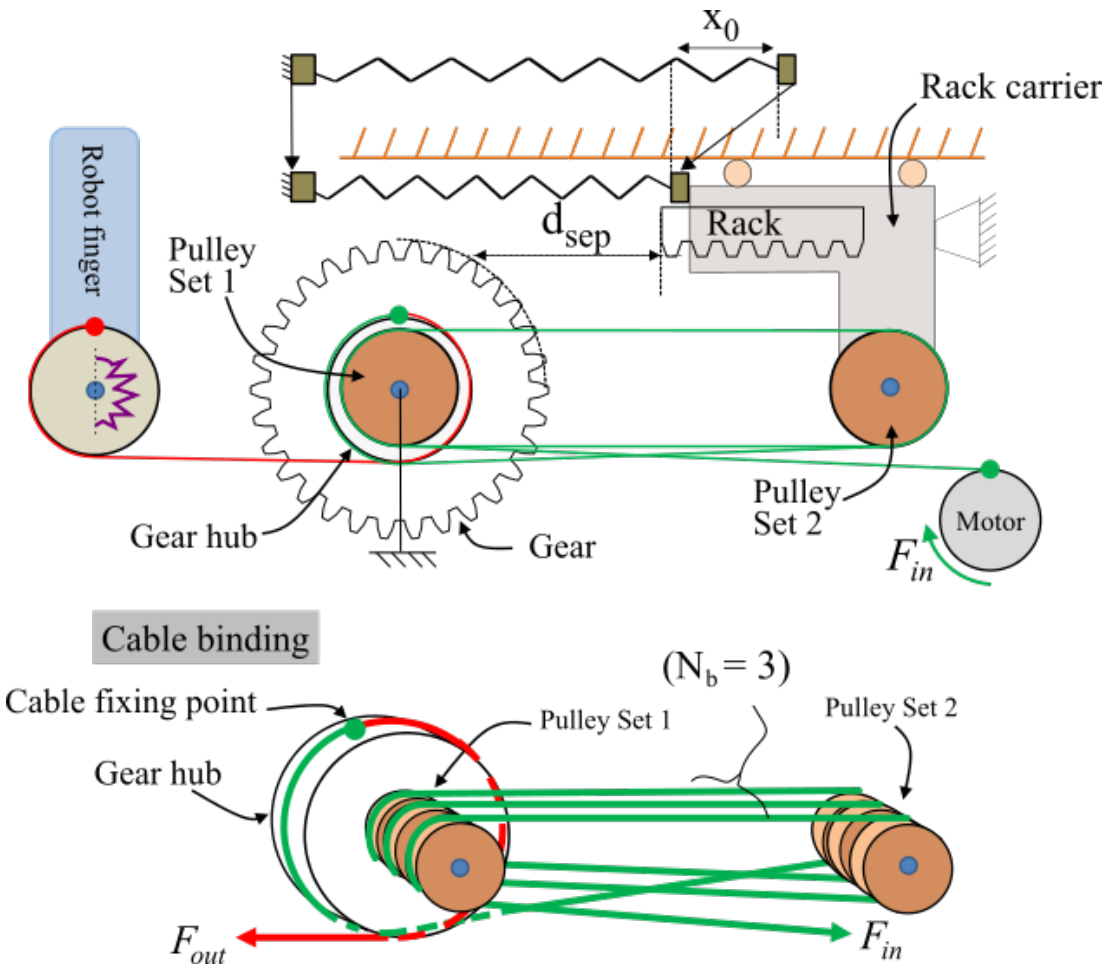

Figure 3-16: Concept of cable-driven LRT with a rack-gear clutch

Mathematical model of the cable-driven LRT

Fig. 3-17 shows the working phases of the LRT.

- High-speed phase (HS): When the output load is low such as when the finger has no contact with the target object, the LRT acts as a series of fixed pulleys and has no reduction in speed.

- Transition: After the finger touches the target object, the motor pulls the cable to shorten its path. This action moves the rack unit toward the gear. During phase

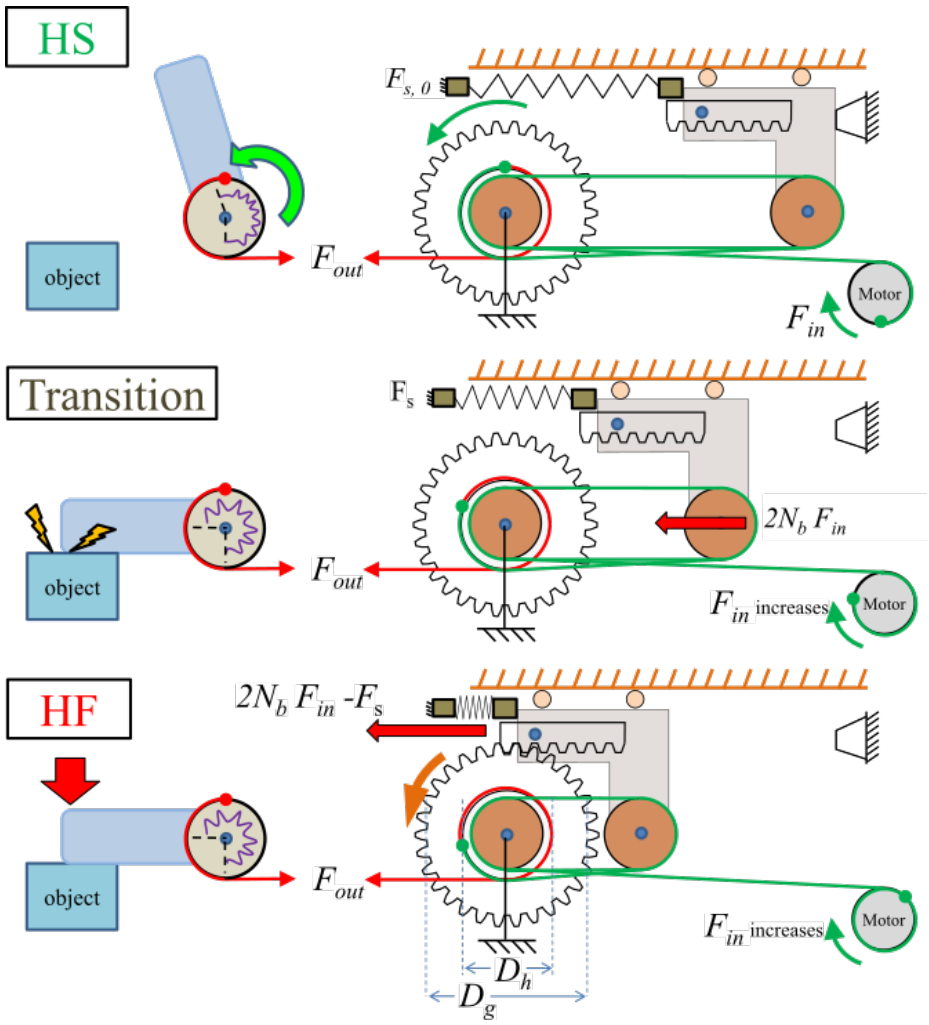

Figure 3-17: Working phases of the cable-driven LRT with rack-gear clutch

transition, the tension force from the motor directly drives the finger.

- High-force phase (HF): Eventually the motor pulling force is sufficient for the rack to engage the gear. At this moment, the reduction ratio of the mechanism abruptly changes into HF phase.

- Return: Because the cable can only transmit pulling but not pushing action, a torsion spring at the finger joint is used to provide the retraction torque. Also, since the HF phase has high stiffness as discussed in chapter 2, the motor has to turn in reverse, lowering the cable tension and allow the compression spring to disengage the rack-gear clutch before the finger can be retracted. Further considerations for choosing

the torsional springs and compression spring are discussed later.

In quasi-static equilibrium, the reduction ratios can be described in analogy to the analysis in Chapter 2.

$$G_L = 1 \tag{3.9}$$

$$G_H = 2N_b \frac{D_g}{D_h} \tag{3.10}$$

$$R_{HS} = G_L \tag{3.11}$$

$$R_{HF} = G_L + G_H \tag{3.12}$$

where N_b is the number of cable binding loops around Pulley set 1 and 2. D_g and D_h refer to pitch diameter of gear and gear hub, respectively. The output cable tension force F_{out} can then be written as follows, assuming no friction loss.

$$F_{out} = \eta_L G_L F_{in} \quad ; F_{in} \leq F_e \tag{3.13}$$

$$F_{out} = (\eta_L G_L + \eta_H G_H) F_{in} - \frac{F_s}{2N_b} G_H \quad ; F_{in} > F_e \tag{3.14}$$

where F_s is the compression spring force and F_e is the input force needed at the point of rack-gear engagement. F_e can be calculated from the following function of the spring stiffness k_s, preload length x_0, N_b, and d_{sep}.

$$F_e = \frac{k_s(d_{sep} + x_0)}{2N_b} \tag{3.15}$$

Note that F_{out} is the output cable tension, not the output fingertip force. Therefore, the effects of the torsional spring at the finger joint is not included in the equations.

The preload spring force at the rack carrier must be high enough to hold the rack unit in place during the entire HS movement of the robot finger. Let the minimum requirement of cable tension to fully flex the finger against the torsion spring be F_{rq}.

$$k_s x_0 \geq 2N_b(F_{rq}) \tag{3.16}$$

According to Eq.3.14 and 3.15, a higher preload will result in a lower expected output force F_{out}. Therefore, the spring preload should be chosen as low as possible according to the above condition.

Rack-tilting mechanism

There is a possibility of jamming between the rack and gear teeth during the clutch engagement. Fig.3-18 shows the jamming scenario. The jamming force N_j acts toward the gear center, causing the rack to get stuck, unable to rotate the gear. To overcome this problem, a rotation axis is added to the rack holder. Fig. 3-19 shows the rack tilting mechanism introduced in [40]. By properly placing the rotation axis, the rack can be tilted by the jamming force and slip into proper engagement with the gear. The proper position of the rotation axis can be determined by analyzing the difference in normal reaction forces during meshing and jamming state of the rack-gear clutch. In jamming, the force N_j acts normal to the gear teeth jamming surface, which is in the radial direction to gear center point. The rack can be tilted clockwise by N_j if the rotation axis is placed to the right of the N_j line. The tilting action allows the rack to continue moving into engagement with the gear. After the rack meshes with the gear teeth, the meshing force N_m now acts perpendicular to the engaged tooth surface. The exact direction of N_m can be determined from the pressure angle of the gear teeth. If the rotation axis is placed to the left of the N_m line, the counter-clockwise moment presses the rack against the base. This action keeps the rack straight throughout the rack-gear engagement and is referred to as a stable meshing. In conclusion, the rotation axis has to be placed in between N_j and N_m line for the rack-tilting mechanism to engage without jam and mesh stably after the engagement. A test model was developed to verify the concept of the rack-tilting mechanism. Fig. 3-20 shows the test model. Both the rack and the gear were designed with the standard involute tooth profile [49]. The test was conducted by hand. A) The output gear and link were pushed against the stopping pin to lock

the gear rotation in an angle that the rack will experience jamming. B) the rack-tilting unit was pushed to jam with the gear tooth. C)By continue pushing the rack unit toward the gear, the rack tilted clockwise due to the jamming force and slipped passed the jamming point. D) The rack engaged the gear and kept it straight posture by the meshing force.

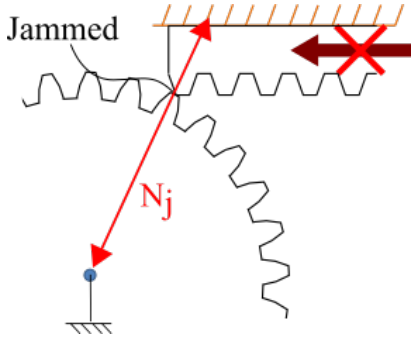

Figure 3-18: Gear teeth jamming problem of the rack-gear clutch

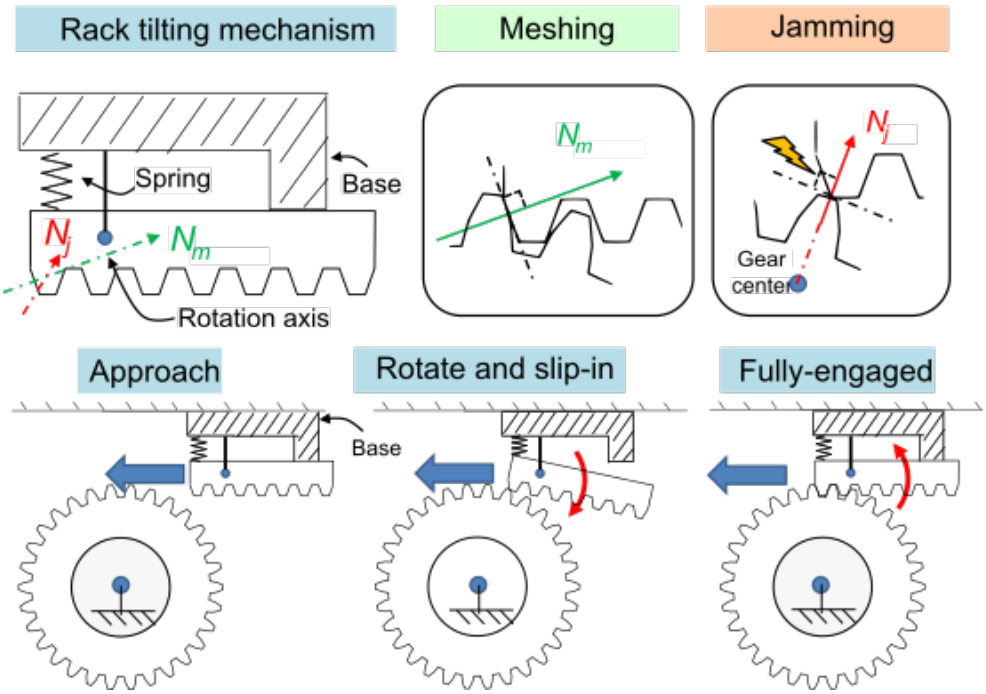

Figure 3-19: Rack tilting mechanism

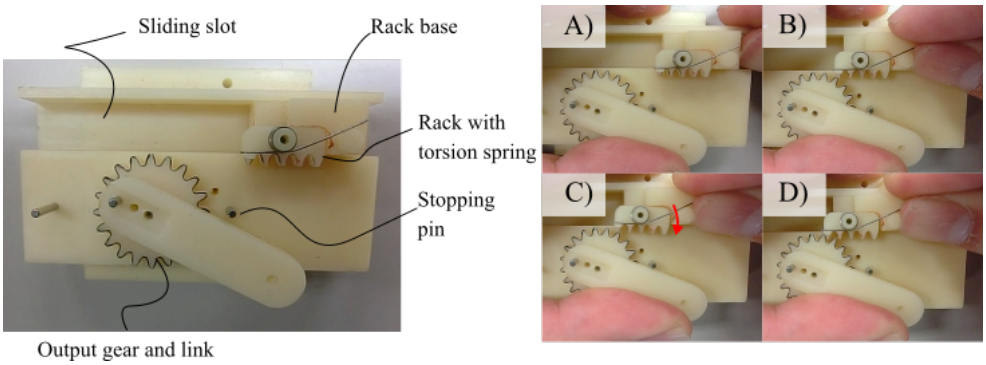

Figure 3-20: Test model of the rack-tilting mechanism

Compliant behavior of the cable-driven LRT

Since the HS phase provides a direct drive ($G_L = 1$) from the motor. The stiffness in HS phase is equal to the motor stiffness as discussed in Chapter 2. During the transition, the stiffness drops as the spring is compressed. If the spring preload $k_s x_0$ is low enough, the LRT can enter the low stiffness region with low backdriving force at the finger. Also, if the motor itself is backdrivable, which is usually the case with low reduction motor, the stiffness during HS phase will also be low. This compliant behavior of the LRT can help limit potential damage when a collision occurs. Fig. 3-21 shows the scenario when the robot finger collides with a nearby human hand during its fast motion in HS phase.

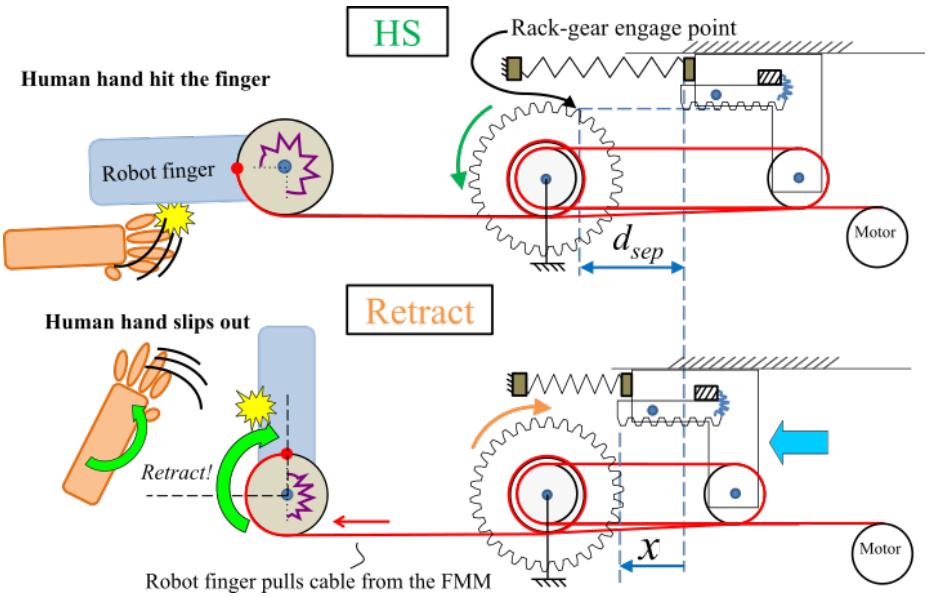

Figure 3-21: Compliant behavior of the LRT when subjected to a shock load to the output

The human hand applies a shock load to the output and pull the cable from the output side by retracting the robot finger. The LRT, experiencing this shock load then starts its phase transition and move the rack by an amount x. As long as $x < d_{sep}$, the high compliance of LRT will allow the finger to be back-driven without much resistance. As discussed in chapter 2, increasing the d_{sep} would widen the high compliance range of the finger. However, an excessive d_{sep} would increase the mechanism size as well as increase the rack traveling time to engage. The minimum requirement of d_{sep} for full stroke retraction can be calculated from the finger specification. Defining the maximum cable length pulled in a total retraction of a particular robot finger by x_{max}, the minimum condition for d_{sep} is then

$$d_{sep} \geq \frac{x_{max}}{2N_b} \tag{3.17}$$

3.2.1 Cable-driven LRT prototype for robot finger joint

A simple underactuated cable-driven robot finger was developed to demonstrate the concept of cable-driven LRT. Underactuation was chosen because of its popularity with cable-driven robot fingers [50, 51, 52, 53, 54, 55, 56, 57].

2-DOF finger design

The target pinching force was set to 20 N and the finger closing time was set to 0.5 s. The target force is approximately equal to the maximum pinching force against palm of an anthropomorphic finger in VU Hand[58].

Fig. 3-22 shows the finger design. The finger has two links with length L_1 and L_2, and two rotation joints with pulley radius R_1, R_2. At each joint, there is a torsion spring with a stiffness of k_1 and k_2, respectively. The fingertip position is described by height H_{tip} and its distance from the finger center L_{tip}. F_{out} is the output cable tension force from the LRT. The proportions of the finger links and joint pulleys were designed so that the finger has a stable pinching posture, similar to those in [59, 60].

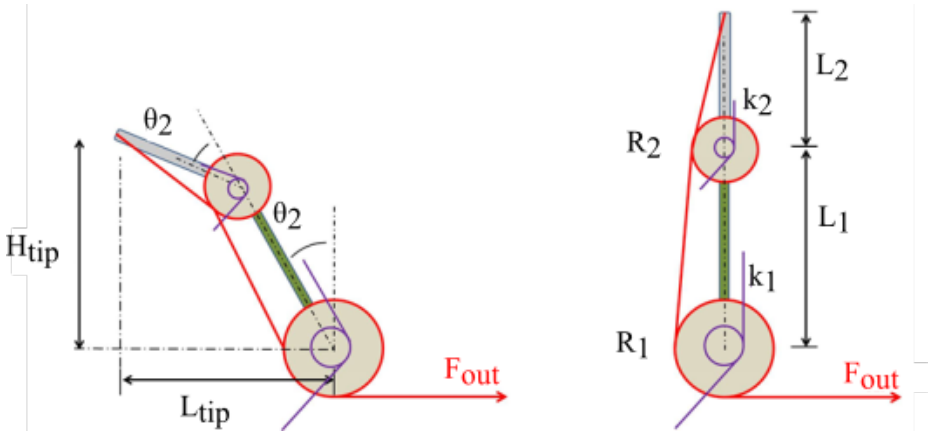

Figure 3-22: 2-DOF underactuated finger

For an underactuated finger to be able to maintain pinching posture stably, torques at the finger joints must be in balance with the fingertip force. Consider the simplest case of a straight finger pinching on an object in Fig. 3-23.

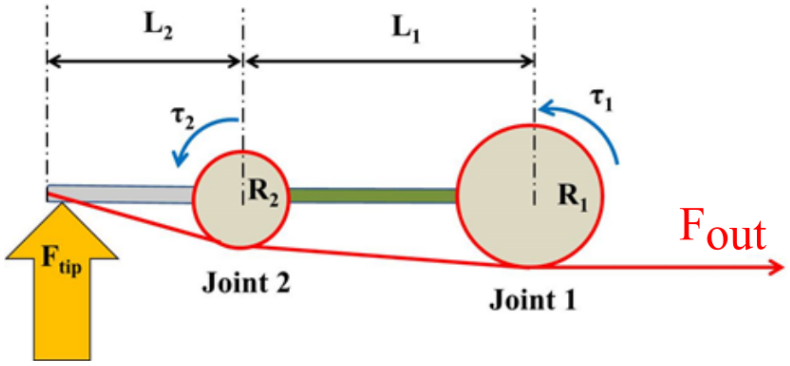

Figure 3-23: FBD of a straight finger in static equilibrium

$$\tau_1 = F_{out} R_1 = F_{tip}(L1 + L2) \tag{3.18}$$

$$\tau_2 = F_{out} R_2 = F_{tip}(L2) \tag{3.19}$$

$$\frac{R_1}{R_2} = \frac{L_1 + L_2}{L_2} \tag{3.20}$$

The sizes of the finger pulleys must obey Eq. 3.20 to statically maintain the straight pinching posture. From the equations, it is clear that R_1 must be larger than R_2, so that the proximal joint can produce a larger torque than the distal joint during pinching. In the

case that $R_2 < R_1 \leq (L_1 + L_2)R_2/L_2$, the finger has insufficient torque τ_1 at the proximal joint to maintain the straight posture. The finger then flexes inward until it reaches a new equilibrium pinching point. Fig. 3-24 illustrates such case. Another extreme case is when $R_1 \leq R2$. There is no equilibrium pinching point, and the finger cannot perform a stable pinching operation. This setting may be suitable for releasing mechanism in Soft gripper [50] but cannot be used in pinching application.

For simplicity, Eq.3.20 in the straight pinching model was used to design the finger links and pulleys. The torsion spring stiffnesses were chosen to provide a natural closing trajectory [60, 61] during HS phase, where θ_1 approximately equals to θ_2. Table. 3.2 lists the specification of the finger. The finger size was roughly the size of a human thumb.

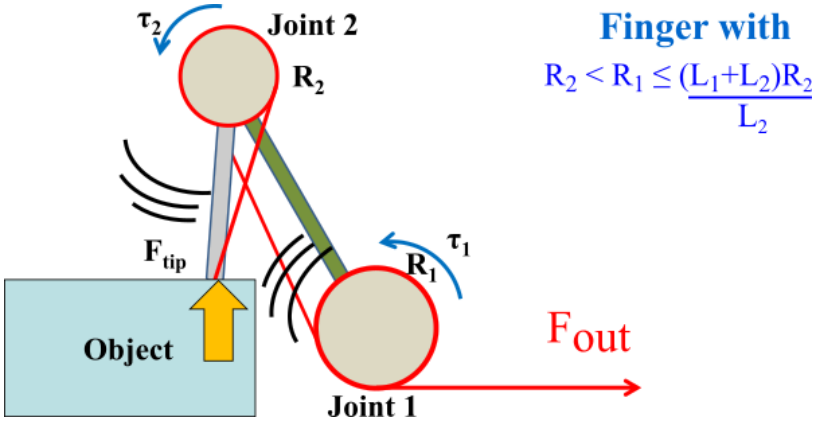

Figure 3-24: Finger behavior with insufficient τ_1

Table 3.2: Specification of the designed robot finger

Specification	Variable	Value
Link 1 length	L_1	30 mm
Link 2 length	L_2	20 mm
Joint 1 pulley radius	R_1	10 mm
Joint 2 pulley radius	R_2	4 mm
Joint 1 torsion stiffness	k_1	0.141 mNm/deg
Joint 2 torsion stiffness	k_2	0.059 mNm/deg
Joint 1 rotation preload	$\theta_{1,0}$	20 deg
Joint 2 rotation preload	$\theta_{2,0}$	20 deg
Joint 1 rotation maximum limit	$\theta_{1,max}$	75 deg
Joint 2 rotation maximum limit	$\theta_{2,max}$	90 deg

From the finger specifications, other two values need considerations. One is the cable tension F_{rq} required for the finger to reach the pinching position. Another is the max cable

length needed for full finger retraction x_{max}. These two values will play an important role in LRT design which will be discussed later. Fig. 3-25 shows the finger in a pinching posture at $H_{tip} = 0$. The following equations were used to calculate F_{rq} and x_{max} from the finger geometry. The calculated values are summarized in Table 3.3.

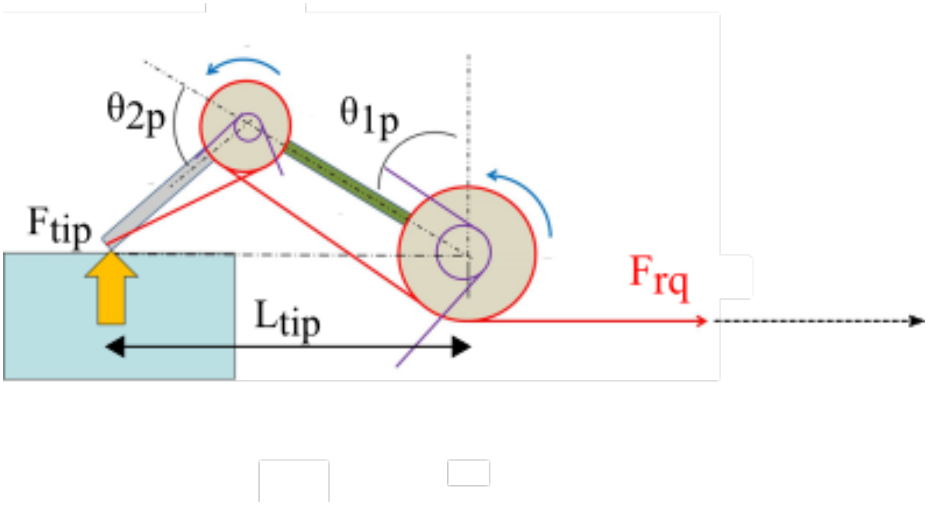

Figure 3-25: Pinching posture of the robot finger

$$0 = L_1 \cos\theta_{1p} + L_2 \cos(\theta_{1p} + \theta_{2p}) \tag{3.21}$$

$$L_{tip} = L_1 \sin\theta_{1p} + L_2 \sin(\theta_{1p} + \theta_{2p}) \tag{3.22}$$

$$F_{rq} = \frac{k_1(\theta_{1p} + \theta_{1,0})}{R_1} = \frac{k_2(\theta_{2p} + \theta_{2,0})}{R_2} \tag{3.23}$$

$$F_{out,p} = \frac{F_{tip} L_{tip}}{R_1} + F_{rq} \tag{3.24}$$

$$x_{max} = R_1\theta_{1,max} + R_2\theta_{2,max} \tag{3.25}$$

Table 3.3: Summarize of important values in pinching

Specification	Variable	Value
Cable tension required to reach pinching position	F_{rq}	1.2 N
Cable tension required to for 20 N pinching force	$F_{out,p}$	87.2 N
Moment arm at pinching position	L_{tip}	43 mm
Max cable length pulled for full finger retraction	x_{max}	19.4 mm

Cable-driven LRT design

Although the finger requires at least 87.2 N output force in pinching posture according to Table.3.3, designing a 20 N fingertip force for the stretched finger would ensure the fingertip force of more than 20 N for any object thickness. Therefore target output force of the LRT was set to 100 N. The target size of the LRT unit was to fit inside a human palm. The finger/LRT pair also needs to have a high compliance range wide enough for its full finger stroke. A 0.69 mm Kevlar rope with a maximum load of 60 kg was used as the cable because of its high strength and its low lateral stiffness which allowed the use of small sized pulleys.

From Eq.3.12 and 3.11, the change in reduction ratio can be written as follows

$$\frac{R_{HF}}{R_{HS}} = 2N_b\frac{D_g}{D_h} + 1 \tag{3.26}$$

D_g/D_h and N_b were chosen to get R_{HF}/R_{HS} of more than 10 times. Large D_g/D_h would result in a higher change of reduction ratio. However, an overly small D_h compared to the cable diameter will ruin the cable life. Therefore, the hub and pulleys diameter were chosen to be significantly larger than the cable diameter. A commercially available brass gear (S50B45B+0208) with hub diameter of 10 mm was then used. The gear has a pitch diameter D_g of 22.5 mm, so the ratio D_g/D_h was 2.25. A condition $N_b \geq 2$ was calculated from Eq.3.26. Therefore, the pulley sets were designed to have three pulleys each so that $N_b = 3$.

Another design criterion for our finger/LRT pair was that the finger should be able to retract compliantly in a collision. For the robot finger, minimum d_{sep} was calculated by using Eq. 3.17 and Eq. 3.25. Table 3.4 summarizes the minimum d_{sep} for full retraction of the finger. For this prototype with $N_b = 3$, the d_{sep} was chosen be more than 4 mm. The rack carrier preload was designed so that d_{sep} is configurable up to 7 mm.

The spring preload $k_s x_0$ was chosen to be 7.4 N using Eq.3.16 with $N_b = 3$ and $F_{rq} = 1.2N$ from the finger specification. A spring with $k_s = 0.442N/mm$ was chosen to have as low stiffness as possible to get high output force of the LRT. Also, the spring needed

Table 3.4: Minimum d_{sep} required for full retraction of the developed finger

N_b	required d_{sep}
1	9.7 mm
2	4.85 mm
3	3.23 mm

to have enough free length after preloaded for the total rack travel. This rack travel range has to be higher than d_{sep} but cannot be arbitrary large from the size constraint of a human palm. The maximum rack travel length was chosen to be 18.5 mm. The required input force from the motor was approximately 13 N, calculated with Eq.3.14, assuming $\eta_H = 0.7$ and $\eta_L = 0.9$. The maximum travel range of 18.5 mm was used in this design calculation.

A small DC geared motor (COPAL HG16-030-AB-00) was chosen and connected to a winch shaft using a 1:1 bevel gears pair. The winch diameter is 6 mm (about nine times larger than the cable diameter). The motor current was limited by a DC power supply Kikusui PMM25-1TR to 0.25 A (40% of the stall current) to get the required input force during stall without overheating. The motor rated speed could pull the cable by 97 mm/s, which is sufficient for the closing speed target of 0.5 s. In addition, the speed was adequate for the clutch to engage within 1 s, calculated from $2N_b d_{sep}/v_{in} = 0.43$ s with the worst case scenario when $d_{sep} = 7$ mm. For d_{sep} = 4 mm, the clutch transition time would be 0.25 s. Fig. 3-26 shows a 3D model and the prototype of finger/LRT pair. The overall specifications of the LRT are listed in Table 3.6.

The LRT prototype weighed approximately 156 g (transmission: 44 g, geared motor: 27 g, palm-sized frame: 85 g). The finger weighed approximately 38 g, and the finger base used to fasten the finger to the LRT unit weighed 36 g. The total weight of the finger/LRT assembly was 230 g. Note that the weights of the frame and finger were not optimized.

Table 3.5: Motor specification COPAL HG16-030-AB-00

Specification	Value
Rated torque	24.5 mNm
Rated speed	310 RPM
No load speed	390 RPM
Starting current	600 mA
Stall torque	Approx 100 mNm
Input voltage	12 V

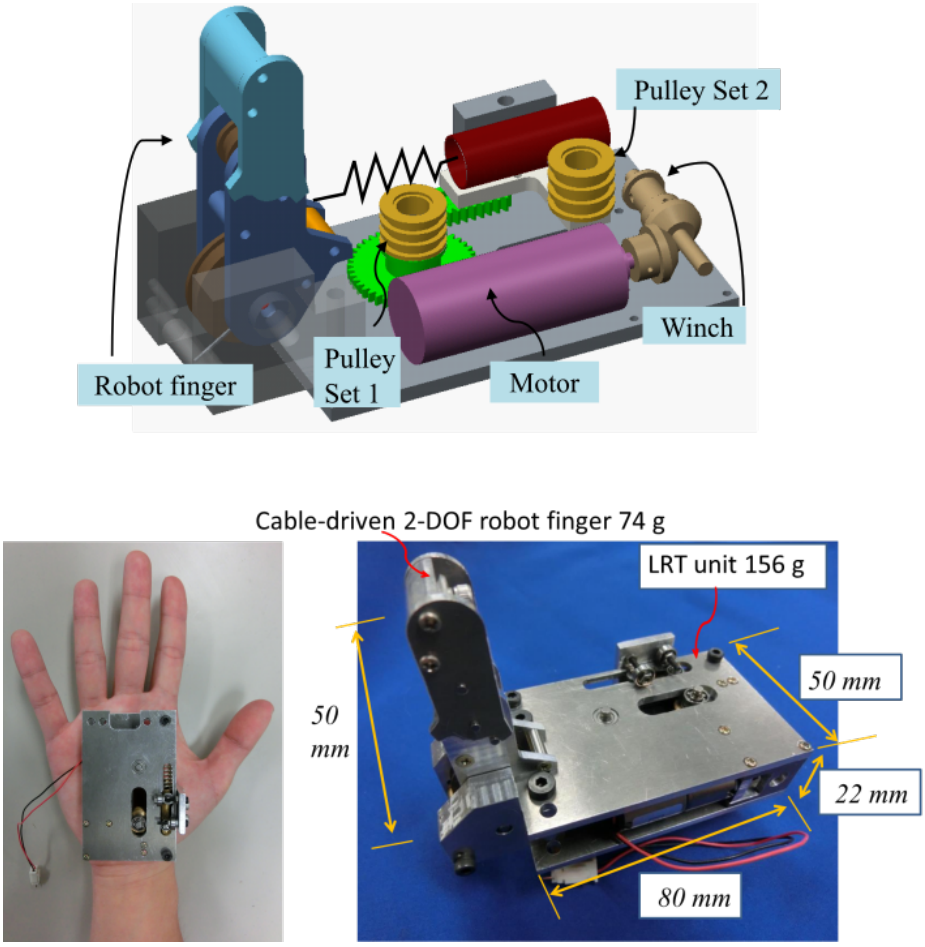

Figure 3-26: A prototype of the finger/LRT pair

Table 3.6: Parameters of the cable-driven LRT prototype

Specification	Variable	Value
Gear hub diameter	D_h	10 mm
Gear pitch diameter	D_g	22.5 mm
Gear and rack module	m	0.5 mm
Gear and rack pressure angle	α	20 deg
Pulley diameters	D_{p1}, D_{p2}	10 mm
Compression spring stiffness	k_s	0.442 N/mm
Preloaded spring force	$F_{s,0}$	7.4 N
Rack–gear separation distance	d_{sep}	$1-7$ mm
Maximum allowable rack travel length	max x	18.5 mm
Number of cable bindings	N_b	$1-3$
Input winch diameter	D_{in}	6 mm

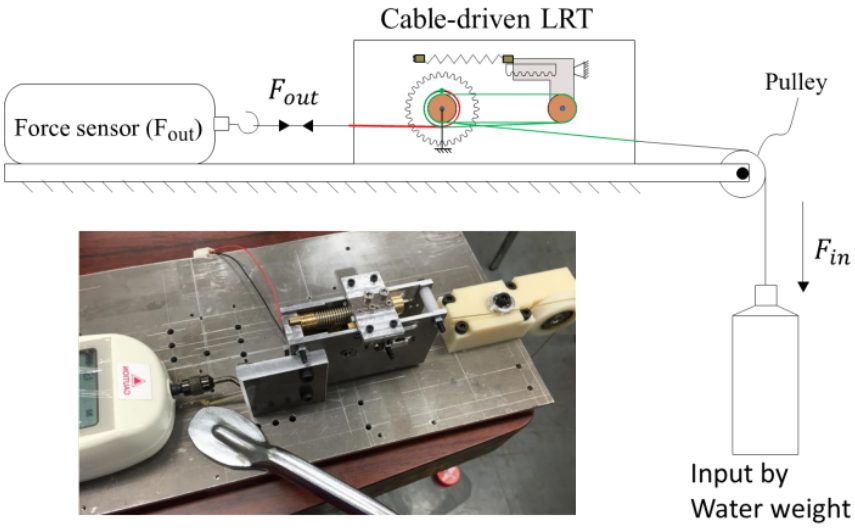

Figure 3-27: Static experiment setup of cable-driven LRT prototype

3.2.2 Experiments and results

Static test of the LRT unit

First, the performance of the LRT was measured statically without the finger. Water weights were used as the input F_{in}.The output cable tension F_{out} was measured by a force sensor. Figure 3-27 shows the experiment setup. In this experiment, the d_{sep} of the LRT was set to the maximum value of 7 mm. The experiment results and the theoretical values calculated from Eq. 3.13 and 3.14 are plotted together in Fig. 3-28. Although the actual design of the LRT unit used the maximum rack travel of 18.5 mm in the calculation of the spring force, as the force sensor was significantly stiff, the rack did not move much past the engagement point. Therefore, the spring force used in the calculation of the theoretical values was estimated from $F_s = k_s(d_{sep} + x_0)$ for all input forces in HF range. The assumption of η_L and η_H was the same as the values used in the LRT design. The graph shows that the mathematical model is accurate enough to be used in the design of the cable-driven LRT.

Because the number of cable loops N_b could be easily changed by rerouting the cable, all possible configurations of N_b were also tested. Figure 3-29 shows the experimental results. The values were averaged from three experiments for each case. The lines in this graph show the ideal cases whose η_L and η_H are both set to 1 (no friction loss). The ratio

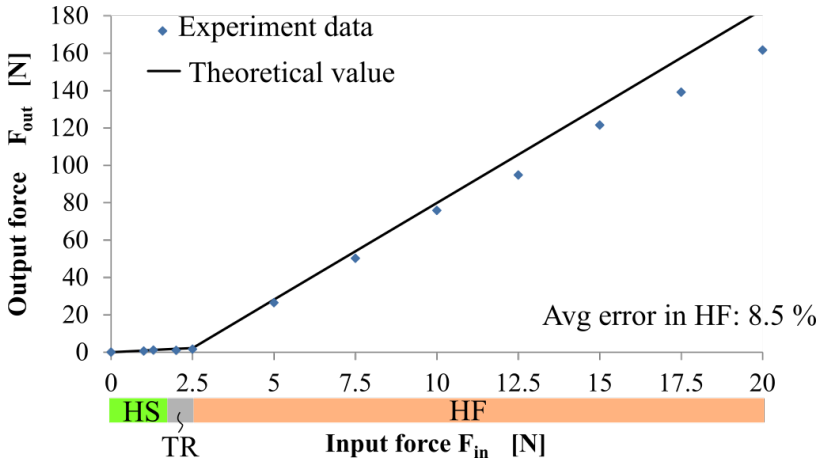

Figure 3-28: Static experiment results compared with the theoretical values

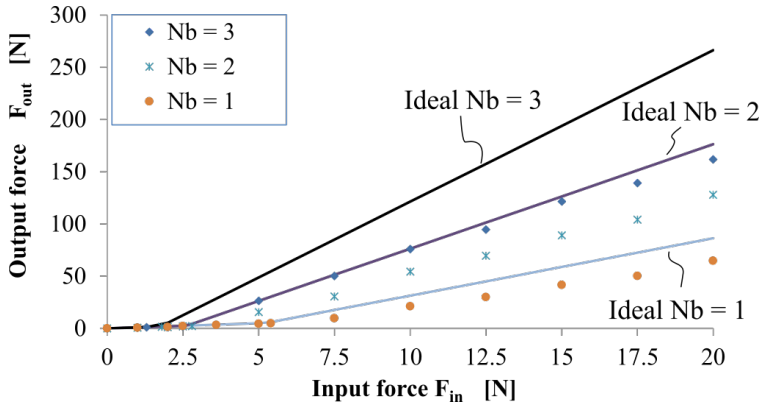

Figure 3-29: Static experiment results compared with lossless ideal cases

of F_{out} between the actual and ideal values is then defined as the transmission efficiency η. Table 3.7 summarizes average values of η calculated point by point for each case. It was found that η decreased after the mechanism changed from the HS phase to the HF phase. Higher N_b cases also resulted in less η. This can be explained by the increase in the frictional losses from the additional components such as pulleys, and rack-gear clutch in the transmission line. Fig. 3-30 shows the static test result on the purely HS case which the rack carrier was not allowed to move. The steeper slopes in HF phase than that of the HS case indicates that the LRT could change its reduction ratio by the clutch engagement. The higher the value of N_b, the steeper the slope in HF phase of the LRT. The input force required to engage the gear F_e was also lower for the higher N_b cases, as expected from Eq. 3.15.

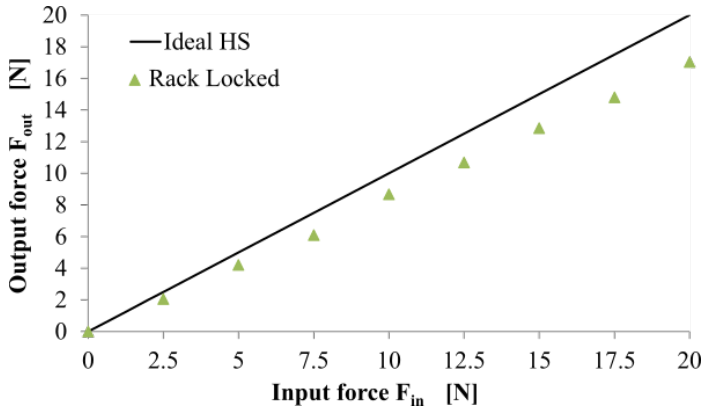

Figure 3-30: Static experiment results in purely HS phase (rack locked)

The output force magnification ratio (HF/HS) was calculated by comparing F_{out} between the HF and purely HS case at $F_{in} = 20$ N. Table 3.8 lists the force magnification ratios and the changes in the reduction ratio of the LRT prototype.

Table 3.7: Static transmission efficiency of cable-driven LRT

η	$N_b = 1$	$N_b = 2$	$N_b = 3$
HS	0.78	0.79	0.74
HF	0.69	0.65	0.60

Table 3.8: Force magnification ratio and reduction change of the cable-driven LRT

	$N_b = 1$	$N_b = 2$	$N_b = 3$
$F_{out,HF}/F_{out,HS}$	3.9	7.8	10.2
R_{HF}/R_{HS}	5.5	10	14.5

Two-phase pinching experiment

In this experiment, the robot finger was connected to the output of LRT unit to verify the two-phase pinching. The motor was driven to stall with the current limited to 0.25 A. A force sensor AIKOH-RX-series (sampling rate of 20 Hz) was used to measure the pinching fingertip force. Fig. 3-31 shows the force measurement result with the LRT parameters configured as designed ($N_b = 3, d_{sep} = 4$). The force data were collected starting from the contact between the finger and the force sensor. Time 0 s is just right after the contact. The lack of an impact spike at the moment of contact was not captured because of the slow

sampling rate (20 Hz). Here, delay A depicts the rack travel time delay from contact to the rack-gear engagement. Delay B refers to time delay originated from the cable elongation, that is the time used for the output force to reach its peak after the LRT changed into HF phase. The dashed line represents the ideal case when the cable and all mechanical parts are infinitely stiff. From the result, the fingertip force was around 25 N which is sufficient for the design target of 20 N. The finger joint speed during HS phase was calculated from video recordings. The average joint speed in HS was 372 deg/s. This is equivalent to about 0.25 s closing time, which is faster than the target 0.5 s.

Several configurations of N_b and d_{sep} were also investigated. Fig 3-32 shows the fingertip measurements. The values were averaged from three experiments for each case. The output force F_{tip} decreased as d_{sep} increased. This relationship can be explained by Eq. 3.14. A smaller value of d_{sep} means that the rack can reach the engaging point with a shorter travel distance. This means a lower spring force F_s, thereby resulting in a slightly higher F_{tip}. In the case of $N_b = 3$, there was not much difference in the output force for different values of d_{sep}, when compared to the other two N_b cases. This is because the spring force and sliding friction become less significant compared to the generated pulling force at Pulley Set 2 for higher N_b cases. Table 3.9 lists the delays from the experiment results together with the F_{tip} at static equilibrium. The result shows that a higher N_b tends to have both longer rack travel time (A) and elongation delay (B). This is because higher N_b results in higher G_H of the LRT and thus affect both delays A and B as discussed in chapter 2. Particularly, the higher G_H in this cable-driven LRT means a longer total length of the cable and also the slower output speed, given the same motor speed. Higher d_{sep} also resulted in higher values in both delays, but with less influence than N_b. Delay A can be changed by designing N_b and d_{sep}. Delay B is inevitable for cable-driven systems. However stiffer cable can help reduce the amount of time used.

It was also experimentally confirmed that the finger could return to its initial position using the spring force when the motor unwinded. The return movement was slow at first while the rack was still in engagement with the gear. After the rack disengaged, the finger quickly returned to its initial position. The cable tension was kept positive by limiting the motor unwinding rotations.

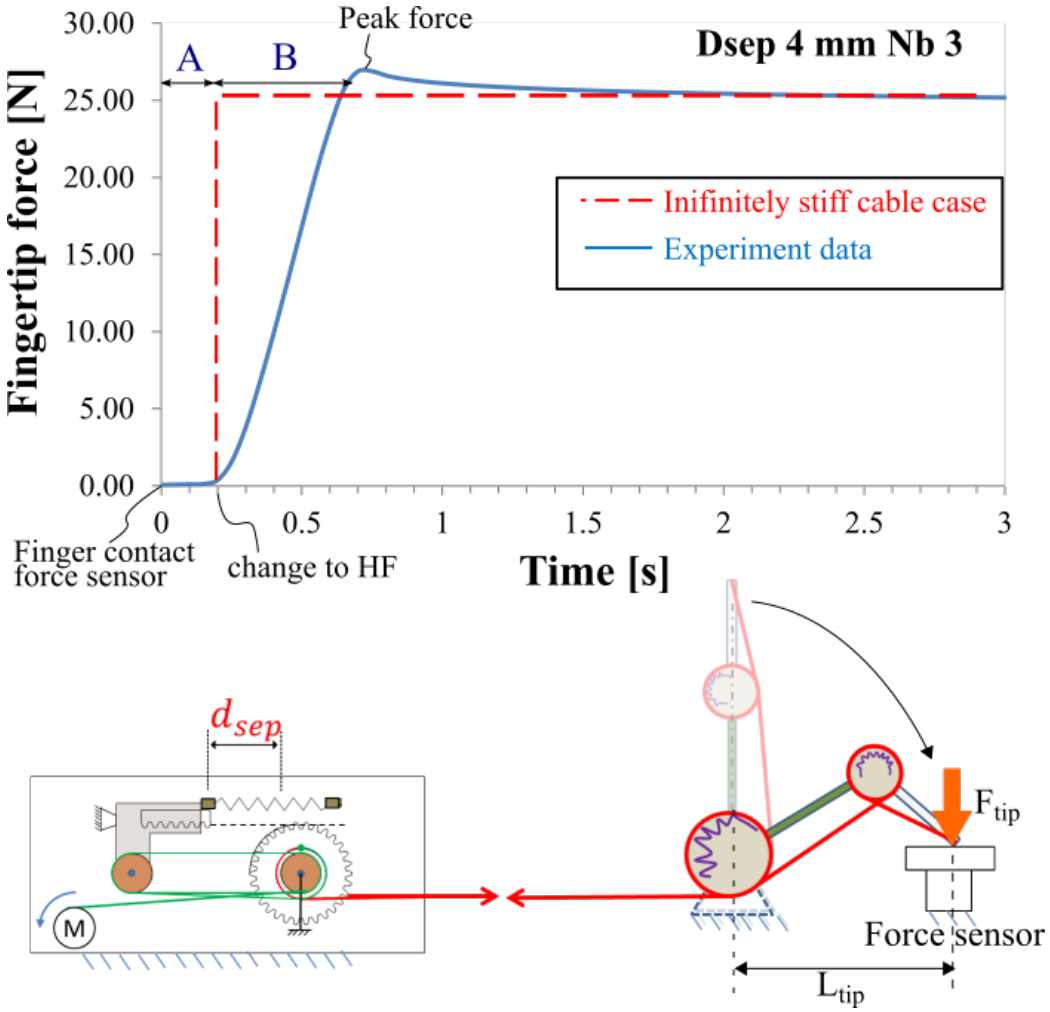

Figure 3-31: Force measurement of two-phase pinching experiment
(With the designed value $d_{sep} = 4$ mm, and $N_b = 3$)

Table 3.9: List of delays from two-phase pinching experiment results

N_b	d_{sep}	Delay A [s]	Delay B [s]	Total delay A+B [s]	F_{tip} [N]
1	1	0.05	0.15	0.2	13.17
1	4	0.05	0.15	0.2	11.10
1	7	0.05	0.15	0.2	10.26
2	1	0.10	0.20	0.30	24.70
2	4	0.10	0.25	0.35	20.38
2	7	0.15	0.35	0.50	18.16
3	1	0.15	0.50	0.65	24.59
3	4	0.25	0.45	0.70	24.58
3	7	0.40	0.45	0.85	23.83

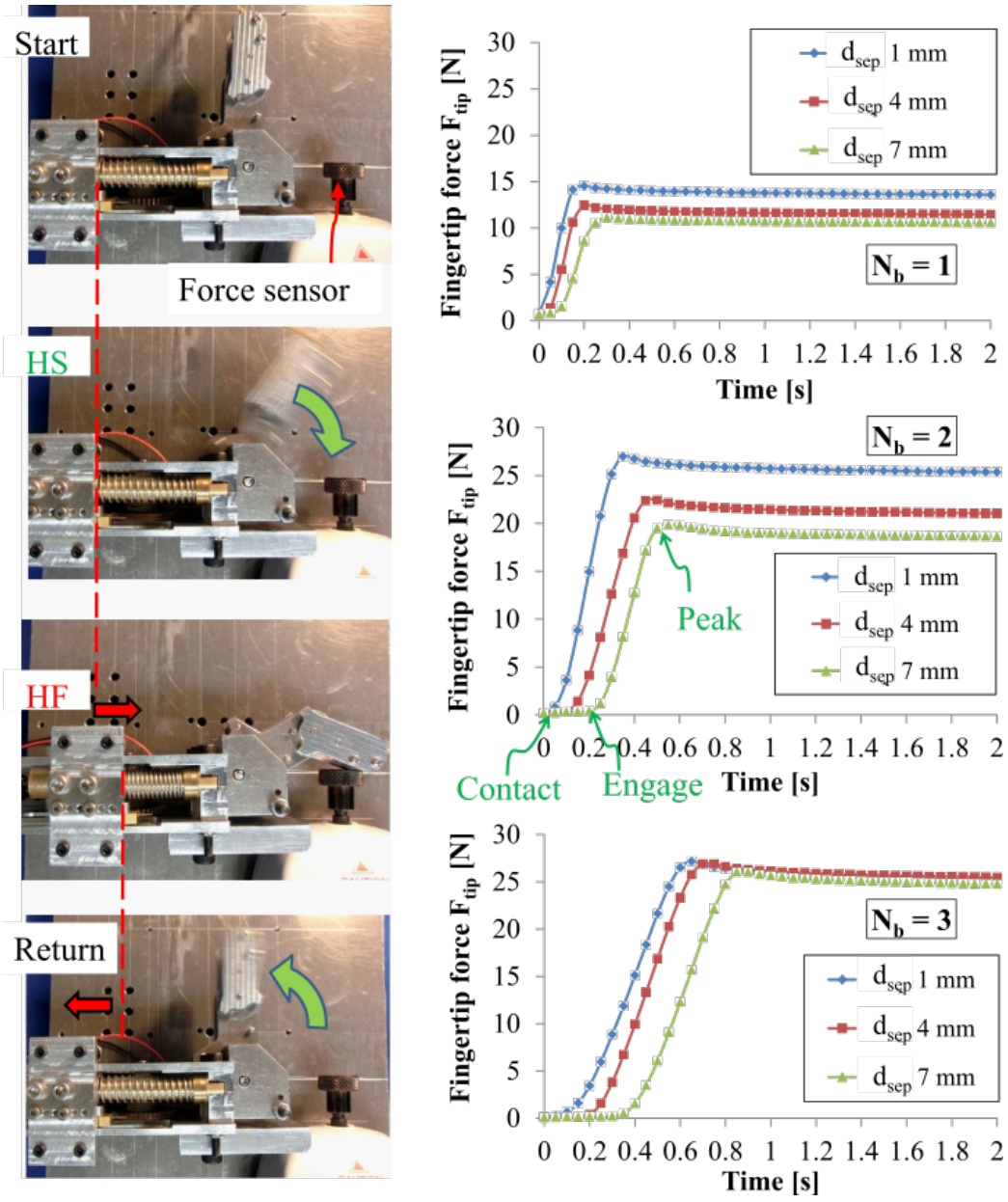

Figure 3-32: Force measurement of two-phase pinching with various N_b and d_{sep}

Compliance shock response in the HS phase

For the chosen configuration, a drop test was conducted to verify the compliant behavior of the finger/LRT pair. A 500 g (approximately 5 N) metal block was used as the drop weight. Because the finger/LRT pair could exert a fingertip force of up to 24.6 N in the HF phase, the metal block would not be able to fully retract if the LRT had changed to the HF phase during the collision. Figure 3-33 shows the snapshots taken during the experiment. The center point of the block is marked with a red circle to help clarify its position. As shown, the finger was struck during its HS phase. The finger then exhibited a compliant behavior with the phase transition. The finger was able to be fully retracted and allowed the metal block to move past the grasping range. After that, the finger flexed back to its HS phase. The graph shows the rack travel during the experiment. The motor was turned on at $t = 0$ s. A indicates the collision point between the metal block and the robot finger. B indicates the fast rack movement caused by the finger retraction due to the impact. At the moment the block slipped out of the finger range, the compression spring in the LRT released its stored energy from the impact. This pushed the rack back toward point C, and at the same time, quickly flexed the finger. Once the finger reached its maximum flex limit, the LRT changed into HF phase. Because the metal block was not stopped at the moment of impact, only a part of its momentum was transferred to the finger/LRT pair. In addition, the compression spring also helps absorb the collision. This reduced much of the damage done to both the robot finger and metal block, which served as an analog for a human hand. Full retraction of the robot finger also confirmed that the proposed LRT design method could ensure a full range of compliance for the given robot finger.

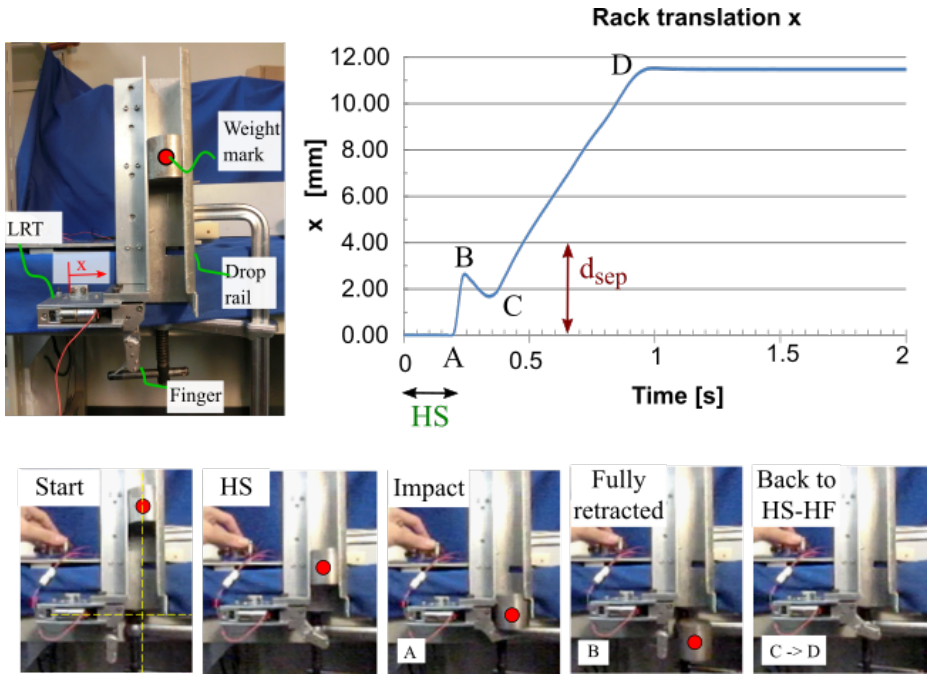

Figure 3-33: Snapshots of the drop test

(500 g weight with speed around 1.5 m/s on impact)

Effects of the spring parameters

In this experiment, the effects of the spring stiffness k_s and the preloaded spring force $F_{s,0}$ were investigated. Figure 3-34 shows the experimental results with four cases: I, II, III and IV. In cases I–III, k_s was fixed but $F_{s,0}$ were varied with three different values. On the other hand, cases I and IV shared the same $F_{s,0}$ but had a different k_s. These values were chosen according to the physical limit of the compression spring and the accommodating size of the LRT. The graph on the right-hand side of the figure shows a magnified view of the end parts of the main graph on the left side. The two-phase pinching experiment was performed three times for each case, and the average values were taken to plot the results.

The right inner graph shows that the fingertip forces as they reached their asymptotic values. By comparing the four cases, it was found that F_{tip} in case I>II>III and I>IV. That is, the cases with higher $F_{s,0}$ and k_s produced a lower output fingertip forces. This is because the total spring force F_s acted on the rack carrier in a counterproductive manner, as shown in Eq.3.14. Therefore, k_s and $F_{s,0}$ should be as small as possible in combination with the condition in Eq.3.15 to ensure that the rack does not move prematurely before the

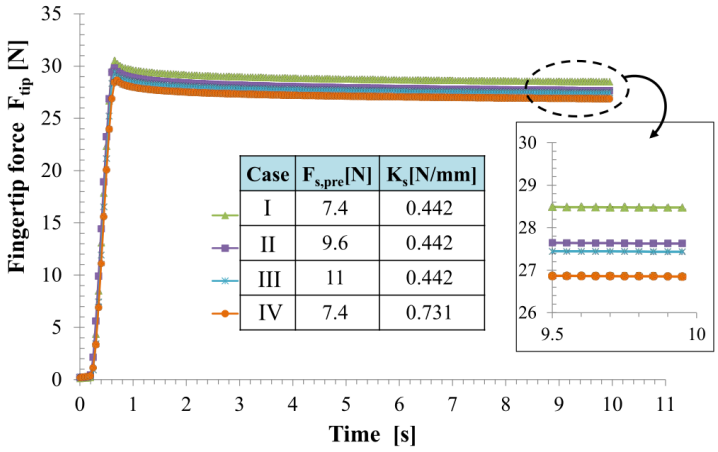

Figure 3-34: Effects of spring parameters $F_{s,0}$ and k_s

finger reaches the pinching position.

Because the overall effects of k_s and $F_{s,0}$ on the mechanism performance were not as apparent compared to other main parameters such as N_b and d_{sep}, optimizing them may not be significant. Choosing k_s and $F_{s,0}$ in comply with Eq. 3.15 should be sufficient as a design guideline.

3.2.3 Discussion on limitation of cable loop

According to the proposed concept of the cable-driven LRT, a larger number of N_b would increase the reduction ratio in HF phase of the LRT. However, there are some limitations that should be considered. First, more cable loops require more pairs of pulleys and thus thicken the LRT design. The developed LRT prototype was designed to fit in a human palm, so the maximum limit of $N_b = 3$ was chosen. Even if there is no limitation of space, more pulleys still induce additional friction loss along the cable line. Fig.3-35 shows a single pair of pulley from pulley sets 1 and 2 of LRT. The cable tension force decreases at every pulley turn. Given the transmission efficiency of the cable per turn to be η_c, the final output tension to the gear hub would be $\eta_c^{2N_b} F_{in}$. For the low reduction path G_L, the total transmission efficiency η_L can be determined by

$$\eta_L = \eta_g \eta_c^{2N_b} \tag{3.27}$$

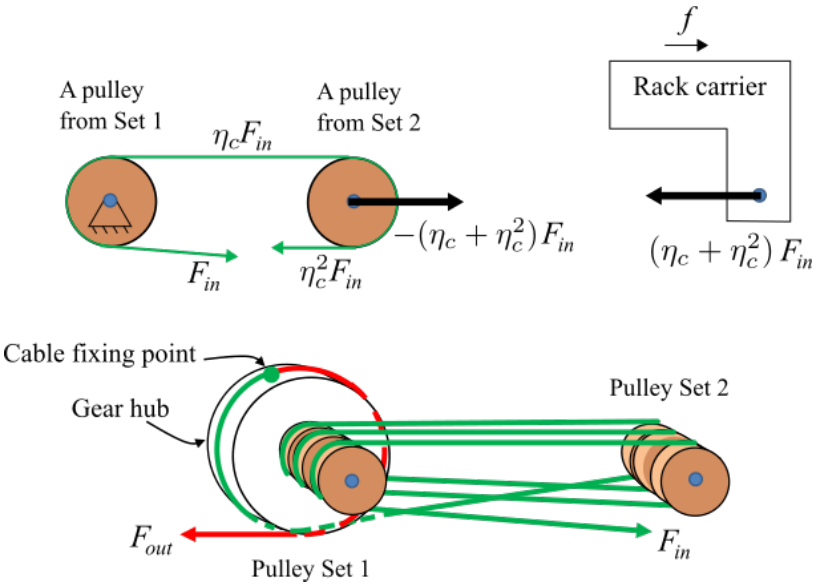

Figure 3-35: Cable friction and its effects

where η_g represents the transmission efficiency of the gear and gear hub.

For the high reduction path, G_H comes from the pulling force at the movable pulleys $\eta_c F_{in} + \eta_c^2 F_{in} + \ldots$ and the engagement of rack-gear clutch. Therefore, η_H can be determined by

$$\eta_H = \frac{\eta_g \eta_r}{2N_b} \sum_{i=1}^{2N_b} \eta_c^i \tag{3.28}$$

where i belongs to positive integers. η_r represents the transmission efficiency of the rack and gear engagement, which is lower than 1 because of sliding friction f and loss at the gear teeth. The values of η_c = 0.95, η_r = 0.9 and η_r = 0.85 (the gear used a sliding bearing), were found found by fitting the theoretical value calculated from Eq. 3.13 and 3.14 to the static experiment data of the prototype. Fig. 3-36 plots the experiment results with the calculated values using the extracted η_c, η_r, and η_r.

Eq. 3.27 and 3.28 both show that η_L and η_H increase as N_b increases. Although the LRT can be designed with a very high reduction ratio by increasing the cable loops, the expected output force can not be increased infinitely because the transmission efficiency drops. Fig. 3-37 shows a simulation result of the output force in HF phase versus N_b. The

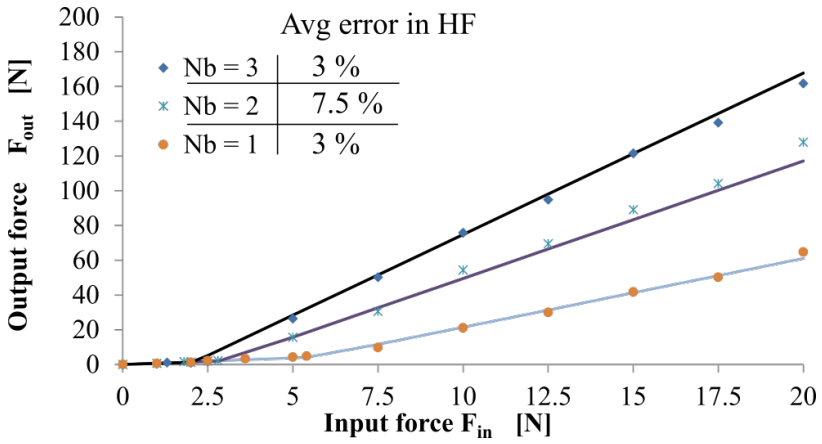

Figure 3-36: Static experiment data fit using accurate friction model

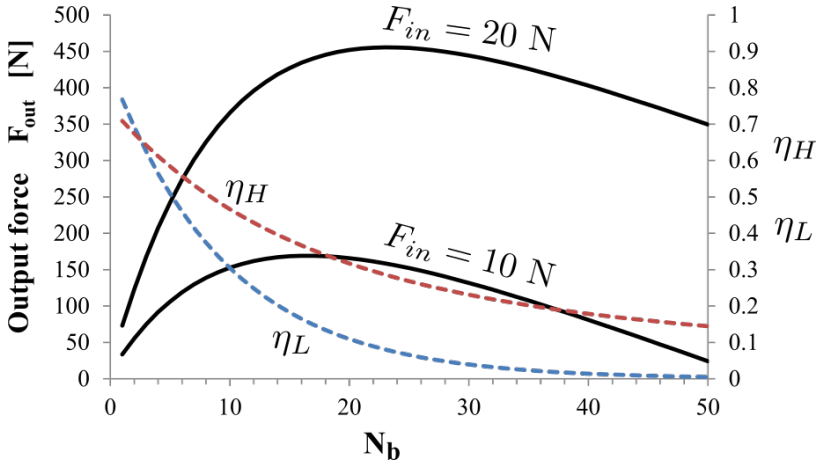

Figure 3-37: Output force and N_b simulation
η_c = 0.95, η_r = 0.9 and η_g = 0.85

clutch switching threshold F_e was scaled to keep the same load threshold for every N_b case. The output force was calculated by keeping F_{in} constant (10 N and 20 N). The dashed lines show the calculated values of η_H and η_L. From the simulation, the output force peaked at $N_b = 23$ with input force of 20 N and $N_b = 16$ with input force of 10 N. Note that a larger N_b also contributes to a larger G_H which increase delay A and B as discussed in chapter 2. The simulation can be used to optimize the design of the cable-driven LRT.

3.2.4 Performance evaluation

The performance of the proposed LRT can be evaluated by comparing its pinching performance to an underactuated finger of existing cable-driven prosthetic hand [58] shown

in Fig. 3-38. The reference finger uses a 12V DC motor (Faulhaber 1724 SR12) with a planetary gearhead (Faulhaber 16/7 43:1). Table. 3.10 summarizes the comparison. The thumb finger produces the maximum fingertip force of 20 N with a supply current of 1 A at a fully flexed position against the palm. The closing time of 0.4 s indicates the joint speed of 246 deg/s. In contrast, the prototype finger/LRT could achieve 24.6 N fingertip force in HF phase with less current. The joint speed in HS phase was 372 deg/s or 0.25 s closing time, which is 50% higher than the reference finger. The weight of the developed LRT without frame is slightly heavier than that of the reference finger's actuation unit.

The developed finger/LRT could provide both a faster closing speed and a significantly stronger fingertip force for simple grasp-and-hold applications. Additionally, the developed finger/LRT also exhibited satisfactory compliant behavior during its high speed motion. This high compliance can help reduce potential damage from a collision in the grasping plane.

The change in the reduction ratio of the developed LRT R_{HF}/R_{HS} was 14.5 times for the designed configuration. The large change in reduction ratio produced high output force in HF phase. The force magnification ratio $M_f = F_{out(HF)}/F_{out(HS)}$ (calculated at the same input force) divided by the total change time (delay A+B) can also be used to evaluate the LRT performance. The force magnification rate MR_f is defined by

$$MR_f = \frac{F_{out(HF)}/F_{out(HS)}}{A+B} = \frac{M_f}{A+B} \tag{3.29}$$

Table. 3.11 compares the value with existing cable-driven load-sensitive CVTs introduced in Chapter 1. The comparison shows that the proposed cable-driven LRT could magnify the output force at a significantly higher rate than some CVTs for robot joints.

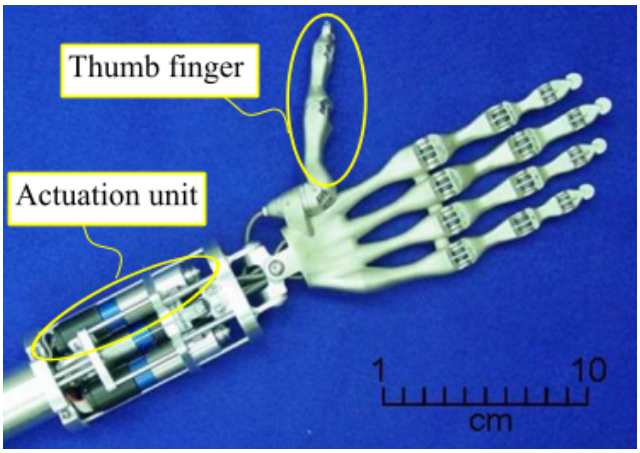

Figure 3-38: Cable-driven underactuated prosthetic hand: VU hand [58]

Table 3.10: Comparison with an existing cable-driven robot finger [58]

Performance and specification	Thumb finger of VU hand[58]	Finger/LRT
Maximum fingertip force	20 N	24.6 N
Motor current	1 A	0.25 A
Joint speed	246 deg/s	372 deg/s
Grasp speed	0.4 s	0.25 s
Weight of actuation unit (without frame)	60 g	71 g

Table 3.11: Comparison with existing cable-driven load-sensitive CVT
* Change in reduction ratio is used instead of the non-reported force ratio

Performance and specification	Twisting CVT [35]	Drum CVT[33]	developed LRT
Force magnification ratio HF/HS M_f	4.61	3*	10.2
Total change time	5 s	1.2 s	0.7 s
Force magnification rate MR_f	0.9	2.5*	14.6
Weight (without frame)	29.9 g	No report	71 g

3.3 Conclusion on cable-driven LRT

This chapter presented a cable-driven transmission using the concept of LRT. First, a novel split pulley clutch were introduced and shown that it could change the reduction ratio load-sensitively. However, the issues of cable damage and slippage caused by the pulley grippers limit its use to low output force applications. An improved design of cable-LRT using a rack-tilting mechanism was then introduced to solve the previous issues of the split pulley type. A 2-DOF underactuated robot finger and an LRT prototype unit were developed to achieve a design target of 20 N fingertip force in pinching. The target closing speed of less than 0.5 s, high force magnification rate and high compliance during high-speed motion were addressed. Static experiments were done the verify the transmission concept and mathematical model used in the design. The prototype finger/LRT pair was experimentally verified that it could provide the two-phase pinching operation. The LRT prototype was able to change the reduction ratio by 14.5 times in 0.25 s, which is faster than 1 s from the research objective. Performance evaluation showed that the developed finger/LRT pair could provide faster speed and stronger fingertip force when compared to a reference robot finger with a fixed reduction actuator. The output force of the LRT could be magnified by about 10 times in 0.7 s. Although space constraint of a human palm limited N_b of the developed prototype, a higher output force with higher N_b is possible if the LRT unit can be placed at a remote location such as in the forearm. Design limitations of N_b and friction effects were also discussed in this chapter. Also, the force magnification rate was shown to be higher than some cable-driven CVTs. It has to be noted that the magnification rate can be increased by minimizing d_{sep} if the compliance is not required, which also results in a more compact LRT. Another way to reduce the requirement on d_{sep} is by introducing a damper to prevent abrupt movement of the rack carrier unit during the impact. Some discussion and experiments on the damper idea can be found in Appendix of this thesis.

In conclusion, the developed cable-driven LRT can fulfill the objective in load-sensitively and rapidly switch the reduction ratio to produce two-phase pinching operation. The compliant behavior during fast finger motion was also experimentally confirmed. Furthermore, in contrast to CVTs whose stiffness continuously increases during impacts. The relatively

constant low stiffness of LRT has the potential to improve the impact tolerance of robot joints. Moreover, as with many cable drive actuation, a single cable-driven LRT unit can also be used to drive multiple fingers through underactuation.

Chapter 4

Gear-driven LRT

From the developed cable-driven LRT, there was a limitation of the rack-tilting mechanism. That is the need of a lengthy accommodation space, especially when a long HF stroke is required. This might not be a problem for cable-driven hand, which has a long housing space in the forearm. However, it may limit the use of LRT in a more limited space such as elbow joints. This chapter will introduce a novel clutch mechanism that can solve this problem and a gear-driven LRT using the developed clutch.

4.1 Gear-clutch mechanism

4.1.1 Basic concept and Mathematical model

Fig.4-1 compares the linear rack-clutch with circular gear clutch motion. Considering If the output link is rotated by one round. The rack length has to be at $L = \pi d$, where d is the pitch diameter of the output gear. The accommodation length of the rack systems has to be at least $2L$ as the rack protrudes in the front. For applications that need long HF stroke such as robot arms, the large size of the rack mechanism and its protrusion may not fit into the available space. In contrast, the gear-clutch require significantly less space, given the same HF stroke of one round. Therefore more compact design of LRT for elbow joint is possible using the proposed gear-clutch.

Fig. 4-2 shows the mechanism concept. The basic concept is similar to the rack-tilting

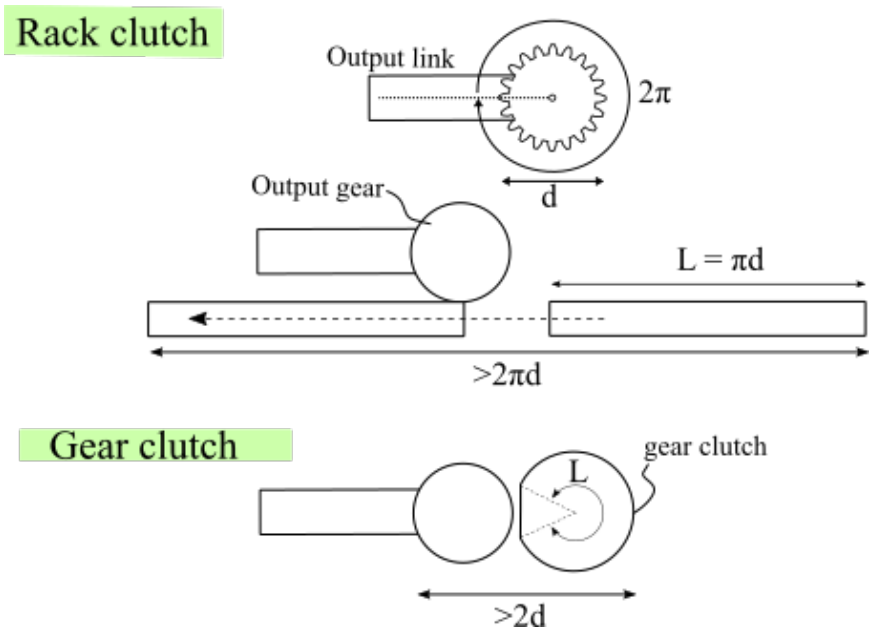

Figure 4-1: Comparison of accommodation space between rack clutch and gear clutch

mechanism. That is it utilizes the difference in the direction of reaction forces during jamming and meshing to allow a jam-free and stable engagement. Gear G1 is connected to the output link and driven by a low reduction input responsible for the HS phase. G2 is a gear that has a portion of its teeth cut off. G2 acts as an idler gear and is used to transmit the torque from a high reduction input connected to G1. For LRT application, HF phase will be achieved by driving G2 counter-clockwise to engage G3. To ensure a jam-free engagement, G2 must be allowed to move in tangent to the line connecting G1 and G2. Any radial movement towards G1 should not be allowed. The most straightforward method would be having a stiff link connects G1 and G2. The center distance between G1 and G2 is kept constant by the link. Fig. 4-2 shows this simple configuration of the gear-clutch mechanism. The link can be tilted around G1 axis and will be called “Tiltable link" in this study. The angle θ refers to the angle between the G1-G2 and G2-G3 lines and will be used as an important design parameter of the gear-clutch mechanism.

The proposed gear-clutch mechanism is statically analyzed separately for cases of meshing and jamming situations, respectively.

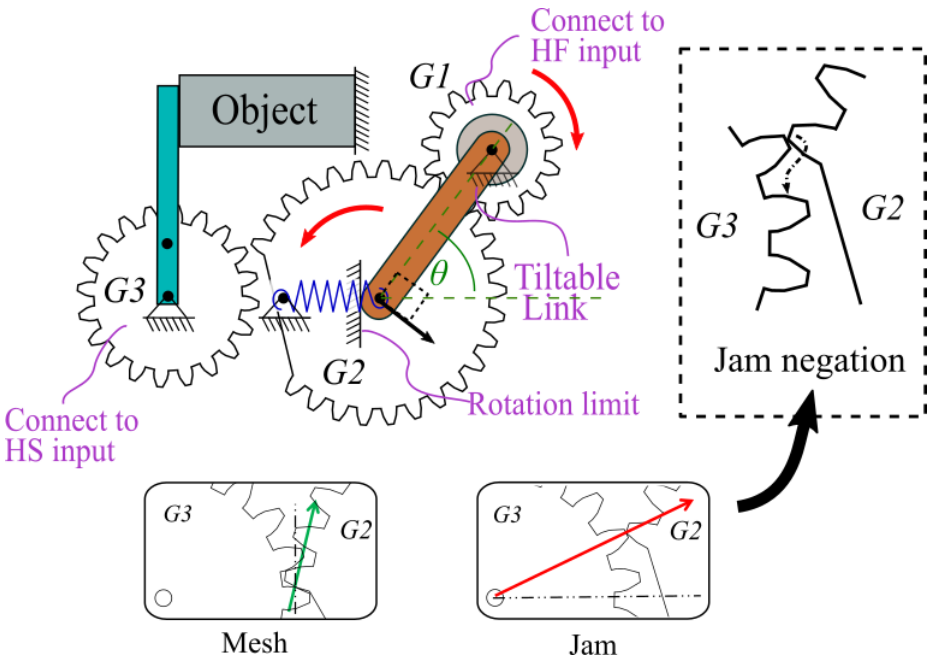

Figure 4-2: Concept of the gear-clutch mechanism

Stable meshing condition

In the case of normal engagement or meshing, the gears transfer the input torque τ_{in} to the output side by contacts between gear teeth. For involute teeth profile [49, 62], the direction of the normal force acting on the gear teeth can be determined from the pressure angle α of the gears. Fig. 4-3 shows the free body diagram of each gear and the tiltable link in the mechanism for meshing case. The force naming convention F_{12} indicates the force acting on gear G1 by gear G2. F_{21}, F_{23} and F_{32} all follow the same naming convention. F_{lt} and F_{lr} are the tangential and radial component of the force acting on the link by G2, respectively. For the dimensions, r_1, r_2 and r_3 are the pitch radius of each gears. Friction forces are neglected to simplify the model. Note that for clarity, some forces such as reaction forces at the fixed pivot joints are not shown in Fig. 4-3. Only the forces related to the analysis are shown.

In static equilibrium, assuming frictionless contact:

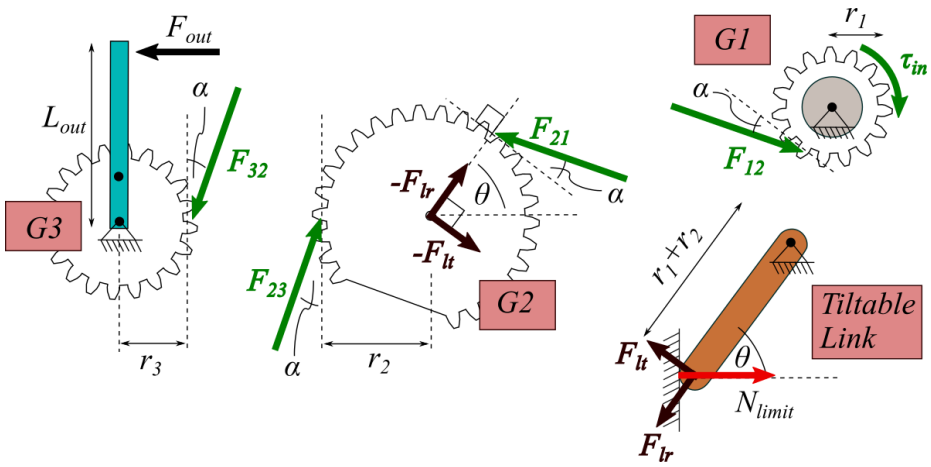

Figure 4-3: Free body diagram of gear meshing in static equilibrium

$$F_{lt} = F_{21}\cos\alpha + F_{23}sin(\frac{\pi}{2} - \theta - \alpha) \tag{4.1}$$

$$F_{21} = F_{23} \tag{4.2}$$

$$\tau_{in} = F_{21} r_1 \cos\alpha \tag{4.3}$$

$$F_{lt} = \frac{\tau_{in}(\cos\alpha + \cos(\theta + \alpha))}{r_1 \cos\alpha} \tag{4.4}$$

To maintain a constant center distance between G2 and G3 in normal meshing position, F_{lt} has to create a clockwise moment on the link, pushing it stably against the rotation limit. Therefore, in stable meshing, when $\tau_{in} > 0$ and $\theta > 0$; The condition for the clockwise moment $F_{lt} \geq 0$ combined with Eq. 4.4 results in

$$\cos(\theta + \alpha) \geq -\cos\alpha \tag{4.5}$$

which, after solving yields,

$$0 < \theta \leq \pi - 2\alpha \tag{4.6}$$

Eq. 4.6 indicates that the angle θ of the tiltable link must be within a certain range. θ

outside of this range will reverse F_{lt} direction and cause the G2 to move away from the meshing position, becoming incapable of transmitting torque statically. Moreover, at the singular point of the link mechanism ($\theta = 0$), the link always tilts for any non-zero F_{lt}, moving G2 away from G3. Such situation is considered an unstable meshing and therefore is excluded from the allowable θ range.

Jam-free condition

Unlike the previous analysis on the stable meshing condition which only the pressure angle α plays a big part in determining the usable values of θ, force analysis in the jamming situation requires a closer look into physical dimension of the gears. Fig. 4-4 shows the only possible jamming point for an involute G2-G3 gear pair with module m. The dashed line represents pitch circles of each gear. The outside radius of an involute gear is equal to the radius of its pitch circle plus its module size. The jamming point is then the intersection between the outmost circle of G2 and G3. In this study, G2 is driven in counter-clockwise direction for $\tau_{in} > 0$. Therefore, only the upper intersection point is of concern. For the widely used involute gears, the jamming angle β can be calculated by

$$\beta = \cos^{-1}\left(\frac{r_3(r_3+m)+r_2(r_3-m)}{(r_3+m)(r_2+r_3)}\right) \tag{4.7}$$

where m is the module of the gear teeth. r_2 and r_3 is the pitch radius of G2 and G3, respectively.

Fig. 4-5 shows the free body diagram of the gear-clutch mechanism during jamming. Please note that for clarity, some forces such as reaction forces at the fixed pivot joints are not shown. The reaction force pair F_{23}, F_{32} point radially to the center of G3 and act through the jamming point.

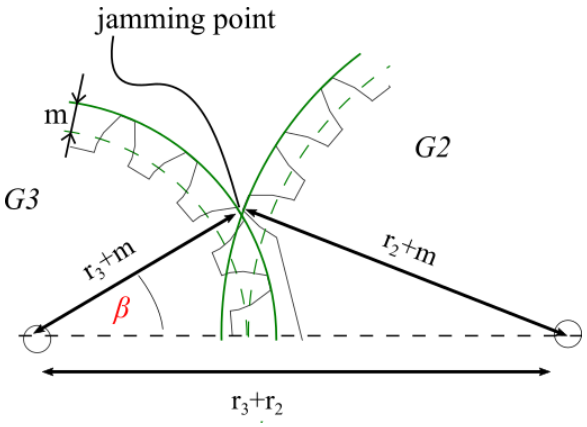

Figure 4-4: Jamming point and jamming angle β

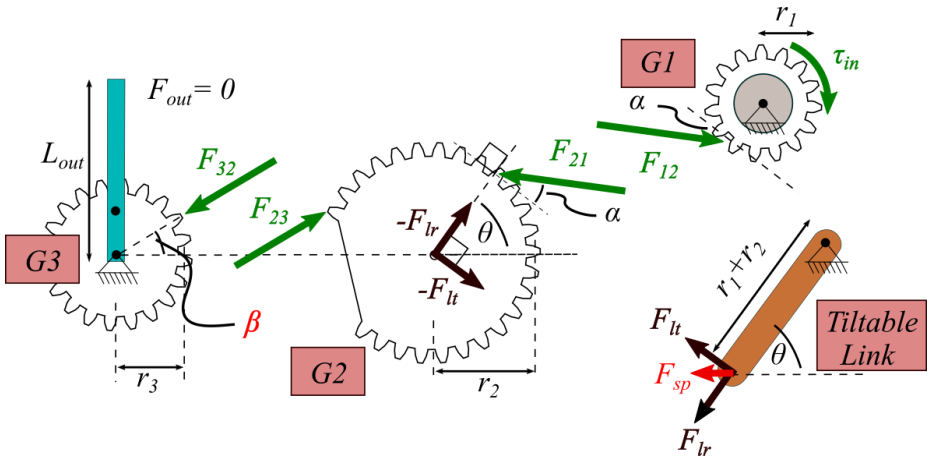

Figure 4-5: Free body diagram of gear jamming in static equilibrium

$$F_{lt} = F_{21}\cos\alpha - F_{23}\sin(\theta-\beta) \tag{4.8}$$

$$F_{21}r_2\cos\alpha = F_{23}(r_2+r_3)\sin\beta \tag{4.9}$$

$$\tau_{in} = F_{21}r_1\cos\alpha \tag{4.10}$$

$$F_{lt} = \tau_{in}\left(\frac{1}{r_1} - \frac{r_2\sin(\theta-\beta)}{r_1(r_2+r_3)\sin\beta}\right) \tag{4.11}$$

To allow G2 to slip pass the jammed tip as shown back in Fig. 4-2, F_{lt} must provide a counter-clockwise moment to the tiltable link against the preloaded spring force F_{sp}. When $\tau_{in} > 0$, $\theta > 0$, F_{lt} must obey the following condition in order to successfully negate the jamming.

$$F_{lt} \quad < \quad -F_{sp} \sin\theta \tag{4.12}$$

combining with Eq. 4.11 yields

$$\tau_{in} \left(\frac{1}{r_1} - \frac{r_2 \sin(\theta - \beta)}{r_1 (r_2 + r_3) \sin\beta} \right) \quad < \quad -F_{sp} \sin\theta \tag{4.13}$$

To simplify the problem, assume that the spring is sufficiently weak, $F_{sp} << F_{lt}$, which can be achieved especially with high reduction input at G1. The condition for jam-free engagement is then

$$(r_2 + r_3) \sin\beta \quad < \quad r_2 \sin(\theta - \beta) \tag{4.14}$$

To solve for θ from Eq. 4.14, a graphical representation in Fig. 4-6 is used. The problem turns into solving for $\theta_1 < \theta - \beta < \theta_2$. The result is the condition of θ for the desired jam-free engagement.

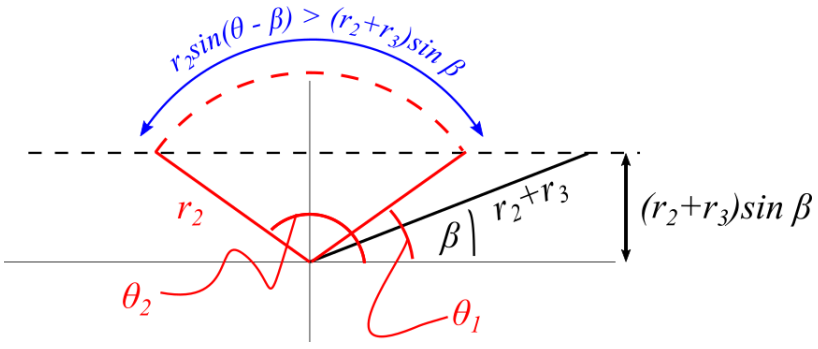

Figure 4-6: Graphical representation of Eq.4.14

$$\theta_1 = \frac{\pi}{2} - \cos^{-1}\left(\frac{(r_2 + r_3)\sin\beta}{r_2}\right) \tag{4.15}$$

$$\theta_2 = \frac{\pi}{2} + \cos^{-1}\left(\frac{(r_2 + r_3)\sin\beta}{r_2}\right) \tag{4.16}$$

$$\theta_1 + \beta < \theta < \theta_2 + \beta \tag{4.17}$$

To design a usable gear-clutch mechanism, the link angle θ must satisfy both the jam-free condition and the stable meshing condition. Note that both conditions can be derived from physical parameters of the gears. The workable range of θ is then the intersection of both conditions. Fig. 4-7 shows the working range of θ that can be used as a design guideline of the proposed jam-free gear-clutch.

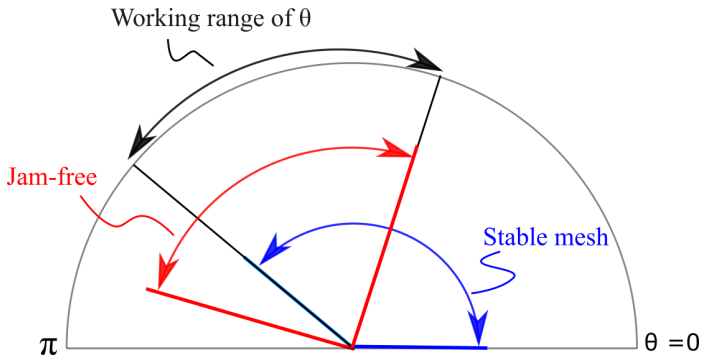

Figure 4-7: Working range of θ for the gear-clutch mechanism

4.1.2 Model validation and discussion

A test model for the gear-clutch mechanism was made and used to verify the developed mathematical model of the jam-free and stable mesh conditions. Fig. 4-8 and Table.4.1 show the experiment setup of the test model and its specification, respectively. The three gears and the tiltable link were positioned as shown. Input torque τ_{in} was generated by the cable wound around G1 hub. The rotation axis of G2 was fixed on the link and was pulled by a weak spring placed below G2 and G3. The output link was connected to G3. The

experiment link angle θ was limited by the practical design and manufacturing limit. That is $\theta > 144$ deg was not possible to test because G1 would hit G3. Secondly, the 12 deg per step was the finest limit because the smaller spacing between the holes would not be strong enough to hold the G1 axis during the experiments.

The model base was made of ABS and Polycarbonate. The gears were made of Polyacetal. The tiltable link was made of Aluminium alloy.

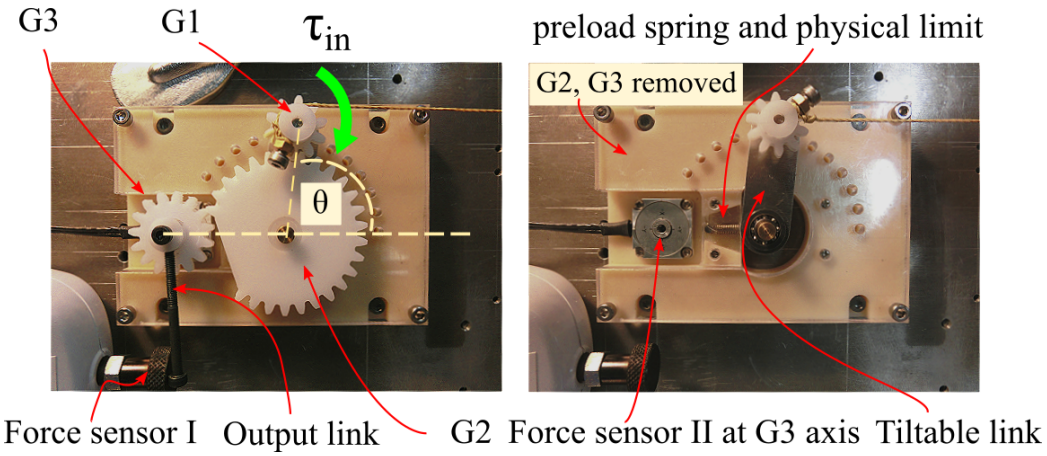

Figure 4-8: Test model of the gear-clutch and its experiment setup

Table 4.1: Specification of the gear-clutch test model

Parameter	Variable	Value
Pitch radius of G1	r_1	7.5 mm
Pitch radius of G2	r_2	22.5 mm
Pitch radius of G3	r_3	11.25 mm
Gears module	m	1.5 mm
Pressure angle	α	20°
Spring constant	k	0.052 N/mm
Spring preloaded force	F_{sp}	0.312 N
Experiment input torque	τ_{in}	25, 50, 75, 100 mNm
Experiment link angle	θ_{exp}	$0 \sim 144°$ /12° step increment
Jamming angle	β	32.53°
Jam-free condition	θ	$86.29° < \theta < 158.76°$
Stable mesh condition	θ	$0° < \theta \leq 140°$

First, G2 and G3 were set so that they always encounter jamming in engagement. The output link was positioned to barely touch the force sensor with zero readings. Then water weights were used to supply input torque τ_{in} to G1 via Kevlar cable. In jamming, the reaction force at the teeth directs radially to the center of G3 and cannot transmit torque. Therefore, the non-zero reading of the force sensor I (AIKOH, RX-50) was used as an

indicator that G2 successfully negate the jamming and meshed properly with G3. Force sensor II (Tecgihan, USL06-H5-50N) was located at G3 and was used to measure the force acting onto the G3 axis. The jam-negation and stable meshing behaviors of the gear-clutch were tested for each tiltable link angles θ. The input torques were also varied with four different values. Fig. 4-9 shows the experiment result. All the cases considered in the experiment are represented by the small dots. The cases that resulted in both jam-free and stable meshing are highlighted in the graph (areas B and C). The result shows that the intersected range of θ calculated from the mathematical model could reasonably predict the usable range of θ. Deviations from the calculated value are shown in areas A and C. The main cause for these deviations is the assumption of frictionless contact between gear teeth. In reality, the friction affects the jam-free condition by resisting the slip-and-engage movement of the jamming teeth. Therefore resulting in an unusable margin shown in area A. Part of area A is unknown if it has jam-free or not because of the coarse resolution of the test cases. However, the lower portion of area A with $\theta = 96^\circ$ and $\tau_{in} = 25$ mNm clearly shows the effect of friction preventing jam-free engagement. In this case, the tangential force F_{lt} of the link can be calculated from Eq. 4.11 to be -0.364 N. The negative sign shows that the force caused the net disengaging moment on the tiltable link, allowing for jam-free engagement of the gear. However, when compared to $-F_{sp} \sin\theta$ which equals to -0.310 N (Eq.4.12) F_{lt} was only higher than the spring force by a tiny margin and could not overcome the friction forces. On the other hand, friction helps prevent the gears from disengaging in unstable meshing. Thus, as shown in area C, the actual usable range extends over the calculated stable meshing condition.

Fig. 4-10 shows snapshots of a successful case in area B at $\theta = 96^\circ$ and $\tau_{in} = 50$ mNm. This case was able to maintain stable meshing state of the gears.

Force measurements of the force sensor I and II also provide additional insight to the experiment result. Fig. 4-11 shows the force measurements, where F_x and F_y are the forces measured by the force sensor II. F_{out} is the force measured by the force sensor I. Their sign conventions are shown next to the graph.

The highlighted area spanning from 0 deg to 12 deg were too close to the singularity of the gear-clutch mechanism at 0 deg. The link snapped pass through the singular point,

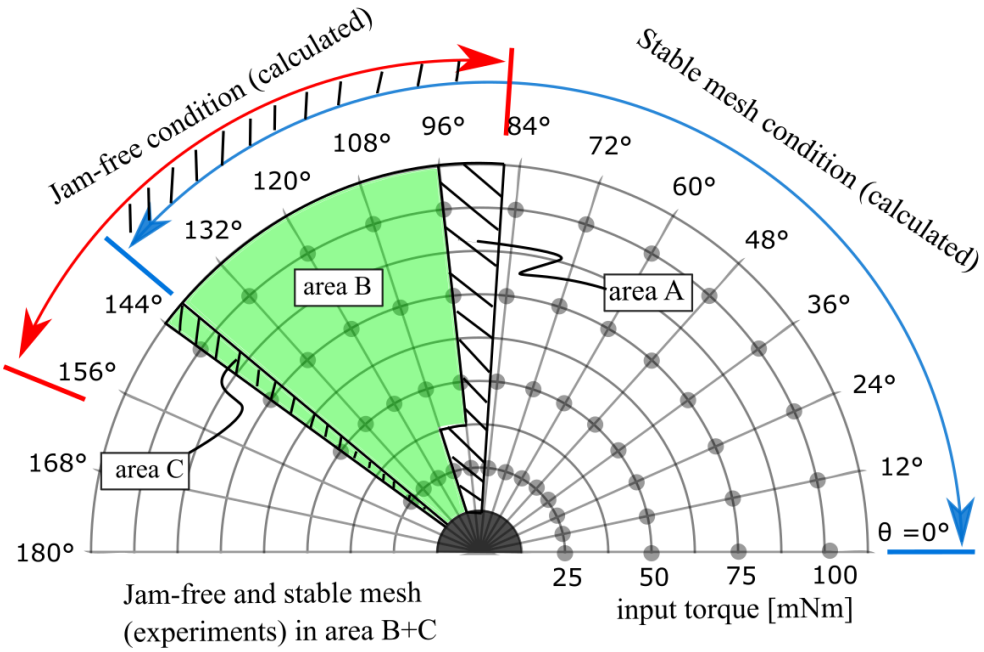

Figure 4-9: Experiment result of the gear-clutch plotted in polar coordinate

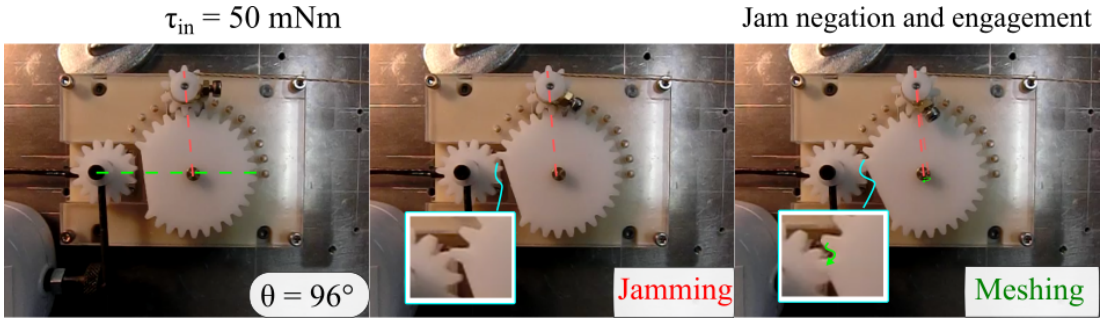

Figure 4-10: Snapshots of a gear-clutch experiment case in area B ($96°$, 50 mNm)

breaking the desired configuration of the gear-clutch as shown in Fig. 4-12. This is because the material of the test model base was plastic which could not rigidly hold the tiltable link at these angles. Therefore, the force measured in this highlighted area did not accurately represent the gear-clutch model. However, the calculated working condition was $86.29° < \theta \leq 140°$, way beyond this unusable highlighted range. The remaining data was sufficient to verify the concept and mathematical model of the gear-clutch mechanism.

Next, considering the different force direction during jamming and meshing state of the gears, this change in direction resulted in the shift in the force measurement values

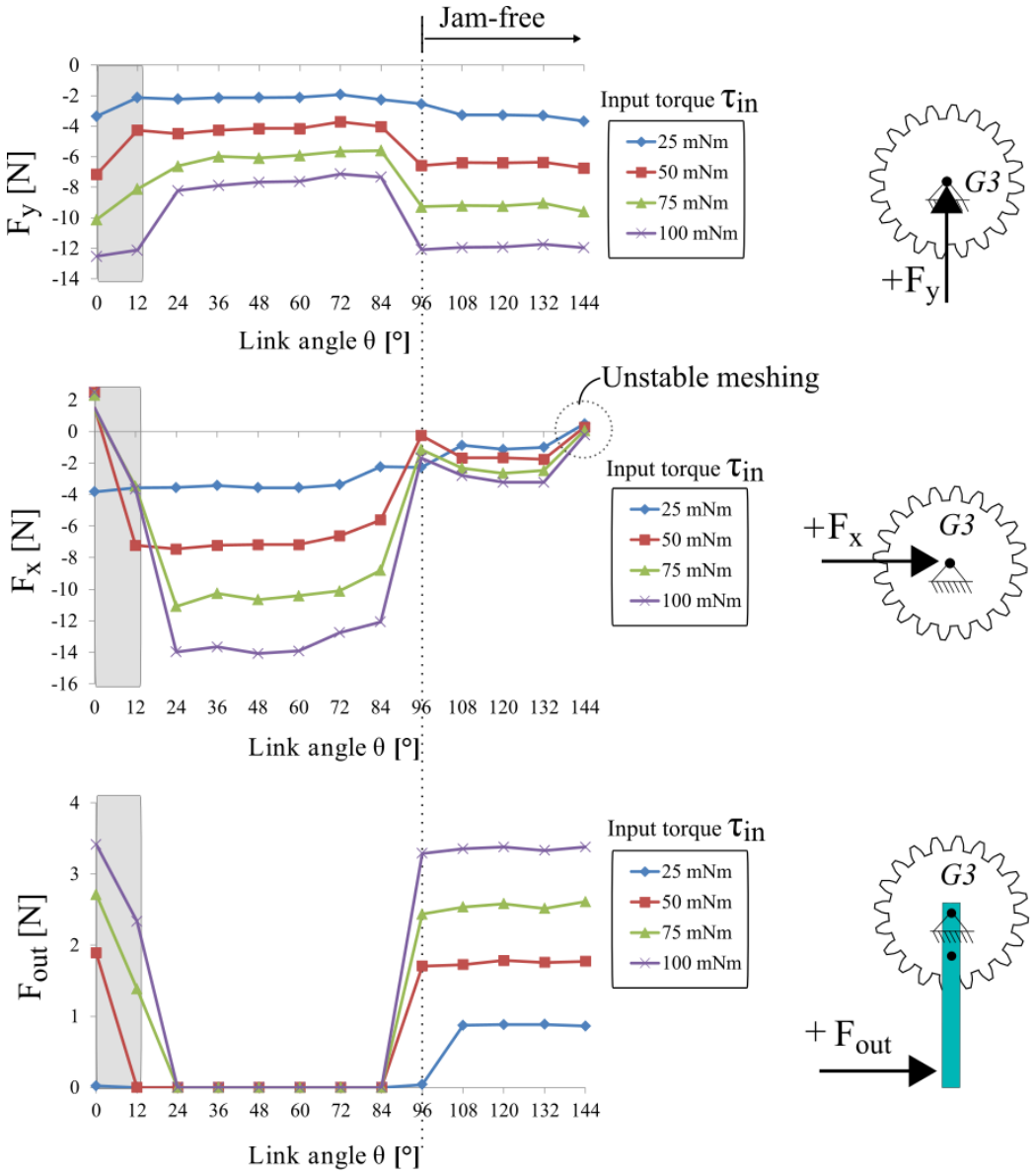

*Highlighted area are near singularity and the result could not be properly measured

Figure 4-11: Force measurements of the gear-clutch experiment

of F_x and F_y. Accompanying the result, Fig. 4-13 compares the force measurements between jamming and stable meshing. In Fig. 4-11, the higher F_y in the negative direction, combined with the diminishing F_x at $96°$ helps confirm that the gear-clutch was in jamming state at $\theta = 84°$ and then changed to a meshing state at $\theta = 96°$. In addition, the increase in F_{out} also confirmed that the meshing could properly transmit torque, verifying the jam-

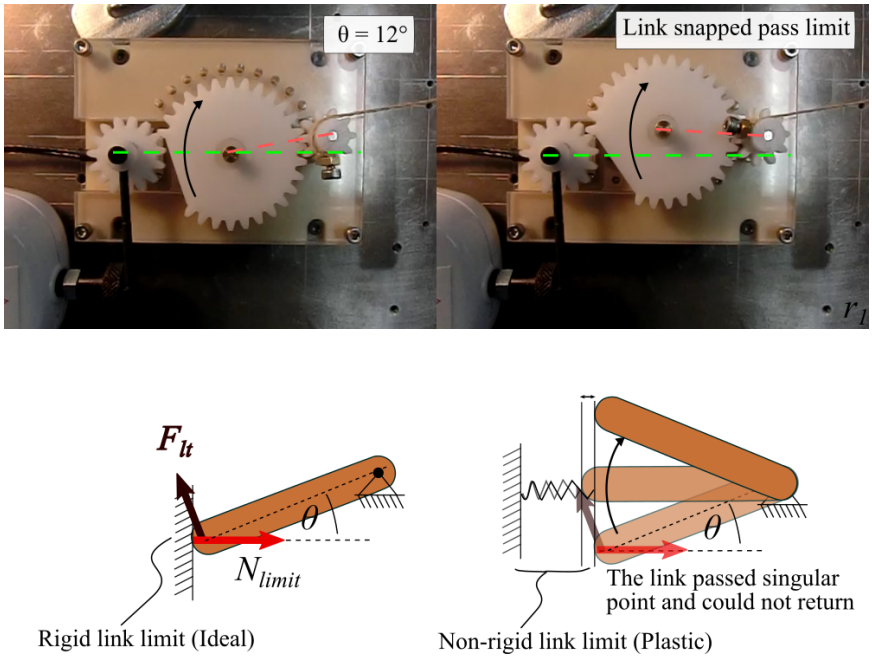

Figure 4-12: Snapshots from gear-clutch experiment at $\theta = 12°$

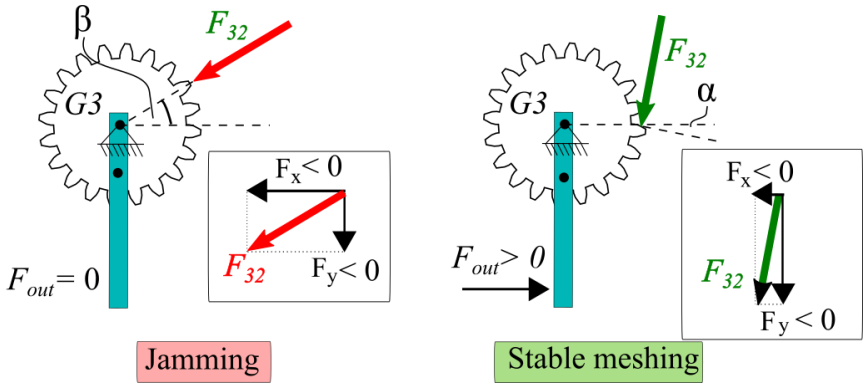

Figure 4-13: Illustration of force measurements during jamming and meshing

free engagement. Furthermore, F_x value at $144°$ experienced a cross to the positive side, contradicting to the slightly negative value in the span of $96° - 132°$. As $\theta = 144°$ exceeds the calculated stable meshing condition ($0° < \theta \leq 140°$, the moment acting on the tiltable link tends to switch its direction to counter-clockwise. That means G2 tends to disengage from G3 at $\theta = 144°$. With the presence of friction at the gear teeth, Fig. 4-14 explains why the change in F_x from negative to positive represents unstable meshing state of the mechanism.

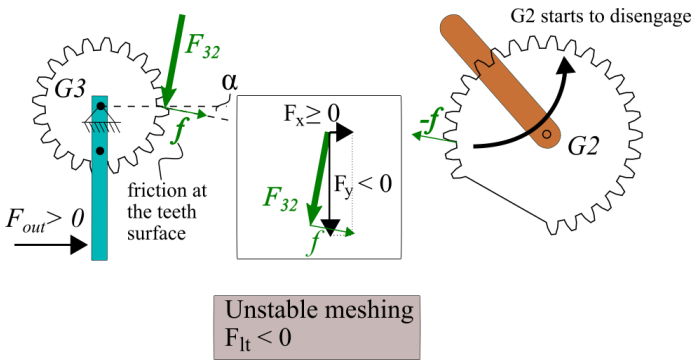

Figure 4-14: Illustration of force measurements during unstable meshing (with friction)

It can be concluded that the developed mathematical model could be used to predict the clutch behavior. The two conditions can be used as a design guideline for the future development of the proposed gear-clutch. Furthermore, Eq.4.12 could also be used to estimate the minimum τ_{in} required to win over the spring force for the jam negation process at a specific θ. Still, an input torque of at least 3 times this minimum τ_{in} is advised in order to overcome friction forces in actual applications. As a design guideline, a higher value of θ should be used because the friction effect becomes less significant. As long as it does not exceed the upper bound of the usable range, higher θ would also mean lower minimum requirement on the input torque τ_{in} for jam negation (Eq. 4.11).

4.1.3 Possible extensions of the gear-clutch mechanism

Variations in the link design and arrangements

Because G2 only need a small tangential movement in the jam negation, alternative configurations can be used without having much difference in its performance. Fig.4-15 shows some of these alternative configurations, such as confining the G2 axis in a guiding slot or by adding a rotational link to the G2 axis in the opposite direction to G1.

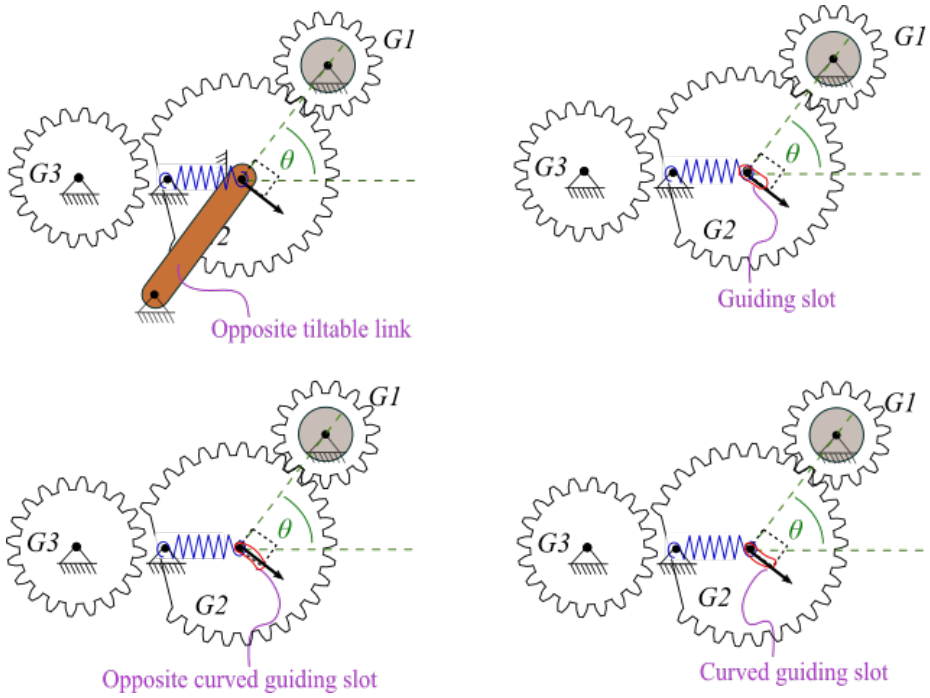

Figure 4-15: Alternative configurations of the gear-clutch

Integrated gear train

The proposed mechanism essentially uses gears as the clutch component. Therefore, it is possible to add complexity to the gear train to achieve a variety of gear reduction ratio. The simplest way to do this is by stacking gears and integrate it directly into the gear-clutch component as shown in Fig. 4-16. For clarity, pitch outlines of the gears are shown while hiding the gear teeth. G2 and $G2b$ are fixed to rotate together. G1 engages with $G2b$.

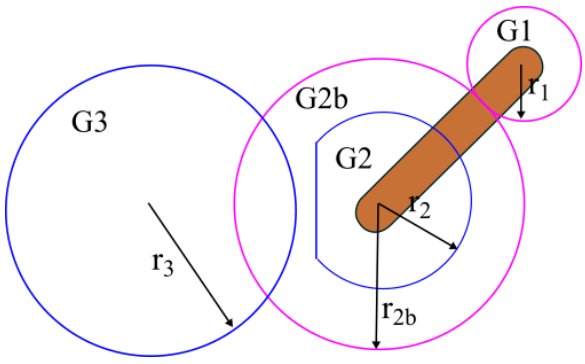

Figure 4-16: Integrated gear train with gear-clutch mechanism

The condition for jam-free and stable meshing can be easily adjusted to the integrated gear train. As the engagement between G2 and G3 remains the same, the equation for the jamming angle β is the same as Eq.4.7. On the other hand, the jam-free condition is changed slightly as follows

$$\frac{\pi}{2} + \beta - \cos^{-1}\left(\frac{(r_2 + r_3)\sin\beta}{r_{2b}}\right) < \theta < \frac{\pi}{2} + \beta + \cos^{-1}\left(\frac{(r_2 + r_3)\sin\beta}{r_{2b}}\right) \tag{4.18}$$

Now consider the stable meshing condition, Eq. 4.5 is now changed to

$$\cos(\theta + \alpha) \geq -\frac{r_2}{r_{2b}}\cos\alpha \tag{4.19}$$

Fig. 4-17 shows a graphical representation of the above equation. This can be solved into two cases. In the case $r_2/r_{2b} > 1$, stable meshing for all θ available. On the other hand, for the case $r_2/r_{2b} \leq 1$, the stable meshing condition is in the following range

$$0 < \theta \leq \cos^{-1}\left(-\frac{r_2}{r_{2b}}\cos\alpha\right) - \alpha \tag{4.20}$$

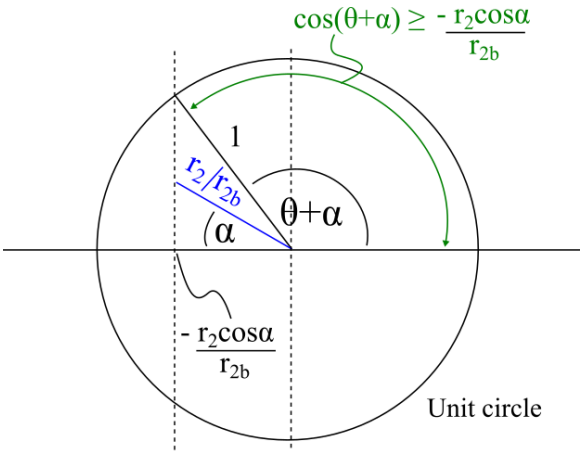

Figure 4-17: Graphical representation of Eq. 4.19

By using the adjusted conditions for jam-free and stable meshing introduced here, one can have more variations and choice during the design process of the developed gear-clutch mechanism.

4.1.4 Conclusion on gear-clutch mechanism

A novel gear-clutch mechanism was developed to provide a potential solution for the stroke limitation of the rack-tilting clutch. The basic concept and its mathematical model were introduced and verified by experiments. The experiment result confirmed that the proposed conditions for jam-free and stable meshing could be used to design the usable range of tiltable link angle θ. Some deviations from the theoretical values could be explained by the existence of friction in the real world applications and were discussed in detail. Some possible extensions such as possible alternative configurations of the tiltable link and guiding slots were also discussed. Furthermore, various design possibility could be enhanced by integrating additional gear trains into the gear-clutch mechanism. In addition, the gear-clutch can operate as a one-way clutch and allow the output and G3 to rotate faster than G2 even if the clutch is engaged. Fig. 4-18 shows the one-way ratcheting effect of the gear clutch when the output is driven forward, and G3 becomes a driver to G2. Detailed analysis of the one-way behavior and backward drive of the clutch can be found in Appendix of this thesis.

Next section introduces a robot joint LRT using the proposed gear-clutch mechanism. The joint prototype is to be used to investigate actual utility of the gear-clutch in two-phase load lifting application which requires long HF stroke.

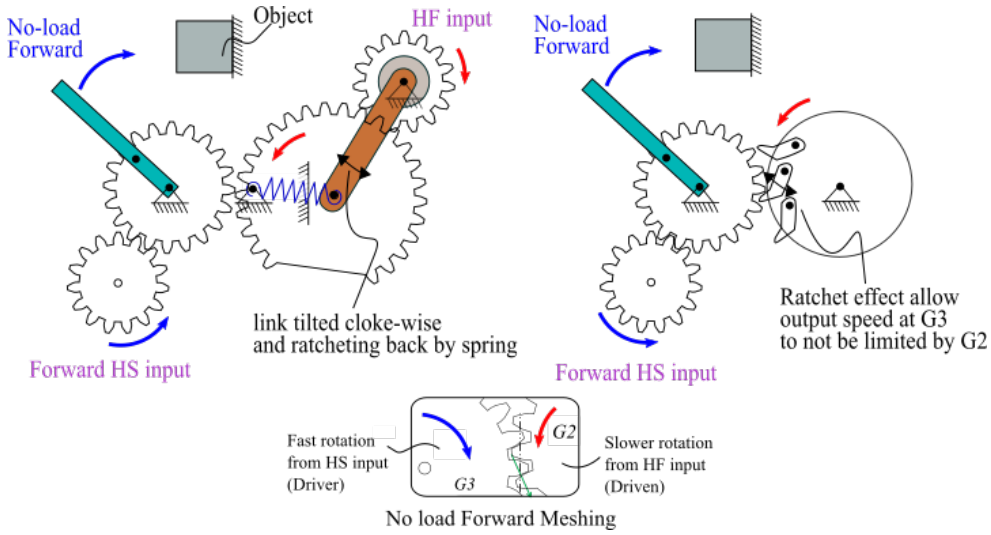

Figure 4-18: Gear-clutch as a one-way clutch in low-load forward drive

4.2 Robot joint LRT with the gear-clutch mechanism

Unlike robotic hands that prioritize on grasping of objects, robotic joints used in, for instance, robotic arms may need to exert high output torque over a longer travel length or angle. Therefore, elbow joints can be thought of as a suitable candidate to demonstrate an application of LRT with the developed gear-clutch mechanism. Also, the one-way characteristic of the gear-clutch mechanism is suitable to use in application that needs to exert high output torque in one direction such as pulley or elbow joints used to lift heavy load in one-direction.

4.2.1 Actuation scheme

Fig. 4-19 shows the actuation scheme of a joint LRT using the developed gear-clutch. A motor M is connected to a differential mechanism, which then distributes its output to low reduction G_L and high reduction G_H gear trains. Instead of using a preloaded spring as in the cable-driven LRT, a slip-type torque limiter is used to make the clutch load-sensitive. That is, when the load is lower than a threshold set by the torque limiter, the motor power is transmitted through the differential D to G_L, resulting in HS phase of the robot joint. In higher load application, the threshold torque is overcome. The torque limiter then slips,

causing the gear-clutch to engage and produce the HF phase of the joint LRT. Using a torque limiter is more beneficial than a preloaded spring because the slipping torque of the torque limiter remains constant throughout the whole HF travel range.

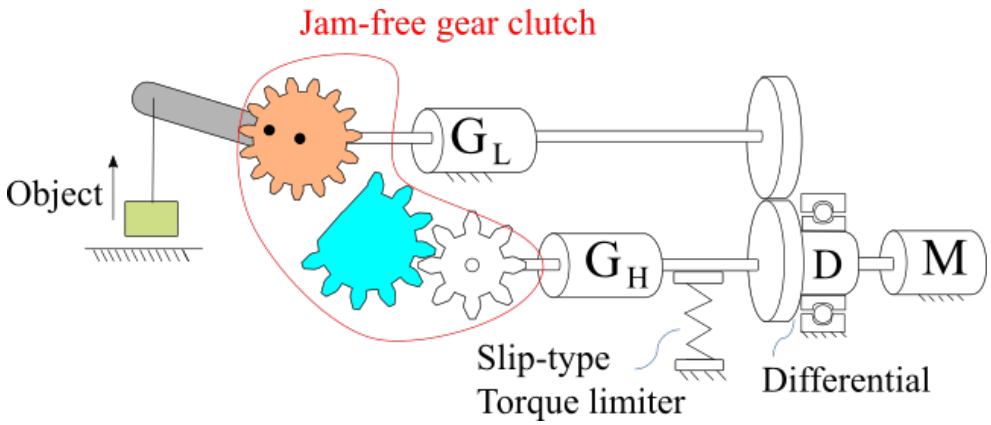

Figure 4-19: Actuation scheme of the robot joint LRT utilizing gear-clutch mechanism

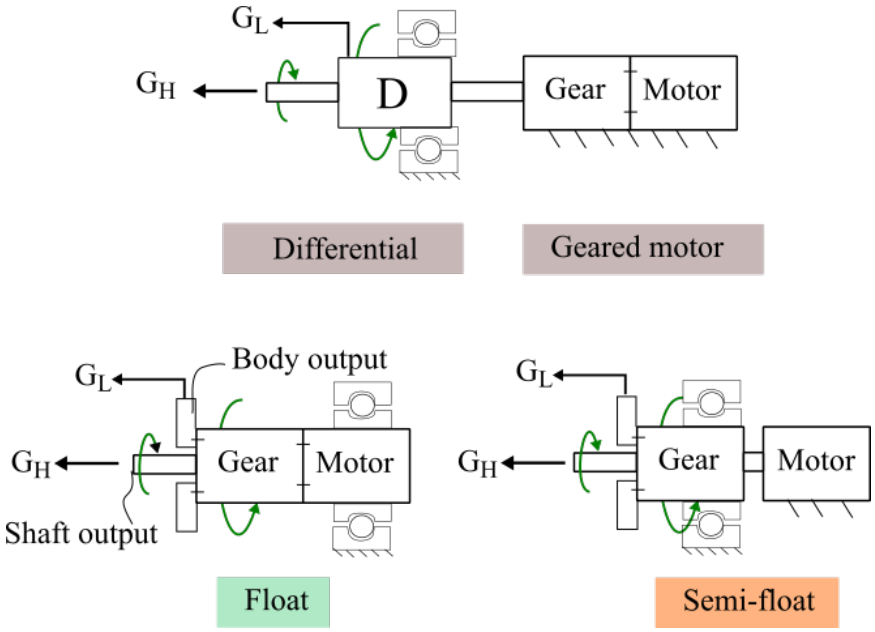

Figure 4-20: Float and semi-float configuration of motor as a differential unit

To further reduce the size of the joint LRT, the motor itself can be used as a differential mechanism. Fig. 4-20 shows such configurations. The top half shows a typical geared motor connected to a differential mechanism. The lower half of the figure shows two

alternative configurations to use the motor as a differential. It can be separated into two types: float and semi-float types. Float type is achieved by, literally, allowing the body of the geared motor to float (not fixed to the frame). The body output can then be used to provide additional input to the joint mechanism. Since the motor torque is produced by electromagnetic forces pushing the rotor against the stator coil, the body output rotation is always in the opposite direction to the shaft output. The use of a motor in float configuration allows us to discard the differential unit from the actual design and thus gives a possibility for a more compact joint LRT. However, the disadvantage of the float type is that the electric poles of the motor rotate and cause difficulty to the motor wiring. The problem can be solved by using a slip ring or rotary connector to connect such rotating poles. On the other hand, this issue can be eliminated by the semi-float type, which its gear is floated and the motor is fixed. The semi-float type should be the best choice if the gear and motor can be separated. A possible difficulty is that the motor case has to be in concentric with the gear. Depending on the fixing method, this might result in a longer length of the mechanism, i.e., bigger space required for the mechanism design.

4.2.2 Mathematical model

Fig. 4-21 shows the working principle of the joint LRT. The motor block refers to a geared motor in floated configuration.

Float type

The motor body output is connected to G_L and the motor shaft output is connected to G_H with a torque limiter apply at the motor shaft output. The joint output torque τ_{out} and the reduction ratio of the LRT can be determined from

High-speed phase (HS) and transition: $\tau_m \leq \tau_{th}$

$$\tau_{out} = \tau_m \eta_L G_L \tag{4.21}$$

$$R_{HS} = G_L \tag{4.22}$$

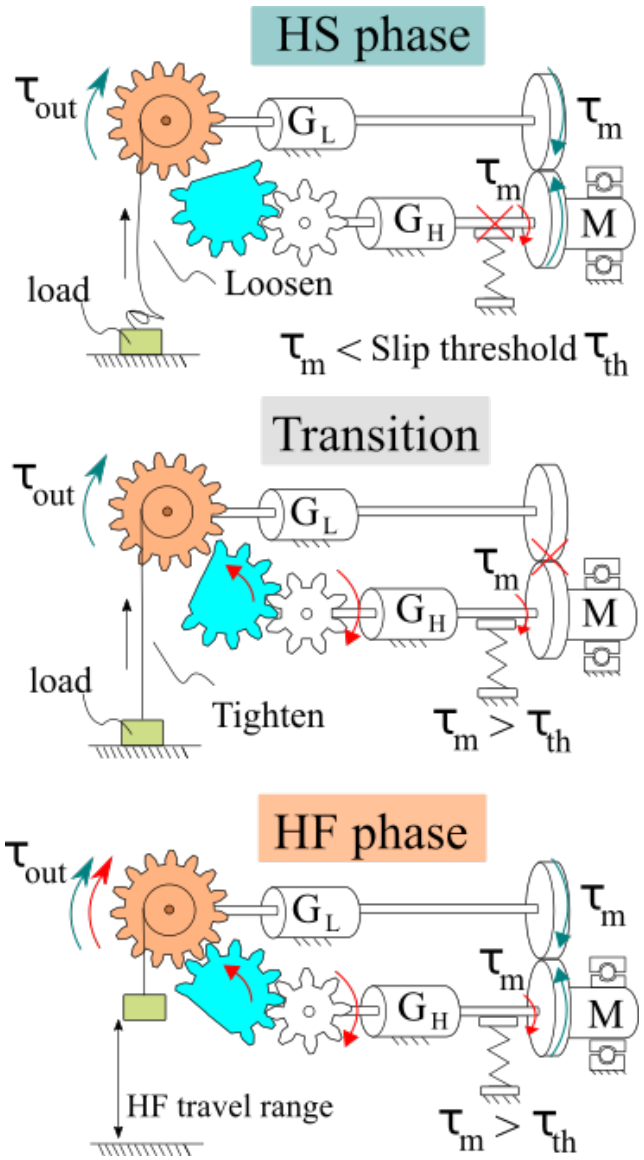

Figure 4-21: Working concept of the developed robot joint LRT (Floated motor)

High-force phase (HF): $\tau_{gm} > \tau_{th}$

$$\tau_{out} = \tau_m(\eta_H G_H + \eta_L G_L) - \tau_{th}\eta_H G_H \tag{4.23}$$

$$R_{HS} = G_L + G_H \tag{4.24}$$

where τ_m represents the output torque of the motor, and τ_{th} represents the effective threshold torque acting on the motor output shaft by the torque limiter. G_L and η_L are the reduc-

tion ratio and transmission efficiency of the low reduction gear train, respectively. Likewise, G_H and η_H are the reduction ratio and transmission efficiency of the high reduction gear train, respectively.

Semi-float type

In this case, the motor is fixed and the gearbox is floated as a differential. This is equivalent to the analysis of LRT introduced back in Chapter 2. Although the calculation is a bit different from the float type, if the motor gearbox has high reduction ratio, the motor effect can be neglected. The equations of the float type can be used to estimate the semi-float type without losing much accuracy.

Stiffness and load holding ability

The torque limiter simply acts similar to a friction brake on the shaft. According to the discussion on stiffness in Chapter 2, this means if the backdrive torque is high enough to overcome τ_{b0}, the output stiffness during the slip or transition would theoretically equal to zero as the backdrive torque is constant. However, if τ_{b0} is set to a high value, the output stiffness then depends on the backdrivability of the motor. If the motor is non-backdrivable, active stiffness control on the motor can help improve compliance of the output link.

There is also an additional merit of using a torque limiter. That is the braking torque of the torque limiter can be used to hold the load in HF phase even when the motor is turned off. Due to the high reduction ratio in HF phase, the backdrive torque need to over come the braking torque from the torque limiter. Neglecting the friction between the motor shaft and body, the minimum backdrive torque required to backdrive the output link in HF phase can be calculated by

$$\text{minimum } \tau_{bd} \quad = \quad \tau_{th} \frac{G_h}{\eta_h} \tag{4.25}$$

τ_{bd} is the amount of the passive-load holding ability of the LRT when offline. Note that the friction between motor shaft and its body, if any, adds more load holding ability to the value calculated in Eq. 4.25.

4.2.3 Joint Prototype

The joint prototype was designed with prosthesis artificial elbow joint as references. Table 4.2 summarizes some information from the review paper [63, 64] of the available upper limb prostheses.

Table 4.2: Characteristics of available prosthesis elbows

Characteristics	Utah Arm	NY Electric Elbow	Boston Elbow
Weight	913 g(elbow)	550 to 620 g	960 g (elbow motor 605 g)
Maximum active lift capacity	4.3 Nm	3.4 Nm (stall)	5.9 Nm
Range of motion	0-135 deg	0-135 deg	0-145 deg
No load speed	112.5 deg/s	100 deg/s	123 deg/s

The target maximum output torque of the prototype in HF phase was set at 4 N.m. The target low-load speed in HS phase was set at least 200 deg/s, approximately two times of the no load speeds of the available upper limb prostheses. This is to show the advantage of the ability to switch the reduction ratio. The target range of motion was set to satisfy the total of 165 deg (hyperextension 15 deg and flexion 150 deg) [65]. The target weight was set to be about the NY electric elbow shown in Table 4.2. Table 4.3 summarizes the design targets of the joint prototype.

Table 4.3: Design target of the robotic joint

Characteristics	Design Target
Weight	Approx. 600 g
Maximum lift capacity (HF phase)	4 Nm
Range of motion	more than 165 deg
No load speed (HS phase)	more than 200 deg/s

According to the design, parts were manufactured and assembled. Fig.4-22 shows the developed joint prototype. The sizes are shown in mm. The transmission can be divided into two sections, L side and H side. L side housed the gears of the low reduction path and the motor outputs. H side housed the gear-clutch mechanism. The joint output shaft was laid through both sections and was supported by three bearings at the frame. The geared motor was floated by two bearings, one at the motor shaft and another one at the motor case. The total weight of the prototype was approximately 650 g without the output link. Which is close to the target of approximately 600 g. The weight of only the actuation parts

without frames were 380 g in total.

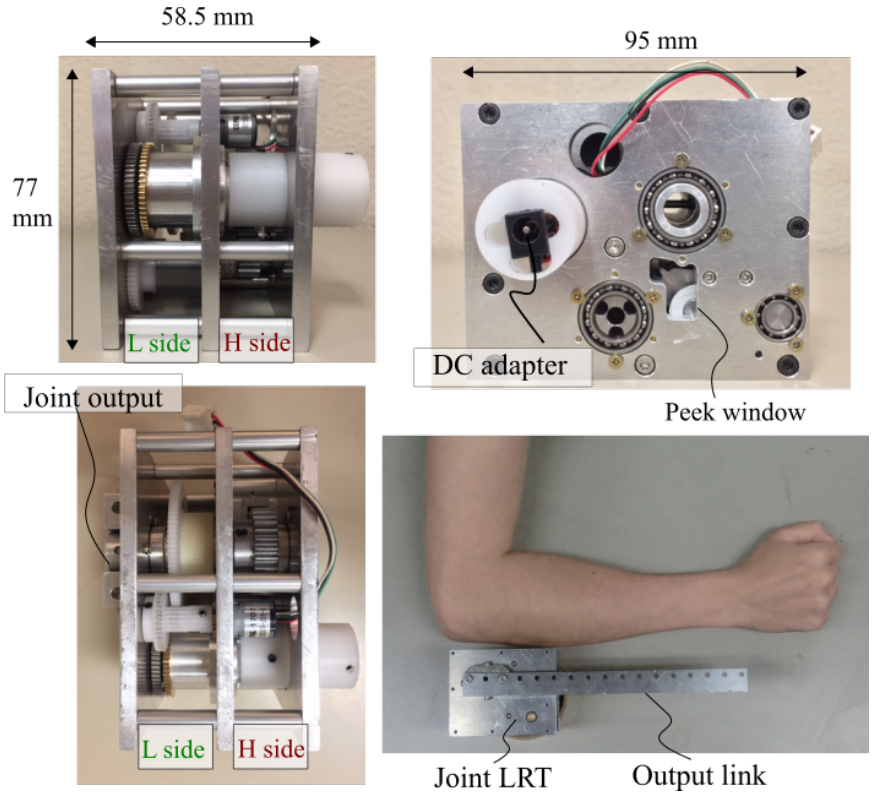

Figure 4-22: Joint prototype

Output link

The output link was made of aluminum alloy as shown in Fig. 4-23. The link had an L-shaped cross subsection. Multipass Finite Element P-Method (FEM) in PTC Creo Simulate 3.0 software was used to simulate the stress profile of the link under 4 Nm load. More information about P-elements method and convergence in PTC creo can be found in [66, 67] Table 4.4 summarizes the property of AL5052 [68] used in the simulation, assuming the weakest, annealed state of the alloy. The output link model was constraint by five pin constraints shown with the small markers. To avoid singularities in simulation, the link was simulated with a uniform force loading on the surface 20 mm long at the free end of the link. The total force acting on this surface was calculated to produce an equivalent of 4 Nm torque around the center of rotation. Fig. 4-24 shows loading and constraints of the output

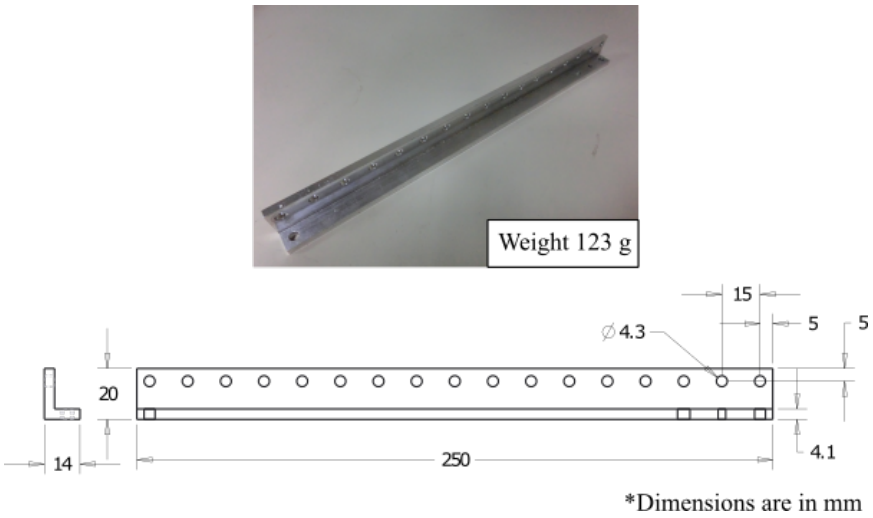

Figure 4-23: Output link of the joint prototype

link, as well as the simulation result. The P-pass graph shows that the Von mises stress value converged within 5% between P-loop pass before reaching the maximum polynomial number of 9. This means the simulation result can be trusted to a certain accuracy. By comparing the maximum von Mises stress σ_{vm} with the yield stress σ_y of the material, the safety factor of the output link was approximately 3 which is sufficient. The weight of the link was 123 g and its total length was 250 mm. The maximum torque τ_l required to rotate this link against gravity was calculated to 150.8 mNm

Table 4.4: Mechanical property of AL5052 used in simulation of the output link

Specification	Value
Density	2.68 g/cm^3
Modulus of elasticity	70.3 GPa
Yield strength	89.6 MPa
Fatigue strength	110 MPa
Poissons ratio	0.33

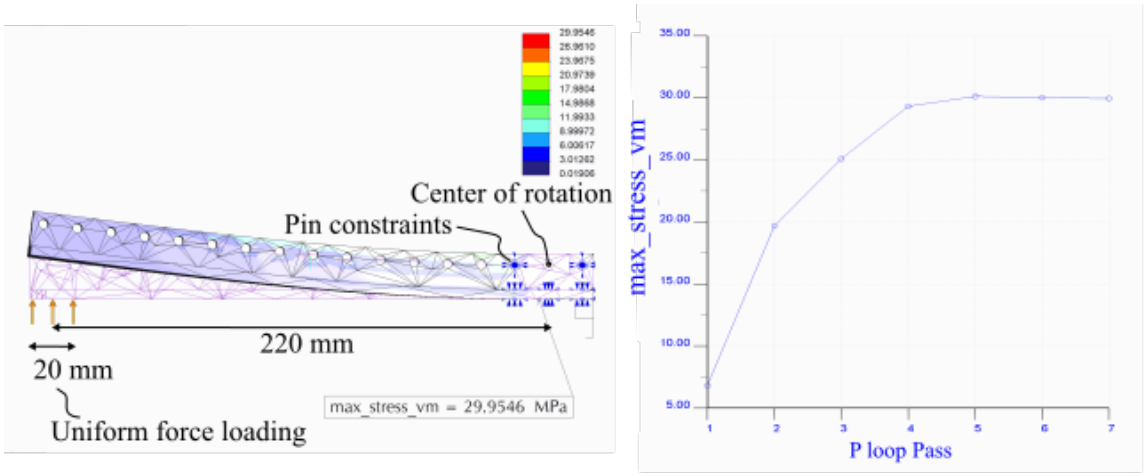

Figure 4-24: Von-mises stress simulation and P-pass analysis on the output link

Motor and Gear

A combination of a geared DC motor, a torque limiter, and reduction ratios G_H, G_L was chosen. The design condition was that the threshold load torque for switching had to be higher than τ_l. Also G_L had to be low enough to achieve a no-load speed of 200 deg/s during HS phase. G_H was sized to achieve 4 Nm in HF phase with the maximum current limit of 30% of motor stall current. Table. 4.5 shows the motor specification. Also, the float actuation type was chosen for the joint prototype because inexpensive DC geared motors often come with its gear as a set and could not be separated without introducing eccentricity problem.

Next, Fig. 4-25 shows a prearrangement of the motor and gears in the joint prototype. Gears m1, i1, i0 and a are gears in the low reduction path G_L and gears m2, i2, b, h, c, d and e represent gears in the high reduction path G_H. Fig. 4-26 shows the gears arrangement from a lateral view. The tiltable link angle of the gear-clutch mechanism can be calculated for this arrangement by cosine law of the geometry

$$\theta = \pi - \cos^{-1} \frac{(d_c + d_d)^2 + (d_d + d_e)^2 - 4L_{ab}^2}{2(d_c + d_d)(d_d + d_e)} \tag{4.26}$$

where d_c, d_d and d_e is the pitch diameter of gear c, d and e, respectively. L_{ab} is the distance between centers of gear a and b. The gears were chosen so that the angle θ acquired from Eq. 4.26 satisfied both the jam-free and stable meshing conditions introduced in the analysis of the gear-clutch.

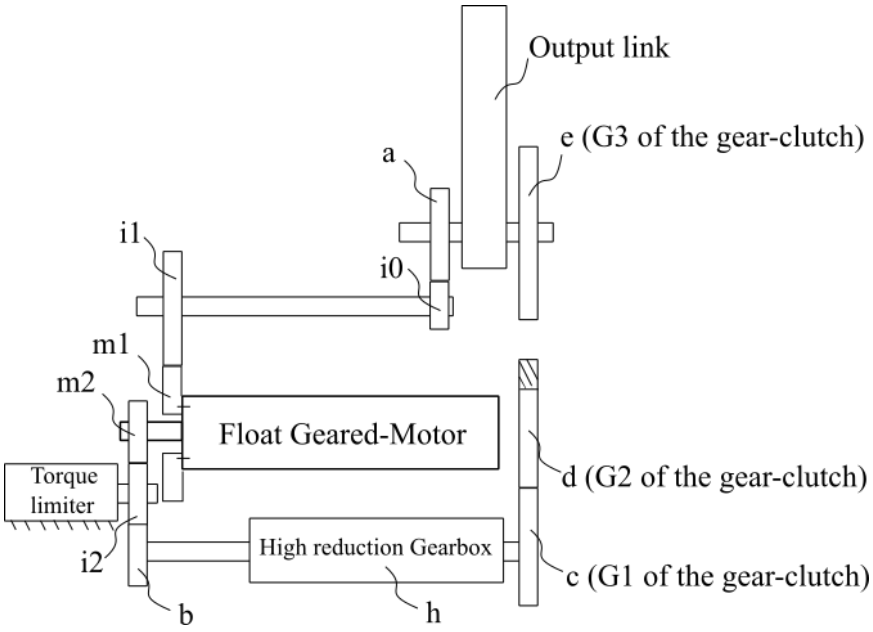

Figure 4-25: Prearrangement of gears in the joint prototype design

In this joint prototype, $G_H = 93.75$ and $G_L = 4.44$ were chosen. The change in reduction ratio HF/HS was then $(93.75+4.44)/4.44 = 22.1$ times. The gear clutch spacing was designed so that the output link could be back driven by at least 90 deg using Eq. 2.45 as discussed in chapter 2. Assuming that the the motor is not backdriven during an impact $\theta_{inb} = 0$, the minimum requirement for the clutch spacing was $90(4.44)/93.75 = 4.3$ deg. With the slowest motor speed at 30% current limit of $180(1 - 0.3) = 126$ RPM, the clutch transition time was calculated to $(4.3)(93.75)(60)/((126)(360)) = 0.53$ s. This is well within the objective of 1 s.

Assuming transmission efficiency of 0.95 in each step of the spur gears and efficiency of 0.7 for the harmonic gear [69]. Accompanying Fig. 4-25, Table. 4.6 lists the gears used in the prototype and other parameters including gear-clutch link angle. Using Eq. 4.25, and the chosen gear specifications, the passive load holding ability in HF can be estimated,

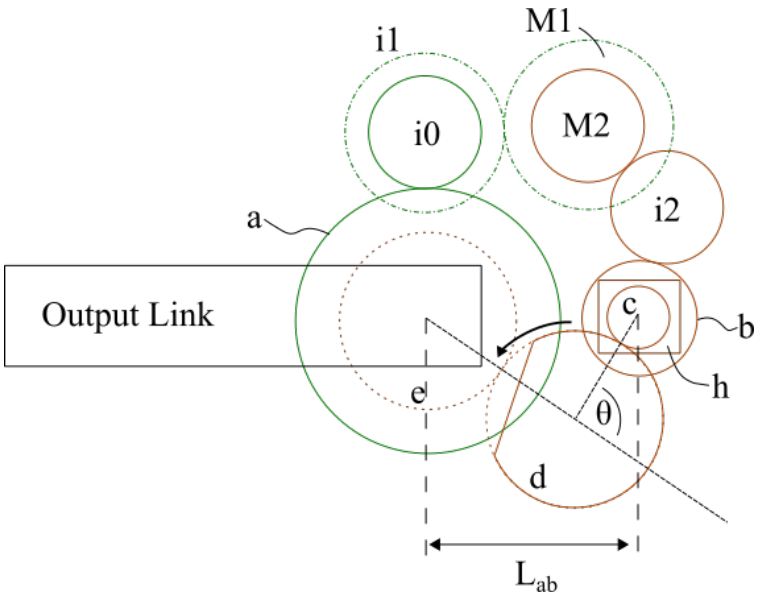

Figure 4-26: Prearrangement of gears in the joint prototype design (lateral view)

$(37.9)(93.75)/0.57 = 6.2$ Nm.

Table 4.5: Motor and torque limiter specification

Specification	Value
Motor	
Part identifier	Pololu 2 W geared motor #1163
Gear ratio	73:1
Nominal voltage	6 V
No load speed	180 rpm
Stall torque	421.4 mNm
Stall current	3.2 A
no load current	250 mA
Size	20D $\times$ 44L mm
Weight	43 g
Torque limiter	
Part identifier	TLES1-816-30W
Slip torque	30 mNm
Threshold torque at motor τ_{th}	37.9 mNm
Weight	13 g

Table 4.6: Gear parts in the joint prototype

Name	Part identifier	Weight
Low reduction path G_L		
Gear a	KG S50D100B-0305	9.2 g
Gear i0	KG S50D15K*0803	1.2 g
Gear i1	KG S50D40B*0303	2.4 g
Gear m1	KG S50B60A-0208	11.2 g
High reduction path G_H		
Gear m2	KHK LS0.5-60	14.2 g
Gear i2	KG S50D50B*0303	3.2 g
Gear b	KG S50D30B*0303	1.4 g
Gear h	CSF-5-100-2XH-F	25 g
Gear c	KG S1S16B-0805	18.5 g
Gear d	KG S1S30A-0808F	41.2 g
Gear e	KG S1S30B*0806	67.8 g
Other parameters		
Name	Variable	Value
Jamming angle	β	20.4 g
Tiltable link angle	θ	98.5 deg
Jam-free condition	θ	64.5 deg $< \theta <$ 156.2 deg
Stable mesh condition	θ	0 deg $< \theta \leq$ 140 deg
Low reduction ratio path	G_L	4.44
High reduction ratio path	G_H	93.75
Design transmission efficiency of G_L	η_L	0.90
Design transmission efficiency of G_H	η_H	0.57

Gear-clutch arrangement

Fig. 4-27 shows the components arrangement in 3D by PTC Creo parametric 3.0 software. The output link is not shown and the frame is made transparent for clarity. Due to the limitation of space, the tiltable link was positioned in the opposite direction. The link rotation center is placed opposite to G1 but preserved the tilt angle θ as calculated. Fig.4-28 shows the tiltable link placement in the gear-clutch mechanism of the joint prototype.

To ensure that G1 always engage with G2, The rotation range of G2 was limited. This was done by using a pin-slot guide as shown in Fig. 4-29. Fig. 4-30 shows more detailed analysis of the pin-slot design. The pin was fixed to the mechanism frame, and the slot was engraved onto G2. In backward drive, when G2 rotates back to its starting position, the pin acts as a rotation limit of G2. The pin provides a clockwise moment to the tiltable link, pushing it against the link rotation limit. In addition, the slot width and position of the pin were designed so that the pin does not collide with the slot wall during the jam-

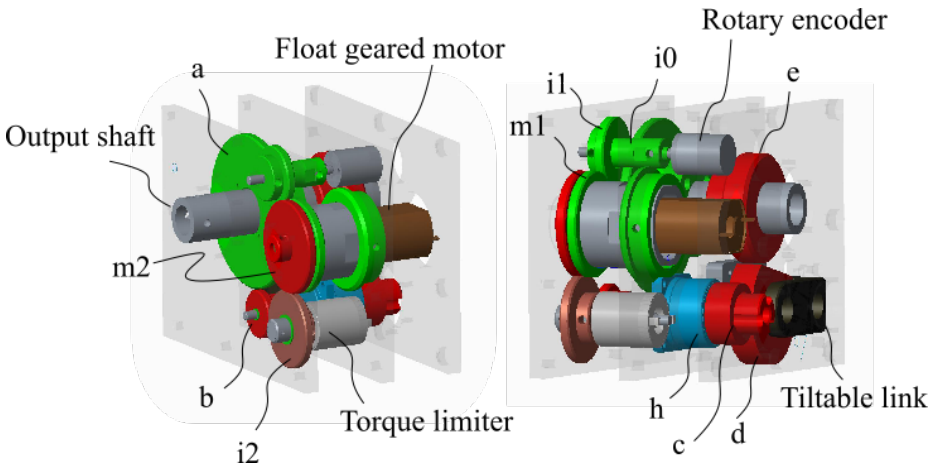

Figure 4-27: Component arrangements of the joint prototype in 3D CAD model.

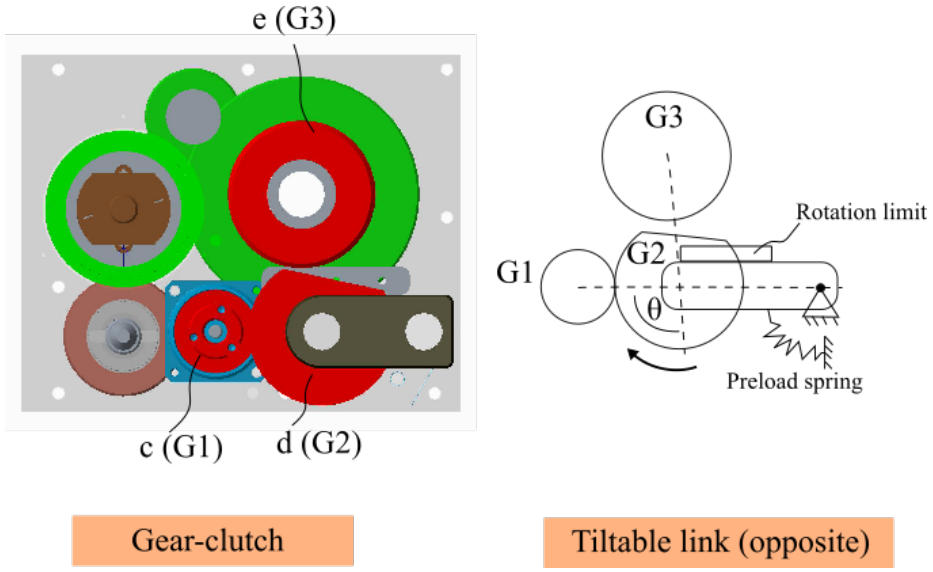

Figure 4-28: Gear-clutch mechanism of the joint prototype.

negation. For standard involute spur gears, the difference between the tip radius and pitch radius is equal to their module m. As the jamming angle β is always less than $\pi/2$. It is safe to assume that, the pin will not collide with the slot wall during the jam-negation if the following condition is satisfied.

$$r_{so} - r_{tp} + \frac{d_{pin}}{2} \geq m \tag{4.27}$$

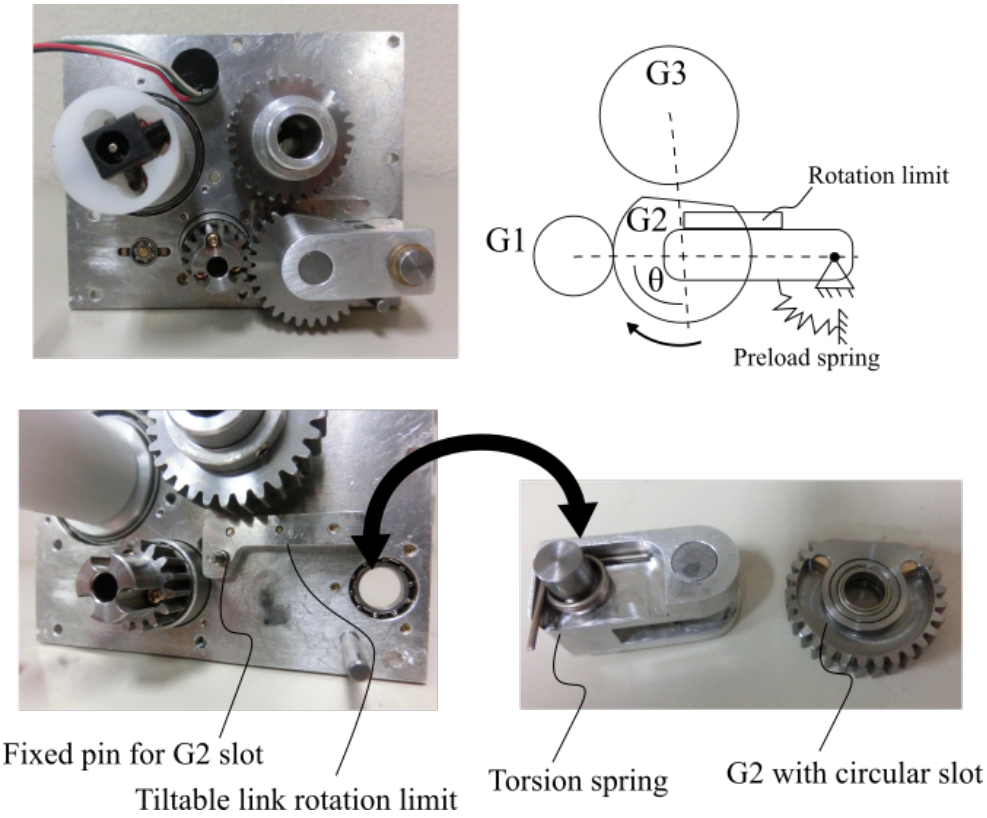

Figure 4-29: Pin and guiding slot in G2 of the gear-clutch mechanism

where r_{so} is the radius of the slot outmost wall, r_{tp} is the radius from G2 center to the pin center and d_{pin} refers to the diameter of the pin.

The slot on G2 or gear d were designed to give a maximum output rotation of 220 deg to the output joint, which is sufficient for the target rotation range of 165 deg set in Table 4.3. The torsion spring at the tiltable link was chosen to be as weak as possible. The spring preload was designed to hold the weight of the tiltable link plus G2. Also, the preload allowed up to 5% of maximum jamming force before the link started to tilt. The spring had a stiffness of 4.58 mNm/deg and was preloaded by approximately 30 deg. Additionally, a rotatable DC adapter was added to the poles of the floated motor. This allowed relative rotation between the electrical cable and the motor. Fig. 4-31 illustrates the rotatable DC adapter.

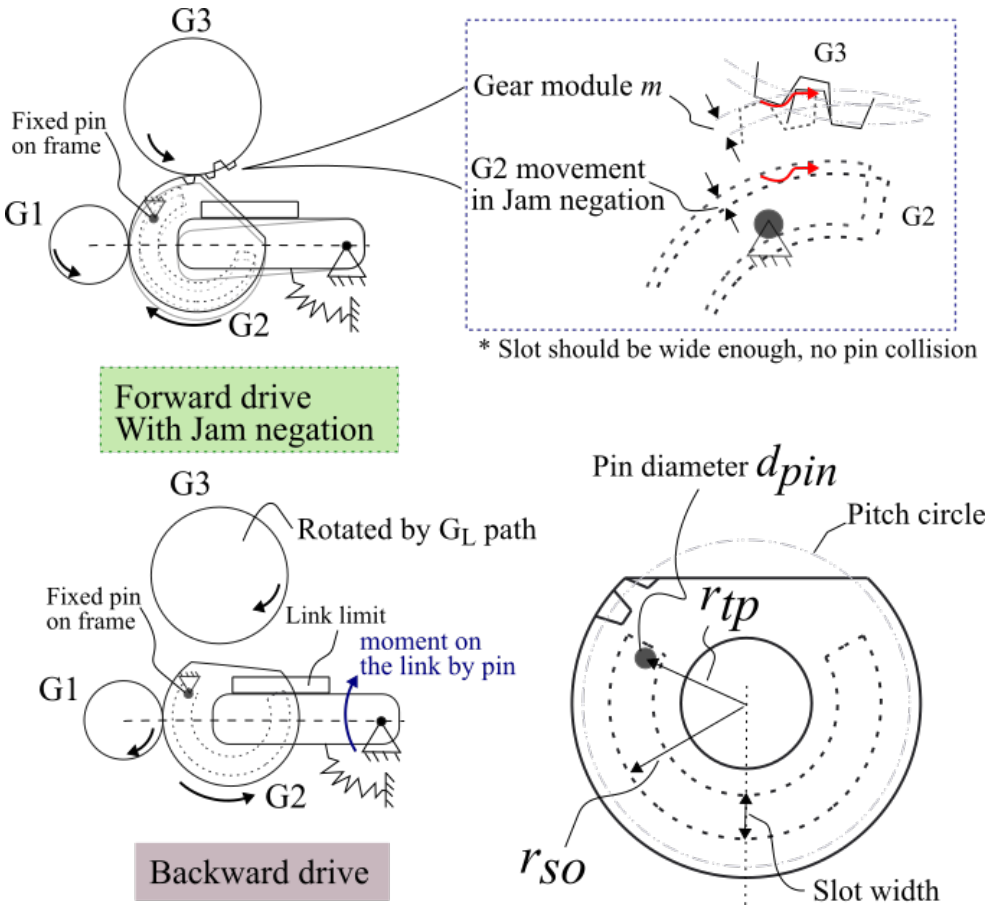

Figure 4-30: Pin and guiding slot analysis

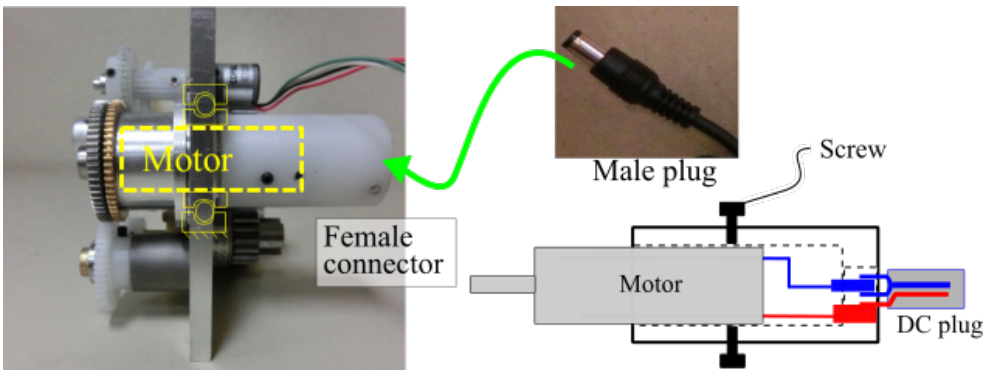

Figure 4-31: Rotatable DC adapter of the motor

Data acquisition

Output rotation angle, output force and motor current were measured to evaluate the joint performance. The motor was driven by Pololu Dual VNH5019 Motor driver [70] connected

to an Arduino Uno Micro-controller [71]. Fig. 4-33 shows the flow of information. In total, there were three sensors. One was a rotary encoder RE12D300-201-1 [72] attached to gear i0/i1 to measure the output rotation angle as shown in Fig.4-32. A hall-effect current sensor Pololu ACS714 [73] was used to measure the motor current. A force sensor AIKOH-RX-5 [74] was used with output link to measure the joint output torque. Table 4.7 summarizes the parts involved in data acquisition.

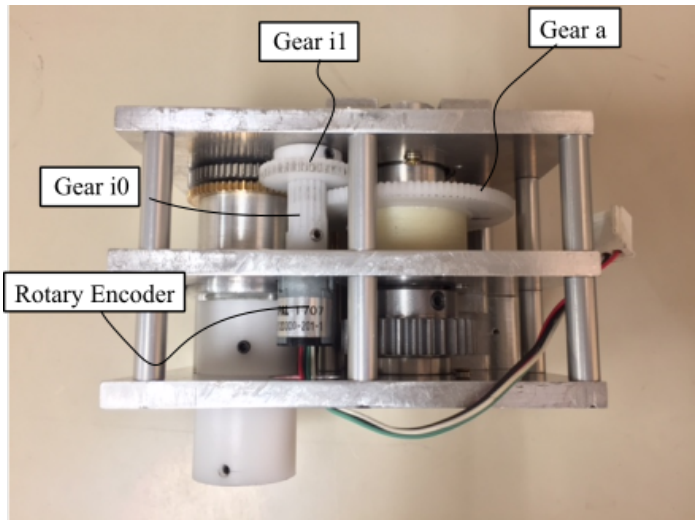

Figure 4-32: Rotary encoder[72] connected to gear i0/i1 shaft

First, a start signal was sent from the PC to both the micro-controller and the force sensor simultaneously. The current sensor and rotary encoder reported the motor current I_{motor} and output angle θ_{out} to the micro-controller through Analog-to-Digital Converter (ADC) periodically using a timer loop of 200 Hz. The micro-controller and the force sensor then reported the recorded data back to PC via a serial connection for further analysis of the results. The motor could also be manually controlled by the three switches shown in Fig. 4-33. SW1 acts as a start/stop switch, SW2 chooses the rotation direction and SW3 resets the data recorded.

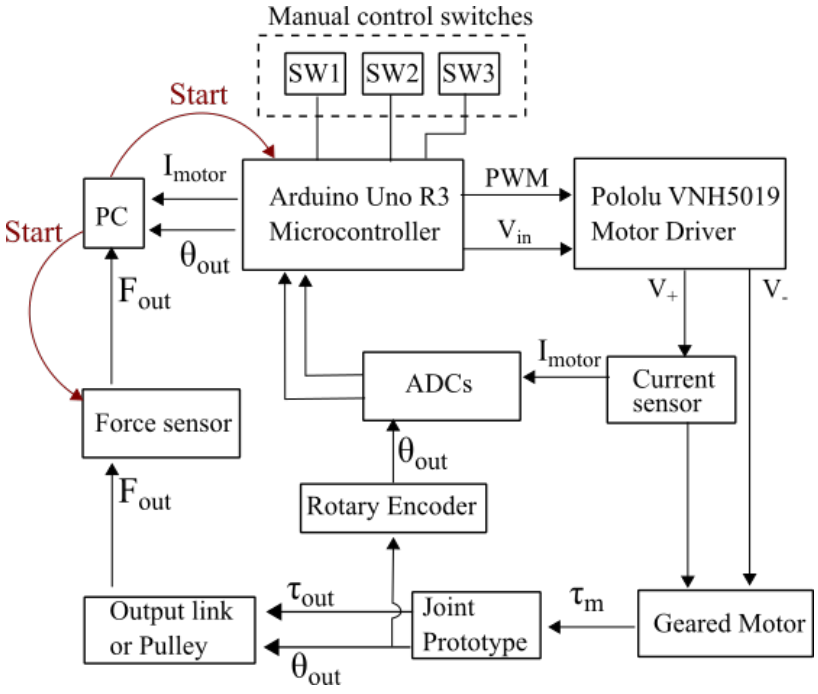

Figure 4-33: Information flow diagram of the joint prototype

Table 4.7: Data acquisition parts

Part	specification
Microcontroller	Arduino Uno R3 [71]
Motor driver	Pololu VNH5019 [70]
Analog-to-Digital Converter Current sensor	10-bit ADC in Arduino Uno R3 [71] Pololu ACS714 [73]
Force sensor	AIKOH RX-5 [74]
Rotary encoder	RE12D300-201-1 [72]
Power supply	Kikusui PMC18-5 [75]

4.2.4 Experiment and results

The experiments were separated into three main parts, jam-free confirmation, output link experiment and pulley lifting experiment. The first one verified if the designed gear-clutch mechanism in the joint can properly provide jam-free engagement. The second one examined the joint static performance when the output link pushed against a force sensor. The last experiment examined the joint behavior when used to lift loads over a long HF stroke.

Jam-free confirmation

This experiment was done by attaching the output link to the output shaft of the joint prototype. A camera was used to record the movement of gear G2 and G3 through the peek window (refer to Fig.4-22. First, the joint was driven to rotate the link toward an iron block. The driving voltage was 6 V, 20 kHz PWM with 100% duty cycle. After the contact was made, G3 which was connected to the output shaft stop moving, then G2 rotated as the LRT change into HF phase. The block height was set so that G3 always experienced jamming with G2. Fig. 4-34 shows the experiment setup and snapshots of the gear-clutch in the experiments. The joint forward direction was defined as shown. The marking line indicates the initial alignment of the tiltable link.

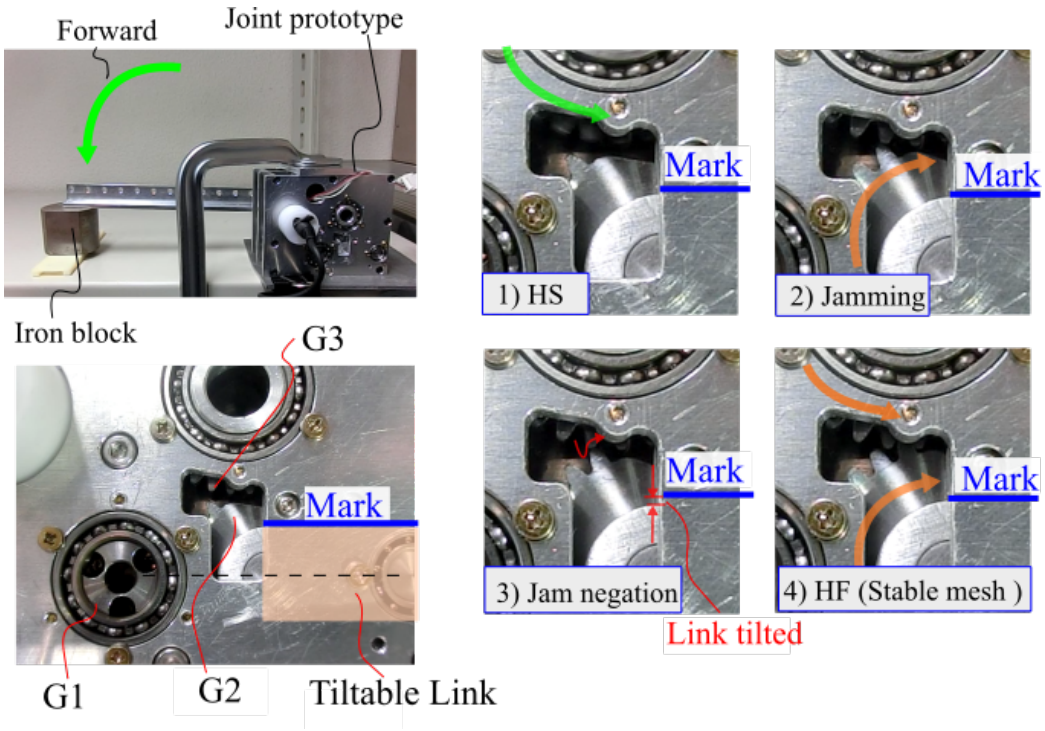

Figure 4-34: Experiment setup and snapshot of jam-free engagement

The snapshots show that the jamming force caused the tiltable link to swing downward in 3). The marking line indicating the top edge of the tiltable link can help identify that the link was tilted. This tilting action allowed the teeth of G2 to slip pass the jamming and engaged with G3. After the gears had entered an engaged state, the tiltable link swung

back to its initial position and ensured a stable meshing state in the HF phase as shown in 4). This result indicates that the proposed gear-clutch mechanism successfully provided the jam-free engagement for the joint prototype. The proposed design method of the gear-cluth was practical enough to be used in an actual design.

The one-way characteristic of the gear-clutch was also verified. Fig.4-35 shows the experiment setup with the snapshots. First, the joint was driven with a load pre-applied to the output link by hand, conditioning the gear-clutch to be in an engaged state. After the engagement had been confirmed, the load was removed. At this moment, G2 and the link started a ratchet-like movement, and allowed the output link to swiftly rotate in the forward direction even when the gear-clutch was in an engaged state. Afterward, the output link made contact with the iron block. The disengaged gear-clutch then re-engaged and entered HF phase of the joint. The result verified the one-way characteristic of the gear-clutch. This behavior might be useful for power assistive application which the driven link may need to rotate faster than the driving transmission.

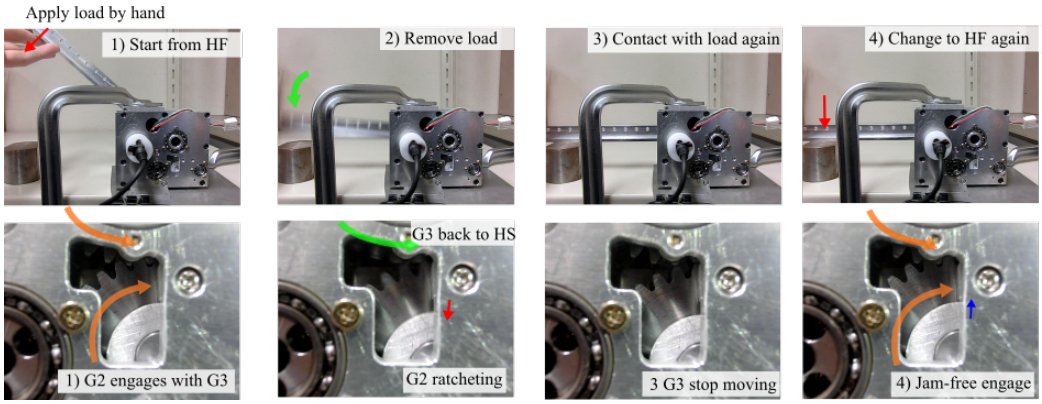

Figure 4-35: Snapshots of one-way clutch experiment

Output link experiment

Fig. 4-36 shows the experiment setup. Note that the joint prototype had been switched its back and front from the previous experiment due to the mounting space of the force sensor. The forward direction in this experiment was defined as shown in the figure. First, the output link was positioned away from the force sensor. Then, the link was driven forward

to toward the force sensor until the motor stalled. The output angle was defined to be zero at the contact point. Afterward, the link was driven backward, away from the force sensor then braked to stop. Specifically, The link was driven forward (toward the force sensor) for 7 s and backward (away from force sensor) for 3 s. The driving voltage was 6 V, 20 kHz PWM with 100% duty cycle. The maximum current was limited by the power supply constant current limit function to 20-30% of the stall current to prevent overheating when the output link stalled. The recordings started simultaneously by the start signals sent by the PC to both the force sensor and the micro-controller.

Fig. 4-37 shows the experiment result with motor current limited at 700 mA (20% of the stall current). The result indicates that the joint LRT prototype could magnify the output torque without much increase in the motor current, which means the magnified output torque was achieved by changing the reduction ratio of the joint.

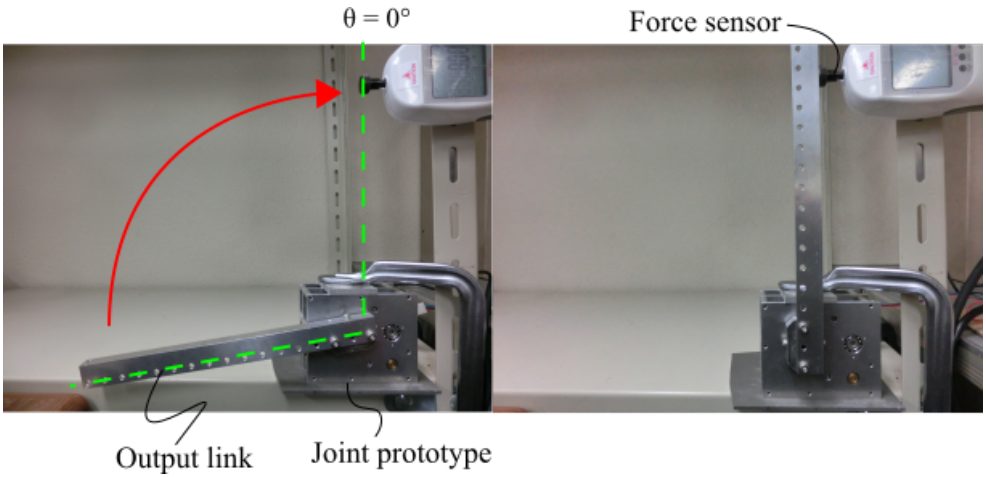

Figure 4-36: Experiment setup for the link experiment

The output angle graph shows that the joint prototype could rotate swiftly before contact with the force sensor, and magnified the output torque after the gear-clutch mechanism engaged. The color bar above the graphs indicates the state of the joint mechanism, high-speed(HS), transition(TR) or high-force(HF). The maximum rotation speed in HS phase was approximately 252 deg/s with an average value of 221.5 deg/s. In HF, the joint could statically deliver up to 3 Nm stalled with 700 mA motor current. The current peak at 8.5 s was because of motor braking. The average backward speed before gear-clutch disengage

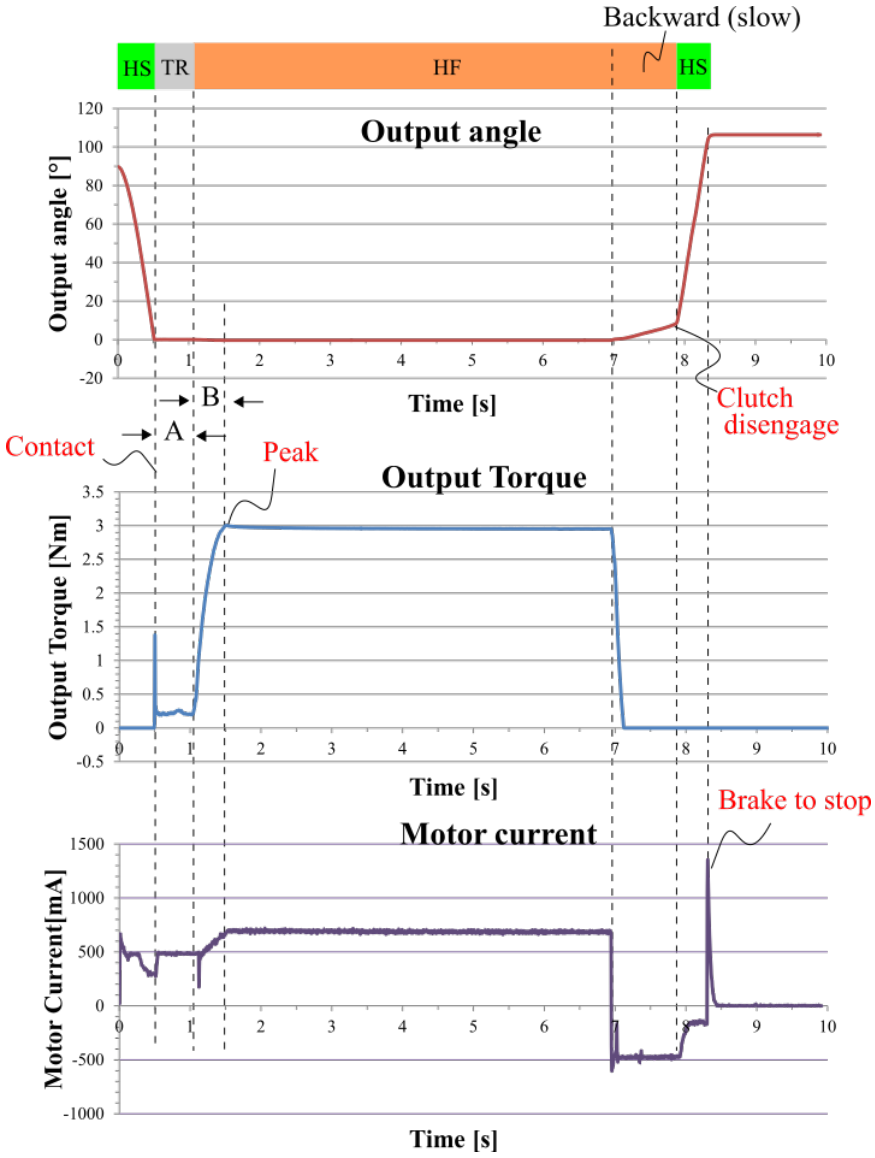

Figure 4-37: Result of the link experiment (700 mA)

was around 9.7 deg/s and back to 220 deg/s right after the gear-clutch disengaged. The slow backward speed was because the output speed was limited by the engagement of the gear-clutch. It has to be noted that the joint could not exert high output torque in backward direction due to its one-way characteristics. To avoid confusion, the slow backward rotation in the clutch engaged state was not referred to as an HF phase. The time used for the output torque to rise were separated into two parts. A was the time used for the clutch to rotate into the engagement and was counted from the contact point. B was the time delay for

the output torque to rise to its peak after the engagement. Delay B was the result of the mechanical compliance and slow speed due to the high reduction. In this experiment, A was measured to be around 0.45 s and B around 0.55 s. The total time delay to realize the HF output torque was then A+B, about 1 s.

From the static experiment results, the torque magnification ratio HF/HS were calculated by the following equation, at the same torque input.

$$M_\tau = \frac{\tau_{HF}}{\tau_{HS}} \tag{4.28}$$

where τ_{HS} was estimated from the output torque during the phase weighted by the motor current. $M_\tau = (3000)(0.5)/(260)(0.7) = 8.3$ Compared with the change in reduction ratio of 22.1 from Table. 4.6, the This means that the actual magnification result in around $8.3/22.1 = 38\%$ of the ideal case. The static transmission efficiency of each reduction path η_L, η_H were also calculated from

$$\eta_L = \left[\frac{\tau_{out}}{\tau_m}\right]_{HS} \frac{1}{G_L} = 0.89 \tag{4.29}$$

$$\eta_H = \frac{[\tau_{out}/\tau_m]_{HF} - \eta_L G_L}{G_H(1 - \frac{\tau_{th}}{\tau_m})} = 0.52 \tag{4.30}$$

The experiment and calculations were repeated for the current limit of 1 A (about 30% of the motor stall current), which should be the maximum current allowable at stall without overheating. Fig. 4-38 shows the experiment result. The maximum output torque around 6.4 Nm was achieved statically with 1 A motor current during HF phase. The maximum joint rotation speed in HS was 252 deg/s with approximately 228.3 deg/s average speed. The output torque during the transition was about 270 mNm with 0.5 A motor current. Table 4.8 lists the performance calculated from both experiments. The torque magnification rates were calculated from the torque magnification ratio M_τ divided by the total time delay A+B.

The result suggested that the mechanism had a significant increase in efficiency when

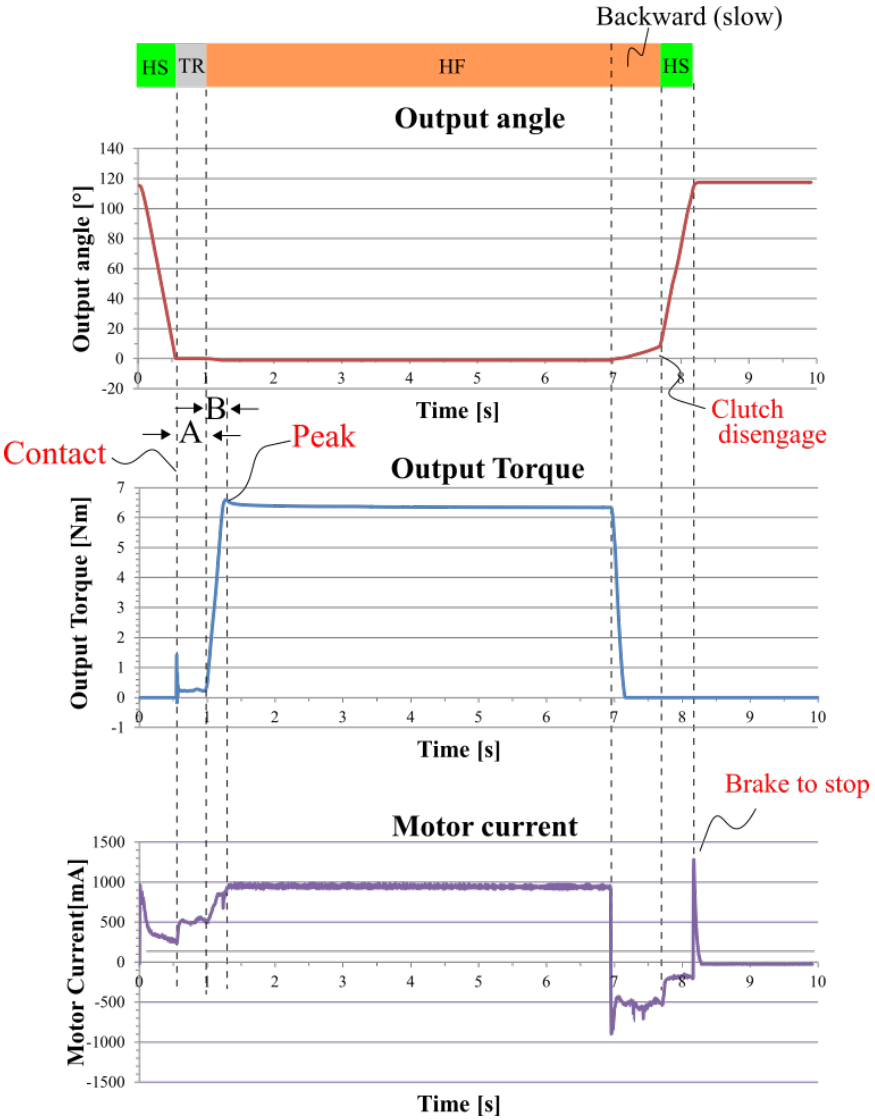

Figure 4-38: Result of the link experiment after sampling rate readjustment (1 A)

subject to a higher input current limit. This is because the friction and the torque limiter are constant while the input torque increases. Especially in this experiment, the link was stalled against the force sensor, and there were no moving components in the gear trains. Therefore, the frictional loss should be minimal in this condition. With the stall current limit of 1 A, which is the maximum current that motor can endure in stalling, the output torque was as high as 6.4 Nm. This was higher than the designed maximum output torque of 4 Nm. Although the gear did not break down in this experiment, the developed joint should not be used to supply this much of the output torque even though the motor can

Table 4.8: Performance of the joint in the link experiment

Performance parameter	Variable	Current limit		Unit
		0.7 A	1 A	
Max rotation speed in HS	ω_{HS}	252	252	deg/s
Average rotation speed in HS	ω_{HS}	221.5	228.3	deg/s
Max static output torque in HF	τ_{out}	3	6.4	Nm
Torque magnification ratio HF/HS	M_τ	8.3	11.9	times
Change in reduction ratio HF/HS	R_{HF}/R_{HS}	22.1	22.1	-
Time delay contact-to-engage	A	0.45	0.43	s
Time delay engage-to-peak	B	0.55	0.3	s
Torque magnification rate	MR_τ	8.3	16.3	times/s
Low reduction path efficiency	η_L	0.89	0.93	-
High reduction path efficiency	η_H	0.52	0.67	-

endure the current limit.

The output link also exhibited a high compliance during the transition from HS to HF phase. The high compliance behavior was confirmed by hammering the output link during its HS phase. Fig. 4-39 shows the snapshots of the hammering experiment. The output link could be easily backdriven by the impact from the hammering load. This can reduce potential damage from a collision.

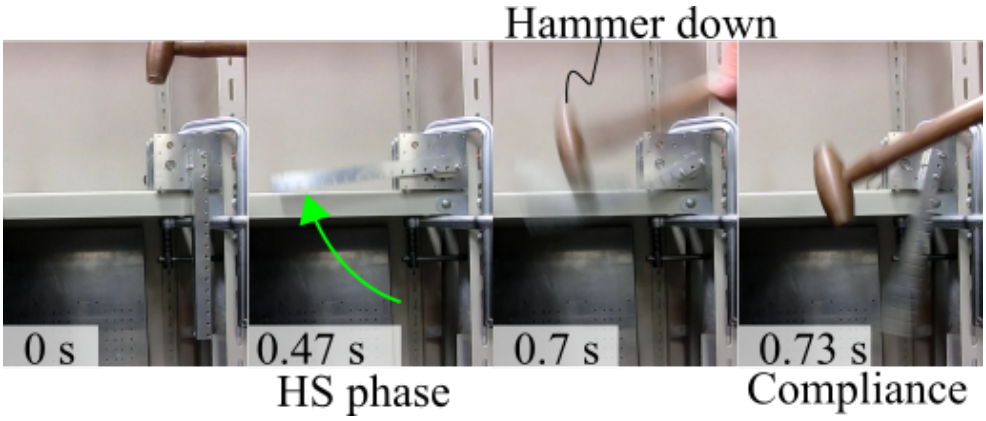

Figure 4-39: Snapshots of the joint exhibiting high compliance with hammering load)

Lifting experiment

This experiment verified the ability to exert high output torque over a long stroke. An 80 mm diameter pulley was connected to the output shaft and tied to water weights by an SUS304 ϕ0.6 mm steel cable. Fig. 4-40 shows the experiment setup. First, the cable

started from a loosened state as the low-load scenario. Then the joint was driven forward to quickly tighten the cable and lift the load up until the joint stalled. After that, the joint was driven backward and unload the weights down until the cable became loosened. The experimental loads of 0.8, 1.6, 2.4, 3.2, 4 and 4.8 Nm were used in this experiment. The current limit of all cases was set to 1 A. The forward-backward control in this experiment was done by manually pushing the control switches.

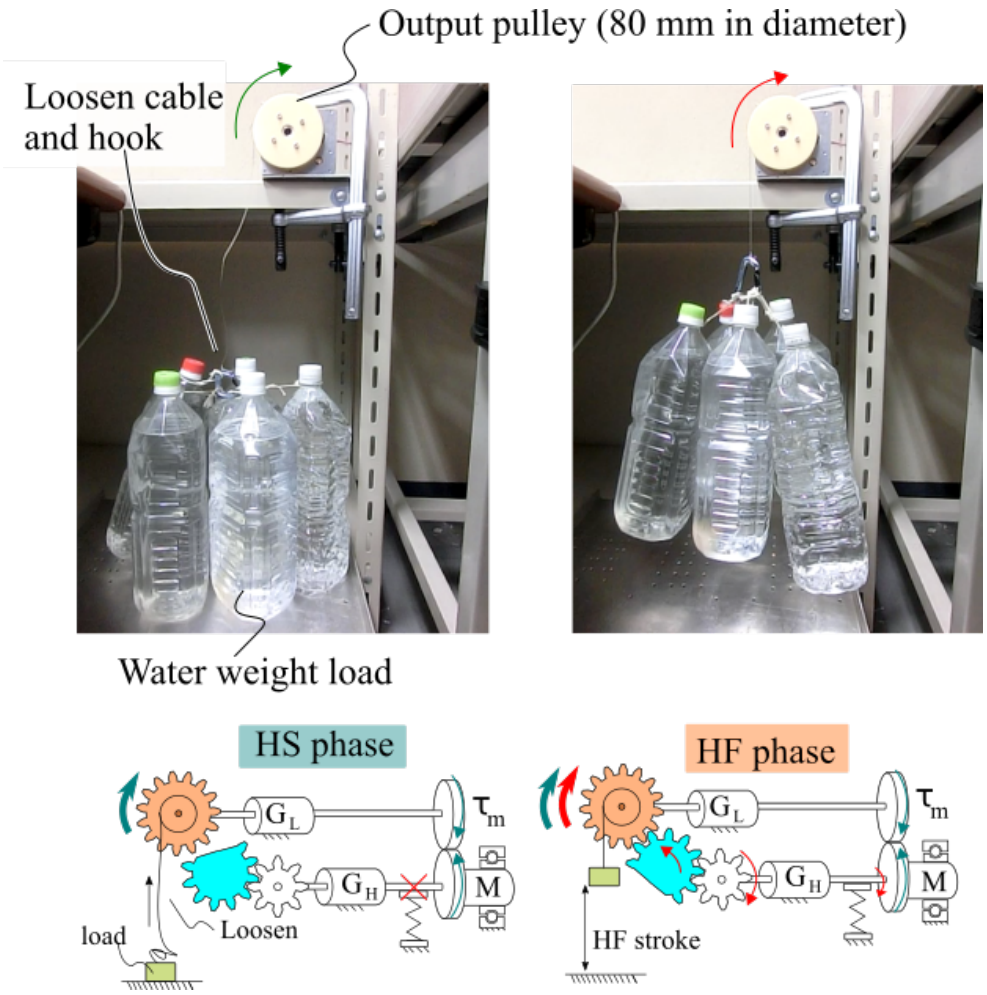

Figure 4-40: Experiment setup of the lifting experiment

Fig. 4-41 shows the experiment results with 4 Nm load. The output angle of the pulley started from zero, rotated clockwise until stalled then rotated backward to unload the water weight beyond the starting angle. It should also be noted that the effective load in this experiment was not constant for the entire loading time in the HF phase. This was because

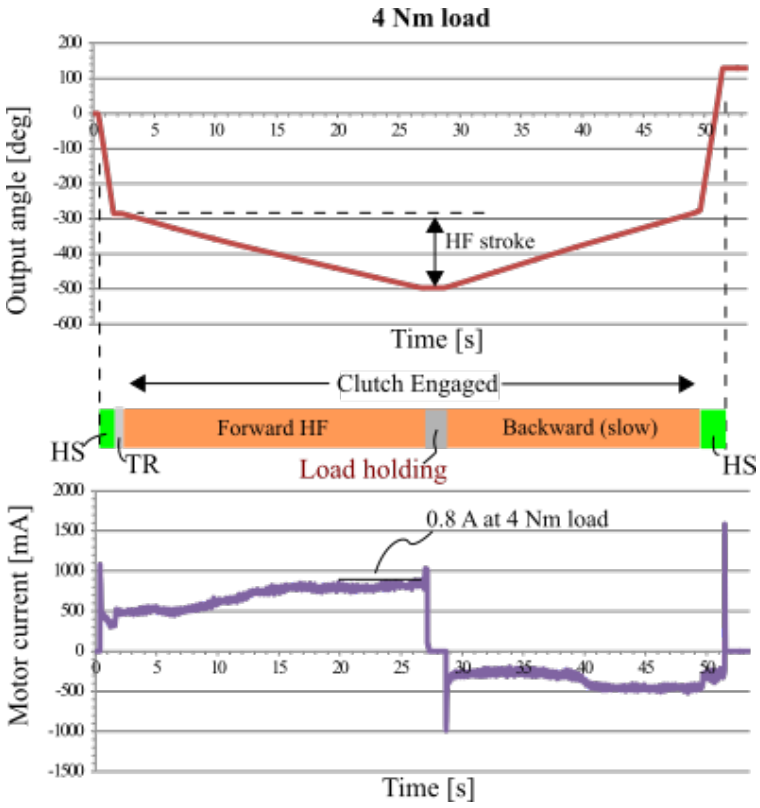

Figure 4-41: Measurement result of the lifting experiment (4 Nm load)

the bottles were connected separately to the hook, and was not lifted simultaneously. Following this idea, the load became constant after the last bottle was lifted above the ground. This can be confirmed by the motor current graph that the current increased over time after entering HF phase until it reached a nearly constant value. In the 4 Nm case, the maximum current draw was approximately 0.8 A. The HF stroke was measured from the start of the HF phase until the motor stalled. The maximum HF strokes for each case are listed in Table 4.9.

Table 4.9: Maximum HF stroke

Load [Nm]	0.8	1.6	2.4	3.2	4	4.8
HF travel range [deg]	217	218	218	212	213	Stalled

Compared to the 220 deg rotation limit from G2 slot design, small deviations from 220 deg are probably from the difference in jamming/no-jamming scenarios, and manufacturing tolerance. It was observed that during the stop period in the experiment, the motor input

voltage was cut off and the motor current is zero. Still, the load did not fall back down but instead was held by the effect of the torque limiter. This verified the offline load holding ability of the joint prototype. Additionally, the efficiency of the joint LRT is shown in Fig. 4-42. The efficiency at no-load was estimated from η_L in the link experiment for 1 A case.

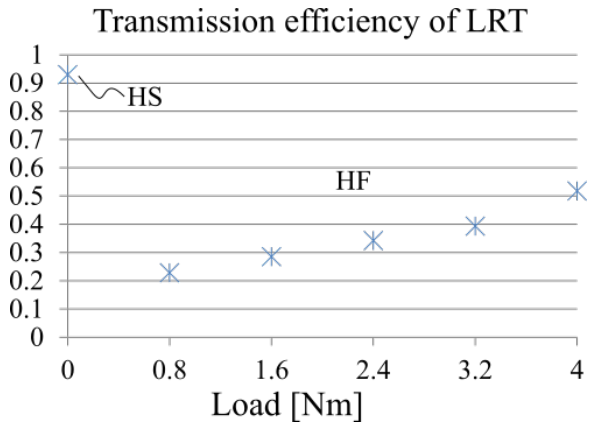

Figure 4-42: Transmission efficiency of the joint LRT

4.2.5 Performance evaluation

The developed joint prototype could exert a maximum torque of 4 Nm with more than 210 deg HF stroke. The joint lifting capacity, weight, range of motion in HF and its low load speed in HS all satisfied the design target set in Table. 4.3. For comparison, Table 4.10 lists the performance of the joint prototype with elbow prostheses used for the design reference [63, 64]. The developed joint has about two times the no-load speed with maximum lift capacity comparable to the reference elbows.

A pair of motor and gearhead was chosen to match the target maximum torque of 4 Nm and the no-load speed of 200 deg/s. A high power 20W 6V DC motor A-Max 32 (Maxon-236659) weighs 240 g and a 132:1 planetary gearhead (GP32A-166171) weighs 194 g were chosen. The maximum continuous torque of the motor results in the max output torque of $44.5 \times 132 \times 0.7 = 4.1$ Nm, (gear max efficiency of 70%). At this load, the current consumption of the motor is 3.96 A. The no-load speed of the motor results in the output no-load speed of $4880/132 = 37$ rpm, which is equivalent to 222 deg/s. The total weight of this fixed gear drive is 434 g without the frame. Compared to the developed joint LRT

Table 4.10: Performance of the joint LRT compared with available upper limb prostheses above elbow

Characteristics	Utah Arm [76, 77]	NY Electric Elbow [78]
Weight	913 g(elbow part)	550 to 620 g
Maximum active lift capacity	4.3 Nm	3.4 Nm (stall)
Maximum Current draw	No report	2 A
Range of motion	0-135 deg	0-135 deg
No load speed	112.5 deg/s	100 deg/s
Characteristics	Boston Elbow [79]	**Joint LRT**
Weight	960 g (elbow motor 605 g)	650 g (motor+gears 380 g)
Maximum lift capacity	5.9 Nm	4 Nm
Maximum Current draw	No report	0.8 A
Range of motion	0-145 deg	0-210 deg in HF (no limit in HS)
No load speed	123 deg/s	220-230 deg/s

which weighed 380 g without the frame, the LRT weighs approximately 13% less than the motor/gear pair. The current consumption at 4 Nm output torque of the fixed gear drive is $3.96/0.8 = 5$ times higher than the developed LRT (both motors are rated with 6 V driving voltage).

4.3 Discussion and Conclusion on gear-driven LRT

In this chapter, a robot joint using the LRT concept was developed. The float actuation scheme was combined with the novel gear-clutch mechanism to design a compact elbow joint that can load-sensitively and rapidly switch from HS to HF phase. A mathematical model of the actuation scheme was also discussed and used in the actual joint design.

The developed joint LRT demonstrated that by having two sets of changeable reduction ratio, the joint could produce much higher no-load speed without losing the ability to output high output torque. Compared to the design reference of existing prosthetic elbows, the developed joint LRT had about two times faster no-load speed in HS phase and a comparable maximum output torque in HF phase. The output torque could be magnified by 11.9 times within 1 s from the start of phase transition. Furthermore, when compared to a motor with a fixed reduction gearhead, the LRT weighed approximately 13% less and drew 5 times less current during maximum torque. The high compliance characteristics of the joint during high-speed motion was also confirmed experimentally.

Although feedback control of the joint prototype was not implemented, position control and force control of the joint should be possible if the state of LRT is known whether it is in HS or HF phase. This is possible by incorporating a position sensor between G2 and the tiltable link to check the gear-clutch engagement state. This idea can be used in combination with monitoring the motor current to check if the motor torque exceeds the switching threshold. The output torque of the joint can then be controlled by controlling the motor current. On the other hand, position control of the output link could be achieved by a feedback loop with a rotary encoder at the output link.

Chapter 5

Research conclusion and future work

This research proposed a load-sensitive rapidly switchable transmission (LRT) for robot joints that need high output torque and high speed. The thesis is structured into five chapters, including this chapter.

Chapter 1: Introduction This chapter introduced the need for variable transmission of high-performance robot joints that use electric motors. Examples of tasks that benefit from a change in reduction ratio were given. Commonly used actuation methods such as cable drive and gear/link drive with robot hands, arms or leg joints were discussed. The importance of compliance in robot joints was addressed with some literature reviews on methods that achieve such compliance. Then, advantages and limitations on existing variable transmissions were discussed and categorized as CVT and RT types, active and load-sensitive. CVT is praised for its many usable reduction ratios, but is rather slow in reaching the final high reduction ratio. This results in a slow change of output force. On the other hand, RT can rapidly change its reduction ratio and is able to quickly exert a high output force once the reduction is changed. Therefore, RT is more suitable for simple applications such as power grasping and load lifting. However, most of the existing RT needed active control over the reduction change and thus require two sets of controllers and additional load-sensing equipment. As far as was concerned, a load-sensitive RT that can be driven by a single actuator with compliance characteristic had yet to be developed. Therefore indicating a need for LRT and thus the objective of this study.

Chapter 2: Load-sensitive Rapidly-switchable Transmission (LRT) This chapter introduced the concept of LRT and its actuation scheme. Parallel actuation with differential and clutch mechanism was used to load-sensitively switch the reduction ratio with a single actuator. A mathematical model of the LRT was proposed to describe the effective reduction ratio and output force in each working phase. The stiffness profile of the LRT was also analyzed and demonstrated a high compliance when the transmission entered phase transition, due to the backdrive torque being higher than a preset threshold. The idea of using this characteristic for safety during high-speed motion was discussed along with design considerations of the proposed LRT concept. In addition, trade offs between phase change time and safety compliance range, and between threshold torque and output torque were also addressed with equations. Using the proposed concept, two types of LRT were developed in the subsequent chapters: Cable-driven LRT for robot finger joints, and gear-driven type for in-joint actuation such as elbow joints.

Chapter 3: Cable-driven LRT Prototypes of cable-driven LRT were developed using pulley system as the differential unit. A preliminary design of a split-pulley clutch was introduced and confirmed for its ability to change the reduction ratio load-sensitively. However, there were some issues regarding cable damage and slippage. The second design of cable-driven LRT using a rack-tilting mechanism was then introduced to solve the previous issues of the split pulley type. A 2-DOF underactuated robot finger and an LRT prototype unit were developed. The finger/LRT pair was able to produce fast pinching speed and high fingertip force using the proposed LRT concept. The finger exhibited an average joint speed of 372 deg/s during HS phase and an output fingertip force of 24.6 N during HF phase. The LRT prototype could magnify the output force by 10 times in 0.7 s after the contact was made. The developed LRT prototype weighed 156 g with frame and was compact enough to fit in human palm. Performance evaluation showed that the developed finger/LRT pair could provide 50% faster speed and stronger fingertip force with 4 times less current draw when compared to a prosthetic finger with a fixed reduction actuator. Also, the force magnification rate was higher than some cable-driven CVTs. Furthermore, the finger/LRT showed desirable compliant behavior during the impact drop experiment.

In contrast to CVTs whose stiffness continuously increases during impacts. The constant low stiffness of LRT during the transition has a potential to improve the impact tolerance.

Chapter 4: Gear-driven LRT This chapter introduced a novel gear-clutch for LRT that exert high output torque over a longer stroke such in elbow joints. Mathematical model and design criteria of the gear-clutch mechanism were proposed and verified with experiments. A robot elbow joint LRT using the novel clutch was designed to demonstrate the LRT concept with prosthetic elbows as references. The joint prototype was able to achieve high no-load speed and exert high output torque using a small DC geared motor. The joint speed during HS phase was 230 deg/s. The maximum torque was 4 Nm in HF phase. The output torque could be magnified by 11.9 times within 1 s from the start of the phase transition. In addition, high compliance characteristics of the joint were demonstrated with a hammering load to the output link. Performance evaluations showed that the joint could operate with two times faster no-load speed than the reference elbow joints with comparable maximum lift capacity. When compared to a fixed reduction motor and gear pair, the developed joint LRT was approximately 13% lighter and consumed 5 times less current during maximum load. The joint weighed 650 g and has an offline load holding ability that could help reduce joint power consumption.

The two types of LRT prototypes have their own merits and limitations. The cable-driven LRT is light weight and can be placed away from the end effector for weight distribution. Long stroke of the rack gives a possibility for underactuation of multiple robot fingers. Therefore, the cable-driven LRT is suitable to applications such as grippers, cable-driven underactuated hands and also prosthetic applications. However, the presence of friction losses might limit the maximum reduction ratio available for the LRT. Since the cable only transmit tension, the joint needs an additional actuation unit or preloaded springs to release its grasp, which might not be practical in case of elbow joints. On the other hand, gear-driven LRT offers a more flexible choice for reduction ratio between HS and HF phase by simply using commercial gearboxes. In addition, the use of the novel gear-clutch gives the design compactness when compared to the rack-clutch in cable-driven LRT. Also, as

the gear can transmit torque in both directions, there is no need for preloaded springs. This means gear-driven LRT has higher expected output torque than cable-driven LRT, given the same reduction in HF phase. However, the use of gears inevitably results in a heavier transmission than cable-driven LRT. With these considerations, the gear-LRT is more suitable for applications that require higher output torque and have more forgiving constraint for the weight of the unit, such as in elbow, knee joints or industrial machines, of which include punching and shearing machines. Power-assist systems is also a possible application given the one-way characteristic of the gear-clutch.

A variant of the LRT concept is also useful for applications that need to change the output direction according to load sensitivity. For example, an elevator door could be designed to load-sensitively reverse its direction when the safety edge of the door is obstructed. Similarly, it can be used in tasks with reciprocating direction reversal such as repeatedly stapling or punching holes through documents with arbitrary thickness. In these cases, the use of LRT would result in simpler control, since the motor does not need to change its rotation direction.

Future work will involve the development of a control strategy for the nonlinear behavior of the LRT. As the reduction ratio of the LRT changes according to the clutch state, controls of the LRT should be possible if the state of the clutch is known. As discussed in Chapter 4, a position encoder could be added to extract the state information from the clutch of the LRT. Fig. 5-1 demonstrates an idea for the clutch state sensing. Because the position of possible jamming is known by the design, if the G2 angle γ were to pass the jamming point, the LRT would be in HF phase. Similarly, the state of the transmission could be done by monitoring the rack carrier unit position in the cable-driven LRT. In addition, the motor current can also be monitored to determine whether the LRT is in HS or HF phase.

Another future work will investigate the controllability of the LRT if the load is near the switching threshold. Theoretically, even if the reduction ratio abruptly switches back and forth between HS and HF phase, the output torque and speed cannot be changed instantaneously due to the mechanism compliance. Therefore the LRT should be controllable to some extent even at near-threshold load. For the gear-driven LRT with gear-clutch, the

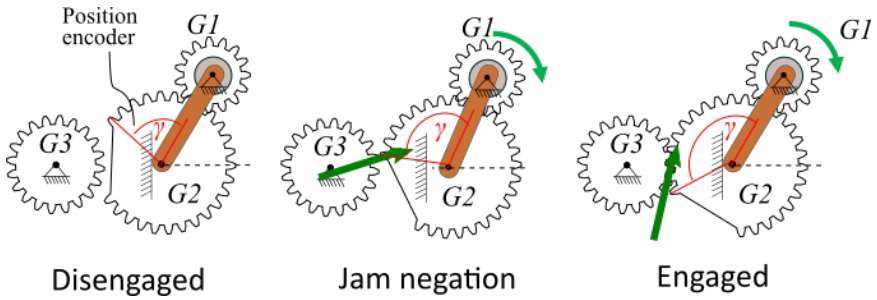

Figure 5-1: Clutch state sensing by a position sensor between G2 and tiltable link

one-way characteristic allows high speed output even in a clutch engaged state; this may cause a jump in output speed in the forward direction. However, since the output direction does not change by phase switching, the problem of chattering may be suppressed if the position control scheme has no overly large overshoot. Force control of the output link should be possible by controlling the motor current. Still, stability and robustness of the control method need to be investigated for the LRT to be used in precise robotic application.

Finally, a limitation on the proposed clutches of the LRTs concerns their ability to exert high output torque/force in only one direction. In the future, a bi-directional clutch design will be investigated for tasks such as push and pull with robot arms.

Bibliography

[1] Vanderborght B, Albu-Schaeffer A, Bicchi A, Burdet E, Caldwell D, Carloni R, Catalano M, Eiberger O, Friedl W, Ganesh G, Garabini M, Grebenstein M, Grioli G, Haddadin S, Hoppner H, Jafari A, Laffranchi M, Lefeber D, Petit F, Stramigioli S, Tsagarakis N, Damme MV, Ham RV, Visser L, Wolf S. Variable impedance actuators: A review. Robotics and Autonomous Systems. 2013;61(12):1601 – 1614. Available from: http://www.sciencedirect.com/science/article/pii/S0921889013001188.

[2] Ahmed M, Kalaykov I. Semi-active compliant robot enabling collision safety for human robot interaction. In: Mechatronics and automation (icma), 2010 international conference on. RiverCentre, Saint Paul, Minnesota, USA. 2010 Aug. p. 1932–1937.

[3] Zinn M, Khatib O, Roth B, Salisbury J. Playing it safe [human-friendly robots]. Robotics Automation Magazine, IEEE. 2004 June;11(2):12–21.

[4] Pylatiuk C, Schulz S, Döderlein L. Results of an internet survey of myoelectric prosthetic hand users. Prosthetics and Orthotics International. 2007;31(4):362–370.

[5] Jacobsen S, Iversen E, Knutti D, Johnson R, Biggers K. Design of the utahh4.i.t. dextrous hand. In: The 1986 ieee international conference on robotics and automation. 1986. p. 1520–1532.

[6] Kurita Y, Ono Y, Ikeda A, Ogasawara T. Naist hand 2: Human-sized anthropomorphic robot hand with detachable mechanism at the wrist. In: The 2009 ieee/rsj international conference on intelligent robots and systems. 2009. p. 2271–2276.

[7] Mao Y, Agrawal SK. Design of a cable-driven arm exoskeleton (carex) for neural rehabilitation. IEEE Transactions on Robotics. 2012 Aug;28(4):922–931.

[8] Kragten GA, Herder JL. The ability of underactuated hands to grasp and hold objects. Mechanism and Machine Theory. 2010;45(3):408 – 425. Available from: http://www.sciencedirect.com/science/article/pii/S0094114X09001797.

[9] Jin X, Cui X, Agrawal SK. Design of a cable-driven active leg exoskeleton (c-alex) and gait training experiments with human subjects. In: 2015 ieee international conference on robotics and automation (icra). 2015 May. p. 5578–5583.

[10] Butterfass J, Grebenstein M, Liu H, Hirzinger G. Next generation of a dextrous robot hand. In: The 2001 ieee international conference on robotics and automation. Vol. 15. 2001. p. pp.105–110.

[11] Technology B. Barrett hand. Last visited 2017. Available from: http://www.barrett.com/products-hand.htm.

[12] Ramos AM, Gravagne IA, Walker ID. Goldfinger: A non-anthropomorphic, dextrous robot hand. In: The 1999 ieee international conference on robotics and automation. 1999. p. 913–919.

[13] Contreras DA, Ramírez-García A, Gallegos FJ, Bazán I. Proposal of a mechanism for an electrical elbow prosthesis. In: 2014 11th international conference on electrical engineering, computing science and automatic control (cce). 2014 Sept. p. 1–5.

[14] Grebenstein M, Chalon M, Friedl W, Haddadin S, Wimböck T, Hirzinger G, Siegwart R. The hand of the dlr hand arm system: Designed for interaction. The International Journal of Robotics Research. 2012;31(13):1531–1555. http://dx.doi.org/10.1177/0278364912459209. Available from: http://dx.doi.org/10.1177/0278364912459209.

[15] Carrozza M, Suppo C, Sebastiani F, Massa B, Vecchi F, Lazzarini R, Cutkosky M, Dario P. The spring hand: Development of a self-adaptive prosthesis for restoring natural grasping. Autonomous Robots. 2004;16(2):125–141. Available from: http://dx.doi.org/10.1023/B%3AAURO.0000016863.48502.98.

[16] Odhner LU, Jentoft LP, Claffee MR, Corson N, Tenzer Y, Ma RR, Buehler M, Kohout R, Howe RD, Dollar AM. A compliant, underactuated hand for robust manipulation. The International Journal of Robotics Research. 2014;33(5):736–752. http://ijr.sagepub.com/cgi/reprint/33/5/736. Available from: http://ijr.sagepub.com/cgi/content/abstract/33/5/736.

[17] Aukes D, Kim S, Garcia P, Edsinger A, Cutkosky M. Selectively compliant underactuated hand for mobile manipulation. In: Robotics and automation (icra), 2012 ieee international conference on. 2012 May. p. 2824–2829.

[18] Bicchi A, Tonietti G. Fast and "soft-arm" tactics [robot arm design]. Robotics Automation Magazine, IEEE. 2004 June;11(2):22–33.

[19] Ham R, Sugar T, Vanderborght B, Hollander K, Lefeber D. Compliant actuator designs. Robotics Automation Magazine, IEEE. 2009 September;16(3):81–94.

[20] Kang BS, Kothera C, Woods B, Wereley N. Dynamic modeling of mckibben pneumatic artificial muscles for antagonistic actuation. In: Robotics and automation, 2009. icra '09. ieee international conference on. 2009 May. p. 182–187.

[21] Tonietti G, Schiavi R, Bicchi A. Design and control of a variable stiffness actuator for safe and fast physical human/robot interaction. In: Robotics and automation, 2005.

icra 2005. proceedings of the 2005 ieee international conference on. Barcelona, Spain. 2005 April. p. 526–531.

[22] Jacobsen S, Ko H, Iversen E, Davis C. Antagonistic control of a tendon driven manipulator. In: Robotics and automation, 1989. proceedings., 1989 ieee international conference on. Scottsdale, Arizona. 1989 May. p. 1334–1339 vol.3.

[23] Zhou X, Jun Sk, Krovi V. A Cable Based Active Variable Stiffness Module With Decoupled Tension. Journal of Mechanisms and Robotics. 2015 Feb;7(1):011005–011005. Available from: http://dx.doi.org/10.1115/1.4029308.

[24] Ahmed MR. Compliance control of robot manipulator for safe physical human robot interaction. [Ph.D. thesis]. Örebro University, School of Science and Technology. 2011.

[25] Morrell JB, Salisbury JK. Parallel-coupled micro-macro actuators. The International Journal of Robotics Research. 1998;17(7):773–791. http://ijr.sagepub.com/content/17/7/773.full.pdf+html. Available from: http://ijr.sagepub.com/content/17/7/773.abstract.

[26] Zinn M, Roth B, Khatib O, Salisbury JK. A new actuation approach for human friendly robot design. The International Journal of Robotics Research. 2004;23(4-5):379–398. http://ijr.sagepub.com/content/23/4-5/379.full.pdf+html. Available from: http://ijr.sagepub.com/content/23/4-5/379.abstract.

[27] Pratt G, Williamson M. Series elastic actuators. In: Intelligent robots and systems 95. 'human robot interaction and cooperative robots', proceedings. 1995 ieee/rsj international conference on. Vol. 1. Pittsburgh, Pennsylvania USA. 1995 Aug. p. 399–406 vol.1.

[28] Yamano I, Maeno T. Five-fingered robot hand using ultrasonic motors and elastic elements. In: Robotics and automation, 2005. icra 2005. proceedings of the 2005 ieee international conference on. Barcelona, Spain. 2005 April. p. 2673–2678.

[29] Yeo S, Yang G, Lim W. Design and analysis of cable-driven manipulators with variable stiffness. Mechanism and Machine Theory. 2013;69:230 – 244. Available from: http://www.sciencedirect.com/science/article/pii/S0094114X13001249.

[30] Yamada H. A proposal of the crank continuously variable transmission driven by 2 links. In: The 28th annual conference of the robotics society of japan. 2010.

[31] Tahara K, Iwasa S, Naba S, Yamamoto M. High-backdrivable parallel-link manipulator with continuously variable transmission. In: 2011 ieee/rsj international conference on intelligent robots and systems. 2011 Sept. p. 1843–1848.

[32] Takaki T, Omata T. 100g-100n finger joint with load-sensitive continuously variable transmission. In: The 2006 ieee international conference on robotics and automation. 2006. p. 976–981.

[33] Matsushita K, Shikanai S, Yokoi H. Development of drum cvt for a wire-driven robot hand. In: Intelligent robots and systems, 2009. iros 2009. ieee/rsj international conference on. St.Louis, USA. 2009 Oct. p. 2251–2256.

[34] Spanjer S, Balasubramanian R, Dollar A, Herder J. Underactuated gripper that is able to convert from precision to power grasp by a variable transmission ratio. In: Dai JS, Zoppi M, Kong X, editors. Advances in reconfigurable mechanisms and robots i. Springer London. 2012. p. 669–679. Available from: http://dx.doi.org/10.1007/978-1-4471-4141-9_60.

[35] Shin YJ, Lee HJ, Kim KS, Kim S. A robot finger design using a dual-mode twisting mechanism to achieve high-speed motion and large grasping force. Robotics, IEEE Transactions on. 2012 Dec;28(6):1398–1405.

[36] Würtz T, May C, Holz B, Natale C, Palli G, Melchiorri C. The twisted string actuation system: Modeling and control. In: Advanced intelligent mechatronics (aim), 2010 ieee/asme international conference on. 2010 July. p. 1215–1220.

[37] Shin YJ, Rew KH, Kim KS, Kim S. Development of anthropomorphic robot hand with dual-mode twisting actuation and electromagnetic joint locking mechanism. In: The 2013 ieee international conference on robotics and automation. 2013. p. 2759–2764.

[38] Takayama T, Chiba Y, Omata T. Tokyo-tech 100 n hand : Three-fingered eight-dof hand with a force-magnification mechanism. In: Robotics and automation, 2009. icra '09. ieee international conference on. 2009 May. p. 593–598.

[39] Takayama T, Yamana T, Omata T. Three-fingered eight-dof hand that exerts 100-n grasping force with force-magnification drive. Mechatronics, IEEE/ASME Transactions on. 2012 April;17(2):218–227.

[40] Takayama T, Chiba G, Omata T. Large grasp force hand with high compliance during high speed phase (in japanese). TRANSACTIONS OF THE JAPAN SOCIETY OF MECHANICAL ENGINEERS Series C. 2013;79(802):1893–1903.

[41] Takaki T, Omata T. Grasp force magnifying mechanism for parallel jaw grippers. In: Proceedings 2007 ieee international conference on robotics and automation. 2007 April. p. 199–204.

[42] Teranishi Y, Hirose S. Development of a load-sensitive dual states transmission with a twoway clutch (in japanese). In: Proceedings of jsme conference on robotics and mechatronics. 2007 May. p. 2A1–J05(1)–2A1–J05(2).

[43] Guarnieri M, Debenest R, Inoh T, Fukushima E, Hirose S. Development of helios vii: an arm-equipped tracked vehicle for search and rescue operations. In: 2004 ieee/rsj international conference on intelligent robots and systems (iros) (ieee cat. no.04ch37566). Vol. 1. 2004 Sept. p. 39–45 vol.1.

[44] Yamada Y, Hirasawa Y, Huang SY, Umetani Y. Fail-safe human/robot contact in the safety space. In: Robot and human communication, 1996., 5th ieee international workshop on. 1996 Nov. p. 59–64.

[45] Wyeth G. Demonstrating the safety and performance of a velocity sourced series elastic actuator. In: 2008 ieee international conference on robotics and automation. 2008 May. p. 3642–3647.

[46] Attaway SW. The mechanics of friction in rope rescue. In: International technical rescue symposium (itrs 99). 1999.

[47] Morales M. Influence of tendon-pulley friction on an index finger model. Unpublished master thesis, Swiss Federal Institute of Technology Zurich. 2011. Master thesis.

[48] In H, Kang S, Cho KJ. Capstan brake: Passive brake for tendon-driven mechanism. In: Intelligent robots and systems (iros), 2012 ieee/rsj international conference on. Vilamoura, Algarve, Portugal. 2012 Oct. p. 2301–2306.

[49] Maitra GM. Handbook of gear design 2nd edition. New Delhi: Tata McGraw Hill Education Private Limited. 2011.

[50] Hirose S, Umetani Y. The development of soft gripper for the versatile robot hand. Mechanism and Machine Theory. 1978;13(3):351 – 359. Available from: http://www.sciencedirect.com/science/article/pii/0094114X78900599.

[51] Rakić M. Multifingered robot hand with selfadaptability. Robotics and Computer-Integrated Manufacturing. 1989;5(2–3):269 – 276. Available from: http://www.sciencedirect.com/science/article/pii/0736584589900744.

[52] Crisman J, Kanojia C, Zeid I. Graspar: a flexible, easily controllable robotic hand. Robotics Automation Magazine, IEEE. 1996 Jun;3(2):32–38.

[53] Laliberte T, Gosselin CM. Simulation and design of underactuated mechanical hands. Mechanism and Machine Theory. 1998;33(1–2):39 – 57. Available from: http://www.sciencedirect.com/science/article/pii/S0094114X97000207.

[54] Gosselin C, Pelletier F, Laliberte T. An anthropomorphic underactuated robotic hand with 15 dofs and a single actuator. In: Robotics and automation, 2008. icra 2008. ieee international conference on. Pasadena, CA, USA. 2008 May. p. 749–754.

[55] Dollar A, Jentoft L, Gao J, Howe R. Contact sensing and grasping performance of compliant hands. Autonomous Robots. 2010;28(1):65–75. Available from: http://dx.doi.org/10.1007/s10514-009-9144-9.

[56] Ozawa R, Hashirii K, Kobayashi H. Design and control of underactuated tendon-driven mechanisms. In: Robotics and automation, 2009. icra '09. ieee international conference on. Kobe, Japan. 2009 May. p. 1522–1527.

[57] Zhang W, Chen Q, Sun Z, Zhao D. Passive adaptive grasp multi-fingered humanoid robot hand with high under-actuated function. In: Robotics and automation, 2004. proceedings. icra '04. 2004 ieee international conference on. Vol. 3. New Orleans, LA. 2004 April. p. 2216–2221 Vol.3.

[58] Dalley SA, Wiste TE, Withrow TJ, Goldfarb M. Design of a multifunctional anthropomorphic prosthetic hand with extrinsic actuation. IEEE/ASME Transactions on Mechatronics. 2009 Dec;14(6):699–706.

[59] Laliberté T, Gosselin CM. Simulation and design of underactuated mechanical hands. Mechanism and Machine Theory. 1998;33(1):39 – 57. Available from: http://www.sciencedirect.com/science/article/pii/S0094114X97000207.

[60] Massa B, Roccella S, Carrozza MC, Dario P. Design and development of an underactuated prosthetic hand. In: Robotics and automation, 2002. proceedings. icra '02. ieee international conference on. Vol. 4. 2002. p. 3374–3379 vol.4.

[61] Wu L, Carbone G, Ceccarelli M. Designing an underactuated mechanism for a 1 active {DOF} finger operation. Mechanism and Machine Theory. 2009;44(2):336 – 348. Available from: http://www.sciencedirect.com/science/article/pii/S0094114X08000633.

[62] Rao J, Dukkipati R. Mechanism and machine theory. New Age International. 1992.

[63] Irfan H, Adnan M, Javaid I, Umar SK. Design of high torque elbow joint for above elbow prosthesis. International Science Index, Mechanical and Mechatronic Engineering. 2011;5(11):2118–2121.

[64] Toledo C, Leija L, Munoz R, Vera A, Ramirez A. Upper limb prostheses for amputations above elbow: A review. In: 2009 pan american health care exchanges. 2009 March. p. 104–108.

[65] Weir RF, Sensinger JW. Design of artificial arms and hands for prosthetic applications. Standard handbook of biomedical engineering & design. 2003;2.

[66] Toogood R. Creo simulate 3.0 tutorial:. SDC Publications. 2015.

[67] Flaherty JE. Course note lecture 8: Adaptive finite element technique. Last visited 2017. Available from: http://www.cs.rpi.edu/~flaherje/pdf/fea8.pdf.

[68] MatWeb. Material property data of aluminum 5052-o. 2017. Available from: http://matweb.com/search/DataSheet.aspx?MatGUID=b3430ccca1334449b0d59cde9f977b57&ckck=1.

[69] drive H. Miniature gearheads catalog. Last visited 2017. Available from: http://www.harmonicdrive.net/_hd/content/documents/CSF_mini.pdf.

[70] Pololu. Pololu dual vnh5019 motor driver shield. Last updated 2017. Available from: https://www.pololu.com/docs/pdf/0J49/dual_vnh5019_motor_driver_shield.pdf.

[71] Arduino. Arduino uno r.3. Last updated 2017. Available from: https://www.arduino.cc/en/Main/ArduinoBoardUno.

[72] COPAL. Acs714 current sensor carrier. Last updated 2017. Available from: https://www.nidec-copal-electronics.com/e/catalog/rotary-encoder/re12d.pdf.

[73] Pololu. Re12d optical encoder. Last updated 2017. Available from: https://www.pololu.com/product/1185.

[74] AIKOH. Operation manual: Cpu gage rx series. Last updated 2014. http://www.aikoh.co.jp/products/load/handy/pdf/rx_manual_en.pdf.

[75] Electronics K. Pmc18-5 manual. Last updated 2009. Available from: http://www.kikusui.co.jp/en/man/?MODEL=PMC&skip=10.

[76] control M. The utah arm. 2009. Available from: http://www.utaharm.com/index.php.

[77] Sears HH, Andrew JT, Jacobsen SC. Experience with the utah arm, hand, and terminal device. New York, NY: Springer New York. 1989. p. 194–210. Available from: http://dx.doi.org/10.1007/978-1-4612-3530-9_18.

[78] Prout W. The new york electric elbow, the new york prehension actuator, and the nu-va synergetic prehensor. New York, NY: Springer New York. 1989. p. 221–226. Available from: http://dx.doi.org/10.1007/978-1-4612-3530-9_20.

[79] LTI. The boston elbow. 1984. Available from: http://ota.fas.org/reports/8405.pdf.

Research Achievements

Published paper

- Phlernjai Maroay, Takayama Toshio, Toru Omata, "Passively switched cable-driven transmission for high-speed/high-force robot finger", Advanced Robotics, Vol.30, No.24. 1559-1570, 2016

- Phlernjai Maroay, Takayama Toshio, "Jam-Free Gear-Clutch Mechanism for Load-Sensitive Step Transmission in Robotic Joint", ROBOMECH Journal, Vol. 4, No.1, 2017

International conference

- "Development of Cable-Driven Force Magnification Mechanism", The 2nd ASIAN-IFToMM, ID. 70, 2012

Domestic conference

- "Cable-Driven Force Magnification Mechanism with Back-drivability", The 30th Annual Conference of the RSJ, No. 4B3-3 2012

- "Load Sensitive Cable-Driven Force Magnification Mechanism", The 31th Annual Conference of the RSJ, No. 1L2-02, 2013

- "Robot finger with load-sensitive force magnification mechanism using rack-gear tilting mechanism", ROBOMECH Conference, No. 3P2-R04, 2014

Appendix A

Damper for cable-driven LRT

If the cable-driven LRT is to be used with underactuation of multiple fingers or simply large finger joints, the clutch separation distance d_{sep} has to be large to provide sufficient compliance range. Alternatively, d_{sep} can potentially be reduced by using a damper to stop the abrupt movement of the rack carrier unit during a collision. Fig. A-1 shows an idea of adding a damper to the developed mechanism to reduce the transmission size.

Fig. A-2 shows how the damper works. The damper has a piston-cylinder design. The piston cap is a cup-shaped piston and is made of an elastic material. The piston cap diameter is slightly smaller than the inner diameter of the cylinder. The damper is filled with an incompressible fluid (water in this case). Slow speed movement of the piston allows the fluid to flow through the gap and does not resist the movement of the damper rod. However, a swift movement of the rod caused by an impact causes the piston cup to expand and closes the gap. Since the fluid is incompressible, the increase in fluid pressure pushes the cup rim against the cylinder inner wall and stops the rod movement. Fig. A-3 shows the developed test model of the damper and various sizes of the piston cap. The piston cap was made of silicone. The silicone used in casting was Momentive TSE3466. The outer diameter of the cap was designed to be a little smaller than the inner diameter of the cylinder, which is 5.5 mm.

To verify the damper concept, drop experiments were conducted for various sizes of the piston cap. Fig. A-4 shows the experiment setup. The developed damper was assembled with a spring. The spring stiffness determines the equilibrium displacement of the rod if

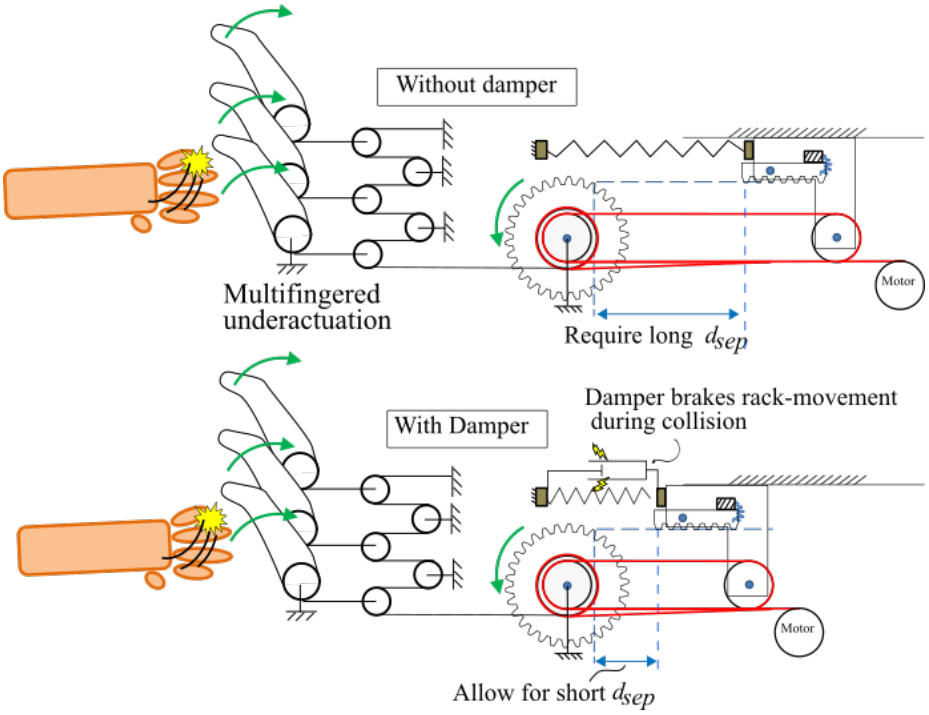

Figure A-1: Idea of using a damper to reduce minimum d_{sep} requirement

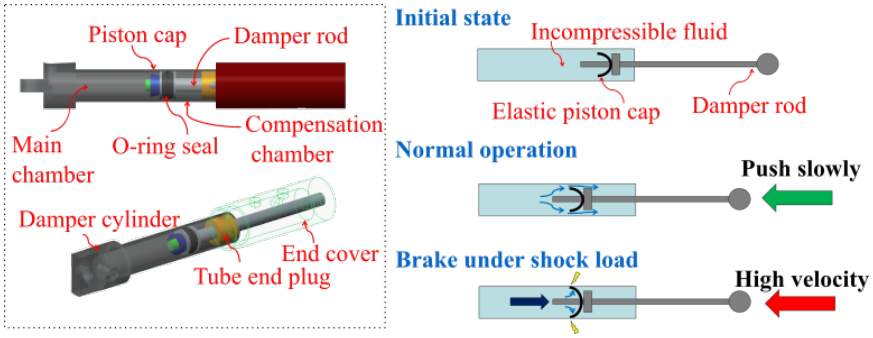

Figure A-2: The working concept of the damper.

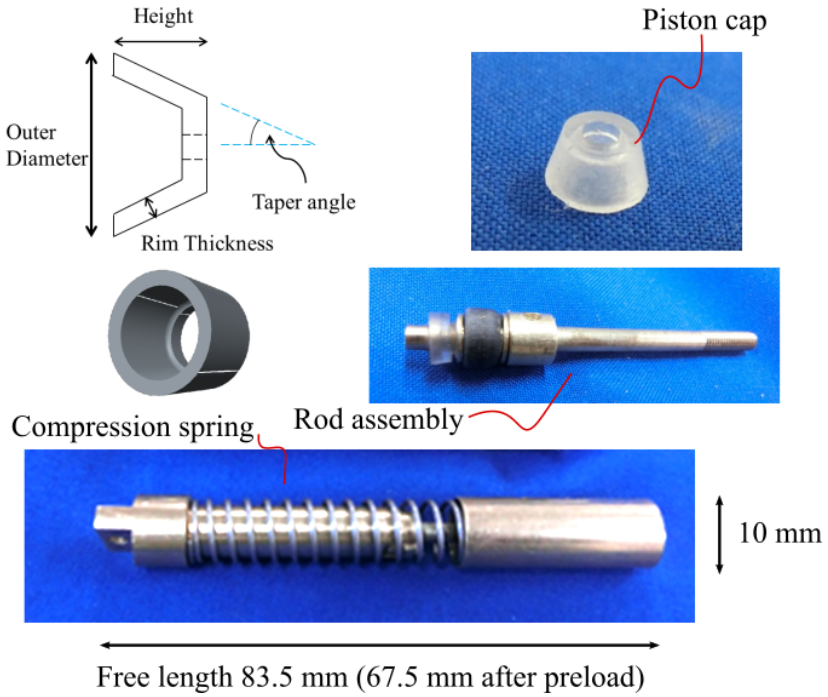

Figure A-3: The test model of the damper

Table A.1: Piston cap specifications

Outer diameter	Rim thickness	Base thickness	Taper angle	Cap height
5.4 mm	1 mm	1 mm	5 deg	2 mm

the weight is statically load onto the damper-spring assembly. In this drop experiment, a spring with $k_s = 0.442$ N/mm and preload of 16 mm were used. The drop weights had the mass of 1.05 kg. In the experiment, the drop height of 25 mm was chosen because it has the approximately the same impact momentum as that in the drop experiment of the cable-driven LRT (0.5 kg with 1.5 m/s impact speed).

Detailed analysis of the damper would require simulations of complex pressure profile in shock loading. Since the damper was proposed as an optional part and not the main concern of this research, its mathematical model and analysis were not developed. Instead, trial and error method was used in the design. Specifications of the piston cap can be found in Table. A.1.

Fig.A-5 shows the drop experiment result. The graph has three types of data: raw displacement data measured by the laser sensor, the moving average of the data (n=4), and linear regression of the shock movement. The dashed line shows the static equilibrium point

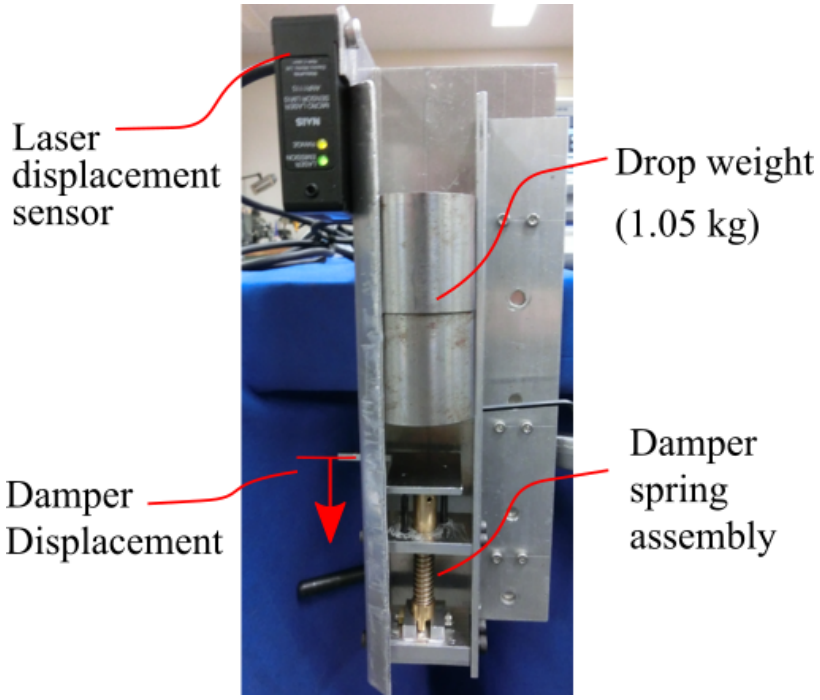

Figure A-4: Drop experiment setup of the damper-spring assembly

consider only the spring stiffness when loaded statically with the weight ($((1.05)(10) - 7.072)/0.442 = 7.76$). The braking distance is the displacement of the damper rod caused by the impact until the brake is in effect. The slopes mentioned in the results are the slope of linear regression lines (red lines); which refers to the speed of the compression. Table A.2 summarizes the experiment results at different dropping heights.

The result shows that the damper was able to stop the rod movement due to the shock load from dropping weight. Moreover, it can reduce the distance the damper supposed to move from 7.76 mm to around 4 mm. The brake condition is believed to strongly depends

Table A.2: Drop experiment results at different drop height

Drop height [mm]	Calculated impact momentum [kg.m/s]	Brake distance [mm]	Compression speed [mm/s]
5	0.33	1.95	21.42
10	0.47	2.15	91.67
15	0.58	2.90	30.75
20	0.66	2.55	40.12
25	0.74	3.60	42.58
30	0.81	3.40	43.67
35	0.88	4.05	50.36
40	0.94	3.80	34.8

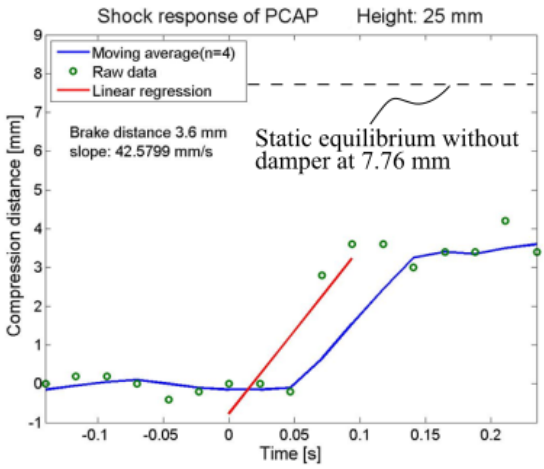

Figure A-5: Experiment result of damper at 25 mm dropping height.

on the shape of the piston cap and its relative speed with the surrounding fluid.

It can be concluded that the developed damper should be potentially useful for an LRT that needs more than 4 mm rack travel for finger retractions. For example, if a robot finger needs 10 mm rack travel in its reversal of its shock response, this damper would be able to stop the rack movement at 4 mm; transferring the tension and back drive the motor. In normal operation, if the motor pulls the rack at much lower speed then the reported shock compression speed, the rack would not be stopped by the damper, and the LRT unit should be able to provide step transmission. However, effects of friction from the sealing should be considered in actual practice.

Appendix B

One-way characteristic of the gear-clutch

The gear-clutch mechanism can provide jam-free engagement and stable meshing of G2 and G3 with the assumption of $\tau_{in} > 0$ in the forward drive. This subsection expands the concept to what would happen when G1 rotates in the opposite direction or $\tau_{in} < 0$ (Backward drive) and explains the one-way characteristic of the gear-clutch. Accompany by Fig. B-1 and Fig. B-2. Static equilibrium of the backward drive can be written as follows.

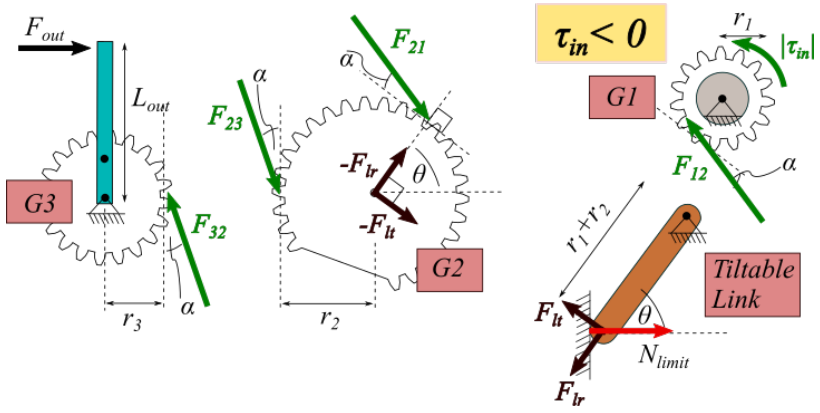

Figure B-1: Free body diagram of gear meshing (backward drive)

Backward mesh:

$$
\begin{aligned}
F_{lt} &= -F_{21}\cos\alpha - F_{23}\cos(\theta-\alpha) && \text{(B.1)}\\
F_{21} &= F_{23} && \text{(B.2)}\\
|\tau_{in}| &= F_{21} r_1 \cos\alpha && \text{(B.3)}\\
F_{lt} &= \frac{-|\tau_{in}|(\cos\alpha+\cos(\theta-\alpha))}{r_1\cos\alpha} && \text{(B.4)}
\end{aligned}
$$

For the gear-clutch that was designed to satisfy the jam-free and stable-meshing in the forward drive, Eq. 4.5 holds true ($\cos\alpha+\cos(\theta+\alpha)\geq 0$). As the pressure angle α of the gear is usually in the first quadrant, $0<\alpha<\pi/2$, Eq. B.4 can be rewritten as follows

$$
\begin{aligned}
F_{lt} &= \frac{-|\tau_{in}|}{r_1\cos\alpha}((\cos\alpha+\cos(\theta+\alpha))+(\cos(\theta-\alpha)-\cos(\theta+\alpha))) && \text{(B.5)}\\
&= \frac{-|\tau_{in}|}{r_1\cos\alpha}((\cos\alpha+\cos(\theta+\alpha))+2\sin\theta\sin\alpha) && \text{(B.6)}\\
&= \frac{-|\tau_{in}|}{r_1\cos\alpha}((..\geq 0)+(..\geq 0)) && \text{(B.7)}
\end{aligned}
$$

Therefore, $F_{lt}\leq 0$ for all $0\leq\theta\leq\pi$ in backward drive. This means that for all the θ that satisfy the stable meshing condition in the forward drive, the tiltable link will experience a counter-clockwise moment in the backward drive, resulting in an unstable meshing scenario.

Next, similar analysis is done for jamming scenario in the backward drive, the jamming angle β is now in the fourth quadrant and thus has a minus sign.

Backward jam:

$$
\begin{aligned}
\beta_{bw}=-\beta &= -\cos^{-1}\left(\frac{r_3(r_3+m)+r_2(r_3-m)}{(r_3+m)(r_2+r_3)}\right) && \text{(B.8)}\\
F_{lt} &= -F_{21}\cos\alpha - F_{23}\sin(\theta+\beta) && \text{(B.9)}\\
F_{21}r_2\cos\alpha &= F_{23}(r_2+r_3)\sin\beta && \text{(B.10)}\\
|\tau_{in}| &= F_{21}r_1\cos\alpha && \text{(B.11)}\\
F_{lt} &= -|\tau_{in}|\left(\frac{1}{r_1}+\frac{r_2\sin(\theta+\beta)}{r_1(r_2+r_3)\sin\beta}\right) && \text{(B.12)}
\end{aligned}
$$

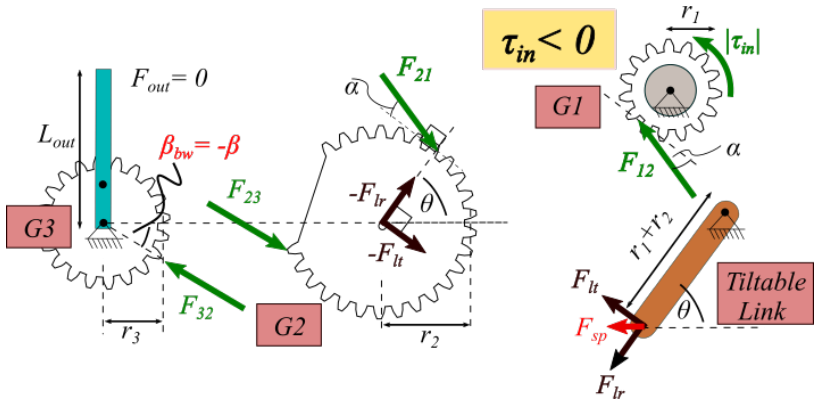

Figure B-2: Free body diagram of gear jamming (backward drive)

with the assumption of $F_{sp} << |F_{lt}|$, similar to previous analysis in Eq. 4.13 and Eq.4.14, the condition for jam-free engagement in backward drive is

$$r_2 \sin(\theta + \beta) > -(r_2 + r_3) \sin \beta \tag{B.13}$$

Using a graphical representation in Fig.B-3, the backward jam-free range of θ can be calculated as follows,

$$\theta_1 = \frac{-\pi}{2} + \cos^{-1}\left(\frac{(r_2 + r_3) \sin \beta}{r_2}\right) \tag{B.14}$$

$$\theta_2 = \frac{3\pi}{2} - \cos^{-1}\left(\frac{(r_2 + r_3) \sin \beta}{r_2}\right) \tag{B.15}$$

$$\theta_1 - \beta < \theta < \theta_2 - \beta \tag{B.16}$$

Now let's compare between the jam-free range in forward drive and backward drive. Fig. B-4 shows the graphical representation of both condition. For clarity, A is defined as the arccosine term in the conditions.

$$A = \cos^{-1}\left(\frac{(r_2 + r_3) \sin \beta}{r_2}\right) \tag{B.17}$$

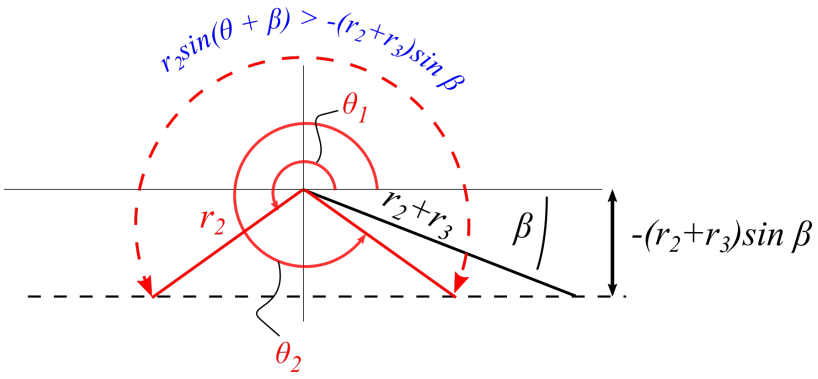

Figure B-3: Graphical representation of Eq.B.13

Therefore the jam-free conditions can be rewritten as

Forward jam-free:

$$\frac{\pi}{2} - A + \beta < \theta < \frac{\pi}{2} + A + \beta \tag{B.18}$$

Backward jam-free:

$$\frac{-\pi}{2} + A - \beta < \theta < \frac{3\pi}{2} - A - \beta \tag{B.19}$$

Seemingly, the jam-free range in the forward drive is a subset of the range in the backward drive. This means that any link angle θ, chosen from the jam-free condition in the forward drive, can achieve the jam-free engagement in backward drive as well. The only way that this is not true is when the forward jam-free range has any part outside the backward range. For |A| and |β| in the first quadrant, this can only happen when

$$A + \beta > \frac{\pi}{2} \tag{B.20}$$

$$\cos^{-1}\left(\frac{(r_2 + r_3)\sin\beta}{r_2}\right) > \frac{\pi}{2} - \beta \tag{B.21}$$

$$\frac{(r_2 + r_3)\sin\beta}{r_2} < \cos\left(\frac{\pi}{2} - \beta\right) \tag{B.22}$$

$$\frac{(r_2 + r_3)}{r_2} < 1 \tag{B.23}$$

where Eq.B.23 is impossible as the gear radii are positive. Therefore it can be concluded

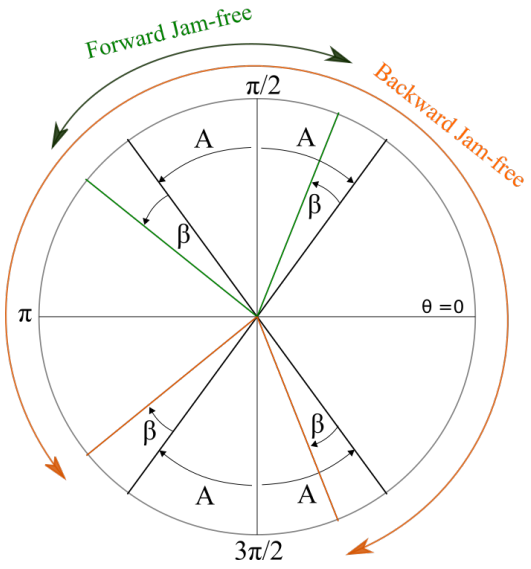

Figure B-4: Graphical comparison between jam-free ranges of θ in forward and backward drive

that the backward jam-free engagement is possible for all the θ that satisfy the forward jam-free condition in Eq:4.17.

From the analysis, the link angle chosen from forward drive condition will always produce a jam-free engagement but unstable meshing in backward drive. To put it simply, G2 will engage G3 without jamming but will move away from G3 due to the reaction forces in meshing. After the gear teeth are out of contact, G2 then swings back into the engagement by the preload spring at the tiltable link, causing a ratchet-like cycle during backward drive. This ratchet-like motion causes the gear-clutch mechanism to behave similar to a one-way clutch. One application is to prevent excessive torque in backward direction such as at the physical limit of the output link. Fig. B-5 shows the scenario which the output link is driven backward until it reaches a physical limit, producing F_{out} in opposite direction. The upper part of the figure illustrates its ratchet-like movement equivalent to that of the lower part of the figure. This one-way characteristic of the gear-clutch occurs when the bottom surface of G3 gear tooth is in contact with the top surface of the G2 gear tooth, causing the force F_{23} to point downward as shown in Fig. B-2. Another scenario of ratcheting would be when G3 is driven in the forward direction with a higher speed than G2. An example case is that when the load suddenly drop or disappear after the gear-clutch engagement. Fig.

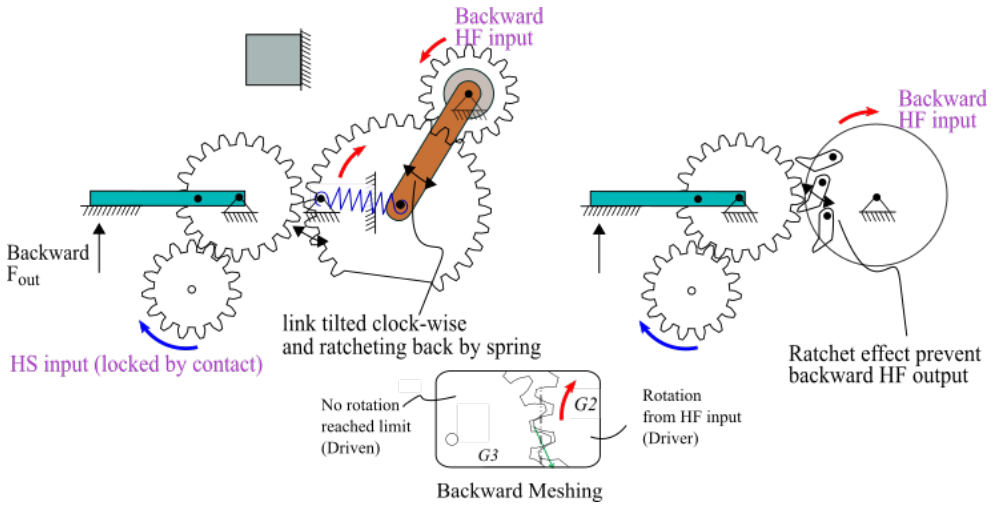

Figure B-5: Ratcheting in backward drive

B-6 illustrates the case. G3 now becomes the driver that push G2 downward. This allows the output rotation speed at G3 to not be limited by the slower G2 supplied by HF input. Obviously, once the output link contacts the object, or the low output torque from HS input become sufficient for the load, G3 will now switch from being a driver to a driven gear. No ratcheting would occur and the gear-clutch will enter a stable meshing state, producing the HF phase of the LRT. This characteristic is similar to a one-way clutch which the output is allowed to rotate at a higher speed than the output. It has to be noted that the analysis was

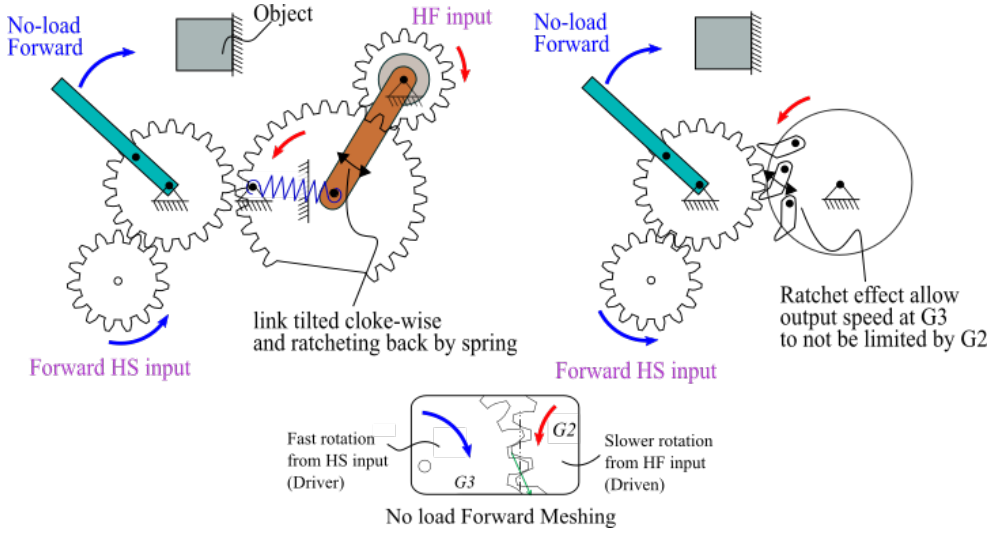

Figure B-6: Ratcheting in low-load forward drive

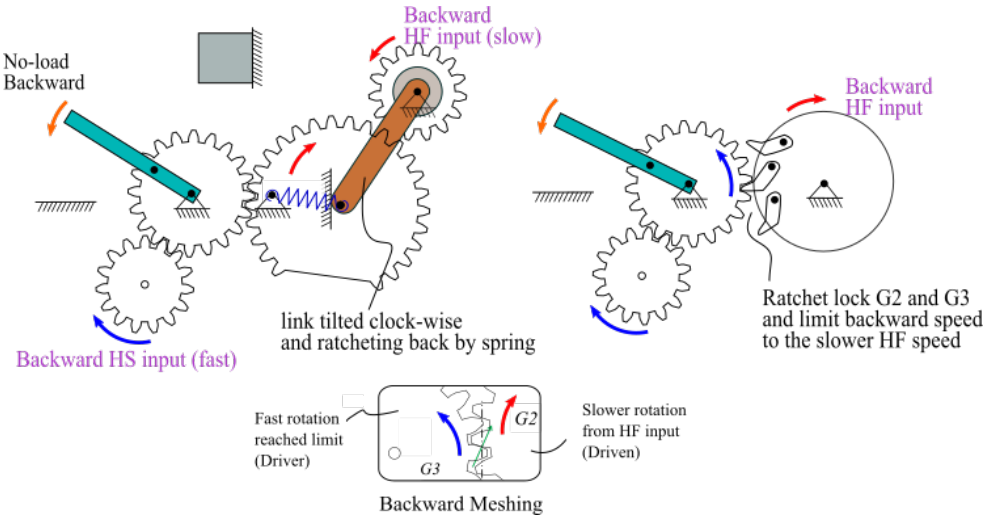

Figure B-7: Speed limitation in low-load backward drive from HS

done in a quasi-static manner, which means an existence of F_{out} was assumed to counter the backward drive torque. In the case of the backward drive without such external force F_{out}, e.g., a no-load backward motion, the backward tangential speed of G2 teeth supplied by the HF input will be slower than that of G3, which is driven by the HS input. In this case, G3 will be the driver that push G2 teeth upward. Fig. B-7 shows the backward drive in a low or no-load situation. The free body diagram of the gears now becomes similar to the analysis of the gear-clutch with the forward drive. However, the input torque now comes from G3 instead of G1. Therefore, the backward drive from HS will produce a stable meshing for all link angle θ chosen from the stable meshing condition in the forward direction. That is no ratcheting occurs in the low-load backward drive. The backward speed of the gear-clutch is then limited by the speed of the slower HF input until G2 completely disengages from G3.